

625939
3181549
TR diss 2562

**TR diss
2562**

**ON THE CONTROL OF POWDER COMPACT
MICROSTRUCTURE THROUGH
METHODS OF WET CONSOLIDATION**

Stellingen

behorende bij het proefschrift

On the control of powder compact microstructure through methods of wet consolidation

van Peter van Houten

- 1 Bij natte verdichting moet de stroming van de vloeistof waaraan de deeltjes tijdens consolidatie onderhevig zijn worden gestuurd, als uitgangspunt voor de beheersing van de kwaliteit van een gesinterd product.
- 2 Variatie van het tijd-temperatuur pad van het sinterproces geeft de mogelijkheid om de relatie te versterken tussen verschillen in microstructuur van groene deeltjespakkingen en verschillen in microstructuur van de resulterende gesinterde vormstukken.
- 3 Het verband tussen reologie en ideale consolidatie, in termen van het meesleeffect, maakt het mogelijk om de dichtheid van natte deeltjespakkingen en de invloed van de suspensie-stabiliteit op de pakkingsdichtheid te voorspellen.
- 4 In de beschrijving van het shear thinning gedrag van gevlokte suspensies met het Giant-Floc model, had in de definitie van de frictiefactor besloten moeten liggen dat deze onafhankelijk is van de suspensiestabiliteit.
A.J.G. van Diemen en H.N. Stein , Rheol. Acta 22 (1983) 41-50
- 5 Ondanks de schijnbare gelijkenis tussen permeatie en sedimentatie bij geschikte keuze van de gebruikte coördinatenstelsels mogen zij niet worden beschouwd als identieke processen.
- 6 Door, in plaats van uit te gaan van het gemeten filtratiedebiet, de cakehoogte met een onafhankelijke methode te meten, hadden Bridger et al. de foutieve weergave van het verloop van de cake-dichtheid (uitgaande van gemeten filtratiedebiet) kunnen vermijden.
K. Bridger , M. Tadros , W. Lieu en F. Tiller , Separation Sci. and Techn. 18 (12&13) (1983) 1417-1438
- 7 Het verdient de voorkeur om in publicaties betreffende reologie en consolidatie, de hoeveelheid vastestof in suspensies te vermelden op volumebasis in plaats van op gewichtsbasis.
H. Nienburg , P. Stein , F. Harbach , cfi/Ber. Deutsche Keramische Gesellschaft 66 [5/6] (1989) 189-197
- 8 Het technische niveau van een cultuur wordt veelal ten onrechte gelijk gesteld aan de mate van beschaving, het is echter slechts een aspect hiervan.
- 9 Daar de beschrijvingen van veel gebeurtenissen sterk persoons- en cultuur-afhankelijk zijn, is "het leren van de geschiedenis" een hachelijke zaak.
- 10 In een multiculturele samenleving leidt armoede tot een toestand waarin de verschillen in geloof en cultuur tussen verschillende groeperingen zodanig worden benadrukt, dat enkele opruiende politieke uitspraken tot een etnisch conflict kunnen leiden. In tegenstelling tot een economische boycot, kan het intensiveren van de handelsbetrekkingen, gepaard met politieke druk, leiden tot het voorkomen of beeindigen van zulke conflicten.

**ON THE CONTROL OF POWDER COMPACT
MICROSTRUCTURE THROUGH
METHODS OF WET CONSOLIDATION**

PROEFSCHRIFT

ter verkrijging van de graad van doctor
aan de Technische Universiteit Delft,
op gezag van de Rector Magnificus prof. ir. K.F. Wakker,
in het openbaar te verdedigen ten overstaan van een commissie,
door het College van Dekanen aangewezen,
op maandag 22 mei 1995 te 16.00 uur
door

Jan Peter VAN HOUTEN

materiaalkundig ingenieur
geboren te 's-Gravenhage



Dit proefschrift is goedgekeurd door de promotor Prof.dr. G. Frens.

Samenstelling promotiecommissie :

voorzitter	: de Rector Magnificus	
promotor	: Prof.dr. G. Frens	TU-Delft, fac der Scheikundige Technologie en der Materiaalkunde
leden	: Prof.dr. H.N. Stein	TU-Eindhoven, fac Scheikundige Technologie
	Prof.dr. A.P. Philipse	U-Utrecht, fac Scheikunde
	Prof. B. Scarlett MSc.	TU-Delft, fac der Scheikundige Technologie en der Materiaalkunde
	Prof.dr. G. de With	TU-Eindhoven, fac Scheikundige Technologie /Philips Nat.Lab.
	Prof.dr. ir. H.E.A. van den Akker	TU Delft, fac der Technische Natuurkunde
gast	: Dr.ir. B.C. Bonekamp	ECN Petten

The work for this thesis has been performed at the Netherlands Energy Research Foundation (ECN), Petten, The Netherlands.

CIP-DATA KONINKLIJKE BIBLIOTHEEK , THE HAGUE

Houten, Jan Peter van

On the control of powder compact microstructure through methods of wet consolidation / Jan Peter van Houten.

PhD Thesis Delft University of Technology. - With lit. - With summary in Dutch.

ISBN 90-9008237-9

NUGI 841

Subject headings : ceramic processing / wet powder consolidation

Copyright ©1995 by J.P. van Houten

All rights reserved. No part of this publication may be reproduced or utilized in any form or by any means, electronic or mechanical, including photocopying, recording or by any information storage and retrieval system, without the written permission of the author.

Printed and bound in The Netherlands by:

Reprografische Dienst ECN Petten

No matter what kind of plank bridge they threw across, it was always swept away by the waters; for either the Žepa would rise quickly and unexpectedly, as mountain streams are wont to do, and weaken the bridge and sweep away the logs, or else it was the Drina that swelled suddenly and rushed into the channel of the Žepa and backed its flow, so that its level rose and bore the bridge away as if it had never been.

from : *The bridge on the Žepa*, Ivo Andrić (1924)

CONTENTS

Chapter 1 Introduction

1.1 Background	9
1.2 The scope of this thesis	15

Chapter 2 Some aspects of colloidal densification processes for technical ceramics

2.1 Colloidal densification	17
The influence of relative direction of liquid flow on particle stacking	17
2.2 Modelling filtration processes	20
The classical filtration theory	20
Filtration with a constant rate	23
Filtration with a constant pressure; Slipcasting	23
The consolidation zone during filtration	25
2.3 Modelling centrifugal densification	30
Compact growth rate	30
The consolidation zone during centrifugation	31

Chapter 3 Rheology of concentrated α -alumina suspensions

3.1 Introduction to rheology	33
3.2 Modelling the rheology of concentrated suspensions	34
The Dougherty-Krieger relation	35
The Giant-Floc model	37

Chapter 4 Rheological investigation of concentrated α -alumina suspensions

4.1 Suspension preparation and characterization	45
Colloid stability of dilute A16SG-F/H ₂ O/Al(NO ₃) ₃ suspensions	51
Colloid stability of more concentrated A16SG-F suspensions	52
4.2 Rheology of concentrated α -alumina suspensions	56
Measurement procedures	56
Preparation of suspensions	60
Determination of $\eta_{r,\infty}$	61
Interpretation of the viscosity data according to the Giant-Floc model	66

Chapter 5 Compaction of concentrated α -alumina suspensions, drying and sintering

5.1	Introduction	71
5.2	Experimental	72
	Wet compaction	72
	Drying of the wet particle compacts	78
	Pre-sintering and porosity measurement	81
	Sintering of particle compacts	82
	SEM investigation of microstructure development	84
5.3	Results of compaction and characterization	87
	Properties of the wet compacts	87
	Properties of the dried and pre-sintered compacts	92
	Microstructure development during sintering	95

Chapter 6 Thesis 103

Appendices

The permeability of a particle compact	105
Derivation of the geometrical constants of a concentric cylinder system	107
Error sources with a concentric cylinder measurement geometry	112
Measured flow curves in linear-linear representation	117
Calculation of volumetric shrinkage	120
Microstructures of sintered compacts	121

Summary 129

Samenvatting 133

Nawoord 137

Curriculum Vitae 139

Chapter 1

Introduction

1.1 Background

Compared with more conventional materials like metals, plastics and wood, technical ceramics is a group of inorganic engineering materials with special properties. Some of these properties, in particular hardness, wear-resistance and strength at elevated temperatures, are essential in the rapidly growing field of high temperature energy conversion.

In this thesis we will be concerned with the ceramic α -alumina (also known as α - Al_2O_3 , corundum), a hard and wear-resistant material even at elevated temperatures. It has a high chemical resistance and excellent dimensional stability. Some typical data on polycrystalline α -alumina are shown in Table 1.1 . Thermal properties at elevated temperatures are listed in Table 1.2 .

Table 1.1 Properties of polycrystalline α -alumina [1-6]

crystalline structure :	rhombohedral
density, ρ :	3.98 g/cm ³
hardness (Vickers) :	20 GPa
yield stress, σ :	600 MPa
stress intensity factor, K_{Ic} :	4.9 MPa $\sqrt{\text{m}}$
Youngs modulus, E :	403 GPa
shear modulus, E_{shear} :	163 GPa
bulk modulus, E_{bulk} :	255 GPa
Poisson ratio, ν :	0.236 [-]
surface energy, γ_0 (21 °C) :	1.2 J/m ²
melting point, T_m :	2047 °C
thermal shock resistance * :	$\Delta T \sim 170$ °C

* quenching in water at room temperature,
assuming a geometrical factor of 1

The exact values of these properties are subject to variations related to the purity and the microstructure of the alumina. **Thus the quality of an alumina product depends on the ceramic processing technology from the powder onwards.**

From tables 1.1 and 1.2 we might anticipate extensive use of α -alumina ceramics in advanced heat engines and in other industrial applications. Examples are chemically and high temperature resistant linings, fan blades, valves, nozzles and bearings, as well as cutting tools, knife blades and crucibles. But in spite of the favourable material properties of technical ceramics, and in particular of α -alumina, a delay in the expected growth of applications of technical ceramics has occurred.

Table 1.2 Thermal properties of polycrystalline alumina at various temperatures [7-10]

	Temperature :			
	21 °C	400 °C	800 °C	1200 °C
heat capacity, C_p [J/mol K] :	15.5	21.7	23.7	24.8
linear thermal expansion, α [10^{-6} K $^{-1}$] :	5.43	7.33	8.97	9.73
thermal conductivity, K [J/m s K] :	36.0	12.8	7.0	5.5

In engineering, the selection of a material is based on the desired material quality (performance) in combination with the costs of production. A property P of an engineering material is related to the value of the intrinsic material property P_i . When focusing at the strength of ceramic products, P_i is given by the theoretical strength. Material processing then influences factors like purity and microstructure of the final product which may deteriorate the strength. A property of an engineering material can thus be expressed as $P = t \cdot P_i$, with P_i the intrinsic material property and t a technology factor, bound in the interval [0-1]. Increasing this factor, by optimizing and controlling material processing, increases the costs of production. In time, t is bound by the state of the art of processing the material.

Compared with conventional materials, promising new engineering materials are accompanied by higher P_i values. The processing of new materials, however, is less developed (lower values of t at high costs of production). To compete with conventional materials, which can meet the required P , the processing of new engineering materials has to be improved.

An important property restricting the use of ceramics is the **brittleness** of ceramic materials. Without ductility most traditional shaping methods, like bending, rolling and forging, are inapplicable. This implies that shaping of ceramics should be an integral part

of the material processing (in general ceramics are shaped during powder consolidation). When after sintering (resulting in shrinkage) a near net shape is obtained, the finishing of a product by machining can be minimized (lowering the costs of production). Furthermore brittleness gives rise to abrupt failure under tensile stress [11,12], which is unpredictable as a consequence of the wide range of possible structural defects (flaws) causing failure. The sensitivity of the magnitude of the failure stress towards flaw size is shown by the Griffith-Irwin failure criterion [13]

$$\sigma\sqrt{\pi a} \geq \sigma_c\sqrt{\pi a} = K_c \quad [Pa \sqrt{m}] \quad (1.1)$$

with σ [Pa] the applied stress, σ_c [Pa] the failure stress, K_c [Pa \sqrt{m}] a material property called the critical stress intensity factor characterising the resistance towards cracking, and a [m] the dimension of the largest present flaw.

To avoid brittle fracture structural flaws have to be eliminated during the processing stage and/or the shape of traditional functional parts has to be redesigned, avoiding tensile stress concentrations during operating conditions.

In case of ceramics, a strong interaction between desired material properties, material processing operations and the design of a functional part is necessary, which complicates engineering.

Flaws are introduced in all stages of processing :

- Powder manufacturing procedures may result in impurities and inclusions (mining, flotation and milling) and hard agglomerates (roasting procedure). A hard agglomerate consists of a loose group of particles sintered together at their contact points, characterised by a large internal porosity.
- Powder compacts may contain stacking defects due to soft agglomerates (caused by van der Waals attraction) or due to the used consolidation procedure.
- Drying a wet particle compact or burning out organic binders from a dry particle compact can respectively result in cracking and the formation of coarse pores.

Local density variations in the compact may be considered as flaw precursors. These result in shape and size distributions of residual pores in the finally sintered product. Furthermore, sintering at too high a temperature or traces of chemical impurities can result in abnormal grain growth (ultimately grain boundaries may be considered as flaws). Machining of the sintered products creates surface cracks.

In general there are two methods of improving the reliability of ceramics. One method is to change the failure mechanism. This can be done by adding a second phase material, resulting in deflection of cracks or absorption of energy on crack propagation, in such a way that the flaw population due to the processing may be tolerated. Examples of toughening mechanisms are fibre pull out, phase transition toughening and Wake toughening [11].

The other method is control of the flaw size distribution due to material processing, by improving the process reliability. The ultimate goal then is a flawless microstructure with a small mean grain size and a narrow grain size distribution (GSD).

Here we will focus our attention on controlling the processing of alumina.

In our opinion, to minimize the flaw distribution, all processing steps should be considered, starting with choosing a suitable ceramic powder in combination with an appropriate forming method.

With ceramics, the number of applicable forming methods are rather limited [14]. In practice most ceramic products are formed by densification of a powder resulting in a powder compact. After sintering of this compact a near net shaped product will be obtained, and machining of this shape will result in the final product.

Two principal methods of powder consolidation can be distinguished, a dry consolidation route and a wet consolidation route or colloidal route.

In the dry route, techniques as uniaxial [15] and isostatic pressing are used. A flowable powder is required for controlled filling of the die. Flowable powders are powders with rather large particles ($> 10 \mu\text{m}$), because the mass forces on the particles have to exceed their van der Waals attraction. Sintering of a compact with coarse particles results in a coarse grained microstructure. Flaws originally present in the powder, like hard and soft agglomerates, will be recognizable in the compact and also in the product. The dry route is especially appropriate for mass production of small ceramic products of a simple shape.

In the wet or colloidal route, a (submicrometer) powder is dispersed in water [16,17]. In a colloidal dispersion the particle-particle interactions can be controlled. Attractive van der Waals forces may be counterbalanced by electrostatic repulsion and/or steric hindrance. In this way soft agglomerates may be broken up, whereas hard agglomerates and foreign inclusions can be removed by settling, based on differences in buoyancy.

Compared with the dry processing route the wet route offers more tools for improving processing reliability and powder consolidation.

Wet consolidation techniques are injection moulding, tape casting, electrophoretic deposition, slip casting, pressure filtration and centrifugal densification [14]. For the ultimate strength of the product, injection moulding is not favourable : the concentrated dispersions contain large amounts of plasticizers, and these have to be burnt out before sintering. Electrophoretic deposition and tape casting resp. produce thin layers ($1\text{-}50 \mu\text{m}$) and tapes ($50\text{-}1000 \mu\text{m}$).

For mechanical strength in combination with a complicated shape of a ceramic part, consolidation techniques like **pressure filtration, slip casting and centrifugal densification** are preferred. These are best used to produce products in small series. Figure 1.1 is a flowsheet of the colloidal approach for producing a ceramic part. It clearly identifies where possibilities are present for reducing the flaw size distribution and obtain better ceramics.

With an optimized powder, the microstructure of a wet compact is determined by the combination of suspension properties and process parameters.

For maximum strength, suspension and process parameters should be chosen to obtain a dense and homogeneous (at a size scale of 10 particles or more) wet particle compact in order to bring about a homogeneous sintering process throughout the product. The wet compact, acting as a precursor in the formation of the microstructure in the "green" (dried) compact, finally affects the development of sintered microstructure in the ceramic [18-20]. In this thesis we will focus on controlling the microstructure of wet compacts and on the influence of the wet compact structure on drying and sintering.

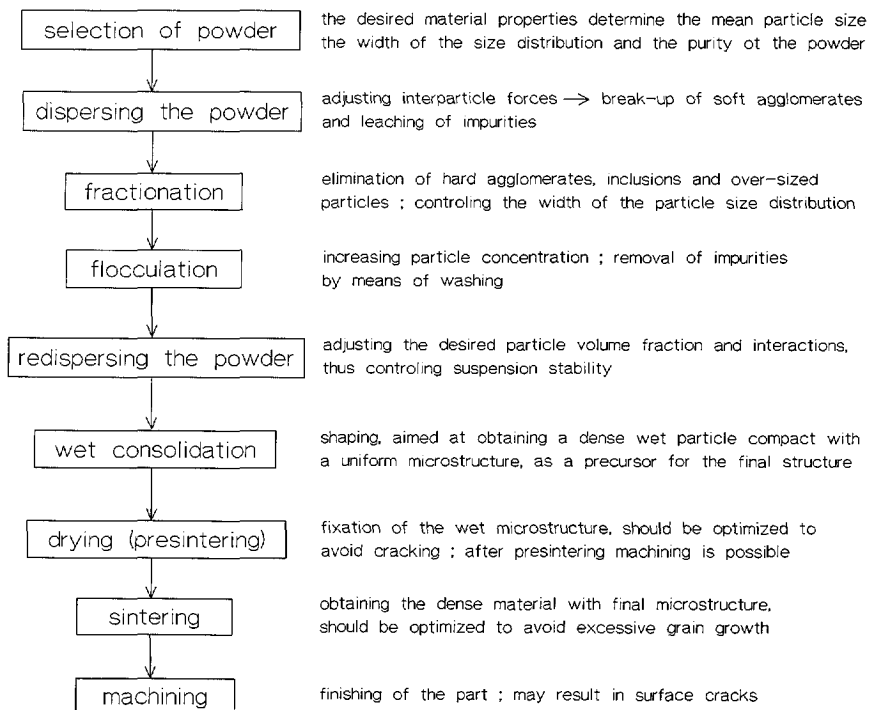


Figure 1.1 Flowsheet of ceramic processing, the colloidal route

References

- [1] E. Dörre , H. Hübner, "Alumina, processing, properties, and applications" , Springer-Verlag , Berlin (1984)
- [2] C.T. Lynch (ed) , "Handbook of material science Vol I" , CRC Press (1975) 357-363
- [3] R.C. Weast , M.J. Astle (eds) , "Handbook of chemistry and physics, 60th ed." , CRC Press Inc. , Boca Raton , Florida , US (1980), page b52
- [4] F.F. Lange , J. Mater. Sci. 17 (1982) 247
- [5] D.H. Chung , G. Simmons , J. Appl. Phys. 39 (1968) 5316-5326
- [6] J.J. Rasmussen , R.P. Nelson , J. Am. Ceram. Soc. 55 (1972) 326-327
- [7] W.D. Kingery , H.K. Bowen , R.D. Uhlmann , "Introduction to ceramics 2nd ed." , Wiley and sons , New York (1976)
- [8] R.L. Coble , W.D. Kingery , J. Am. Ceram. Soc. 39 (1956) 377-385
- [9] W.H. Gitzen , "Alumina as a ceramic material" , The Am. Ceram Soc. Inc. , Columbus Ohio (1970)
- [10] T.H. Nielsen , M.H. Leipold , J. Am. Ceram. Soc. 46 (1963) 381-387
- [11] L.A. Correia , ECN Memo N° 89-149 (1989)
- [12] H. Nienburg , P. Stein , F. Harbach , cfi/Ber. Deutsche Keramische Gesellschaft 66 [5/6] (1989) 189-197
- [13] H.L. Ewalds , R.J.H. Wanhill , "Fracture Mechanics" , DUM Delft (1984)
- [14] F.F. Lange , J. Am. Ceram. Soc. 72 [1] (1989) 3-15
- [15] R.A. Thompson , Ceram. Bull. Vol 60 [2] (1981) 237-251
- [16] A. Aksay , C.H. Schilling , "Colloidal filtration route to uniform microstructures" in "Ultrastructure processing of ceramics" , eds. L.L. Hench , D.R. Ulrich , Wiley and sons , New York (1984) 439-446
- [17] J. Ceserano III , I. A. Aksay , J. Am. Ceram. Soc. 71 [4] (1988) 250-255
- [18] B.C. Bonekamp , H.J. Veringa , Klei/Glas/Keramiek [8] (1986) 166-169
- [19] T. Kimura , Y. Matsuda , M. Oda , T. Yamaguchi , Ceram. Int. 13 (1987) 27-34
- [20] A. Roosen , H. K. Bowen , J. Am. Ceram. Soc. 71 [11] (1988) 970-977

1.2 The scope of this thesis

In ceramic technology the importance of the microstructure of a wet particle compact on the resulting quality of the finally fired product has generally been recognized [1-6]. However, no integral investigation has been made to relate suspension properties and parameters of various densification techniques to the resulting wet compact, the dried compact, the sintering behaviour and the microstructure development during sintering. The aim of this thesis is to establish such an integral investigation based on a chosen α -alumina submicrometer powder, Alcoa's A16SG.

Wet compact formation is governed by both process and suspension parameters. A wet particle compact will be formed in a consolidation zone. In this zone, any displacement of a particle is restricted by the interaction of a particle with surrounding particles, because, upon displacement, a particle has to drag its neighbouring particles along. This drag effect depends on the coordination number of the particles q and the strength of their interaction, both determined by suspension parameters. Particle drag in this consolidation zone is a restriction on the further densification of the compact.

Particle displacement is due to friction because of the fluid movement relative to the particles in the consolidation zone. Depending on the direction and magnitude of the friction force, which is a process parameter, further densification of the consolidation zone may be possible or not.

The following propositions will be investigated :

- 1 - Rheological investigation may reveal which drag parameters govern further densification of the consolidation zone, i.e. the particle interaction force and coordination number. Thus a link between rheology and consolidation may be established.**

In Chapter 3 a rheological model will be developed incorporating both drag parameters, by adapting the Giant-Floc model [7] which describes the viscosity of concentrated flocculated suspensions.

- 2 - There is a relation between rheological parameters of a suspension and the density of wet compacts formed by pressure filtration.**

The strength of particle interactions, incorporated in an interaction parameter I^2 [-], restricts the possible movements of the particles in the consolidation zone. The influence of this interaction parameter I^2 [-] on the density of wet compacts as formed with pressure filtration, will be investigated in Chapter 4.

- 3 - **Process parameters of the densification technique can be identified, which affect the final density of the wet compact through the influence of fluid movement relative to the particles in the consolidation zone.**

An experimental investigation concerning the influence of the parameters in the consolidation zone on the relative density ϕ_v [-] of a wet compact will be the subject of Chapter 5. Pressure filtration, slip casting and centrifugal densification, using a colloidal stable suspension, will be compared.

- 4 - **The wet, the dried and the final sintered structures are related.**

In Chapter 5 the relation between the properties of wet compacts, dried compacts and sintered compacts will be investigated, using standard drying and sintering procedures. The results will indicate how the wet structure, determined by particle interactions and consolidation parameters, affects both the drying and sintering behaviour, and in particular the development of the microstructure during sintering.

From the first three propositions the density of any wet particle compact can be predicted, based on knowledge of the parameters of the suspension and of the densification process. The last proposition relates the obtained wet structure, the dry structure and the microstructural development during sintering.

The integral investigation in this thesis leads then to a picture of how the quality of ceramic products can be controlled through the skilful application of the principles of suspension technology during the (wet) consolidation and drying of the product.

References

- [1] F.F. Lange , J. Am. Ceram. Soc. 72 [1] (1989) 3-15
- [2] I.A. Aksay , "Microstructure Control Through Colloidal Consolidation" in "Adv. in Ceramics N° 9" , eds. J.A. Mangels , G.L. Messing , The Am. Ceram. Soc. Inc. , Columbus Ohio (1984) 94-104
- [3] C.H. Schilling , "Microstructural Development by Colloidal Filtration" , thesis Univ. of California Los Angeles (1983)
- [4] A.P. Philipse , B.C. Bonekamp , H.J. Veringa , J. Am. Ceram. Soc. 73 [9] (1990) 2720-2727
- [5] A. Roosen , H.K. Bowen , J. Am. Ceram. Soc. 71 [11] (1988) 970-977
- [6] H. Nienburg , P. Stein , F. Harbach , cfi/Ber. Deutsche Keramische Gesellschaft 66 [5/6] (1989) 3-15
- [7] A.J.G. van Diemen , H. Stein , Rheol. Acta 22 (1983) 41-50

Chapter 2

Some aspects of colloidal densification processes

2.1 Colloidal consolidation

Since the wet structure of a particle compact affects the microstructure of the dense product, we will take a closer look at mechanisms of wet compaction. We shall compare pressure filtration, at constant rate or constant pressure (slip-casting), with centrifugal densification, because in these two consolidation methods the liquid flow relative to the motion of the particles is in opposite direction. This liquid flow could be a factor influencing the density of a compact through hydrodynamic forces between the particles in the consolidation zone. Real particle packings will deviate from ideality, viz. a hexagonal close packing, because of

- non-spherical particles
- non-uniform particle size
- soft and hard powder agglomerates
- non ideal stacking because of interaction between the particles during consolidation

For a given powder an important consolidation parameter is the Péclet (Pé) number. Pé describes the ratio of the particle velocity in the consolidation process, v_{process} [m/s], and the rate of self-diffusion of a particle over a distance of it's own radius, $v_{\text{diffusion}}$ [m/s] :

$$Pé = \frac{v_{\text{process}}}{v_{\text{diffusion}}} = \frac{v_{\text{process}}}{D/R} = \frac{v_{\text{process}}}{kT/(6\pi\eta_0 R^2)} \quad [-] \quad (2.1)$$

with Boltzmann's constant k [J/K]. The particle radius R [m], temperature T [K], viscosity of the suspending medium η_0 [Pa s] and diffusion coefficient D [m²/s] are parameters which are chosen in the preparation of the suspension, while v_{process} relates to the size and operation of the processing equipment.

The influence of the relative direction of liquid flow on particle stacking

In pressure filtration, the velocities of the fluid and the particles in the suspension are the same (fig. 2.1). In the suspension no ordering of the particles will occur in absence of a relative fluid velocity. When a particle arrives at the compact it will be detained, whereas the surrounding fluid flows on.

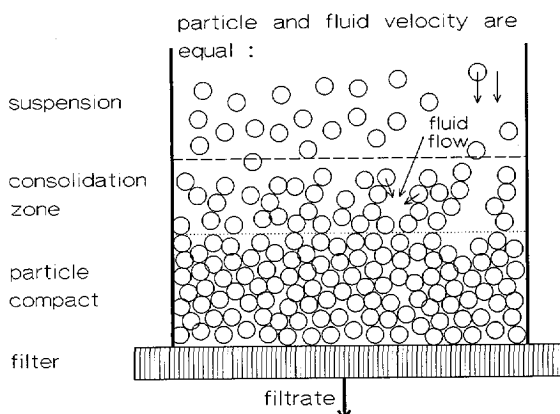


Figure 2.1 Relative particle movement in case of filtration

This would result in the formation of a randomly stacked consolidation zone with low density, but a particle in the consolidation zone experiences friction forces from the passing fluid. On the average the friction is directed towards the filter, and drags the particles into a denser packing. When a particle moves because of this friction force it will have to move surrounding particles. The energy involved in moving neighbouring particles depends on the number of nearest neighbours (q) of the particles and the interaction between the touching particles (interaction parameter l^2). This effect opposes the densification.

The consolidation zone is the part of the flowing suspension in which this interaction between the particles through flow and suspension properties determines the eventual stacking of the particles in the compact.

With a negligible drag between particles (low number of nearest neighbours, comparatively small attractive interparticle forces), friction forces exerted by the fluid result in a continuous transition of the random and open transition zone to a more dense random particle packing.

Strong interaction between the particles, on the other hand, will oppose the densification in the consolidation zone.

In case of centrifugation (figure 2.2), the particles in the suspension move relative to the fluid. In the consolidation zone they experience a friction force which opposes compaction, because of the (counter)flow of the medium. This counterflow promotes ordering of the particles, which results in an ordered, non-randomly stacked, consolidation zone. A particle inside the consolidation zone will experience a hydrodynamic force which hinders further densification as long as the particle compact is densifying, i.e. while fluid

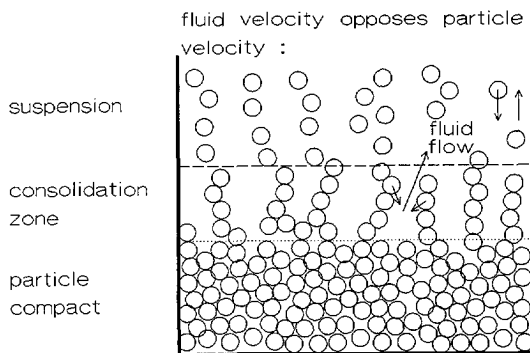


Figure 2.2 Relative particle movement during centrifugal densification

displacement occurs.

Thus, in case of pressure filtration the absence of a friction force on particles in the suspension results in the formation of a randomly stacked consolidation zone, and the friction force experienced by the particles in the consolidation zone promotes further densification. In this respect filtration, in contrast to centrifugation, could be an ideal densification process. Some authors have indeed found a lower compact density and an increased mean pore size resulting from centrifugation, than from pressure filtration of the same suspension [1,2].

References

- [1] A.P. Philipse , B.C. Bonekamp , H.J. Veringa , J. Am. Ceram. Soc. 73 [9] (1990) 2720-2727
- [2] A. Roosen , H. K. Bowen , J. Am. Ceram. Soc. 71 [11] (1988) 970-977

2.2 Modelling filtration processes

Filtration is an important unit operation in chemical engineering [1-29], but the theory behind it is also extended to soil mechanics, to gain insight in the behaviour of flowed-through porous soils [30-32]. When we compare these two disciplines there seems to be a remarkable difference in the modelling of filtration.

In chemical engineering filtration is a separation technique. The emphasis is on the relation between the external, measurable, time-dependent filtration parameters pressure and filtration rate. Although the importance of suspension properties is recognised, interactions between the suspended particles are omitted from the modelling of the filtration process.

Properties of a wet filter cake, such as a time dependent distribution of porosity and the permeability distribution, can then be derived from the external parameters [5-8,21].

In the modelling of filtration for soil mechanics, the particle interactions are considered essential. This complicates the experimental part of filtration research, for in addition to the external filtration parameters internal parameters like the pressure and porosity of the compact have to be measured as a function of time and position.

Permeabilities of alumina compacts in ceramic processing vary between 10^{-18} and 10^{-17} m². These low permeabilities correspond to high filtration pressures (> 50 bar), even for compact layers in the millimetre thickness range. Because in such thin layers the spatial distribution of the internal filtration parameters cannot be measured accurately, we will first describe filtration in terms of the chemical engineer.

The classical filtration theory

Classical filtration theory is based on the following assumptions [17,33] :

- The pressure drop over a flowed-through porous medium can be described with Darcy's law
- The interfaces between the filter, particle compact and suspension are assumed to be discontinuous
- Particle interaction, diffusion and sedimentation are neglected; suspension characteristics are assumed time independent
- The particle compacts are incompressible, i.e. porosity and permeability of the compact are independent of spatial coordinates, which results in a linear pressure distribution over the compact.
- The flow resistances of flowed-through porous layers are additive

A general filtration equation can be derived by combining the flow equation (Darcy's law) with a mass balance and an external pressure balance. The chosen coordinate system

is shown in figure 2.3 .

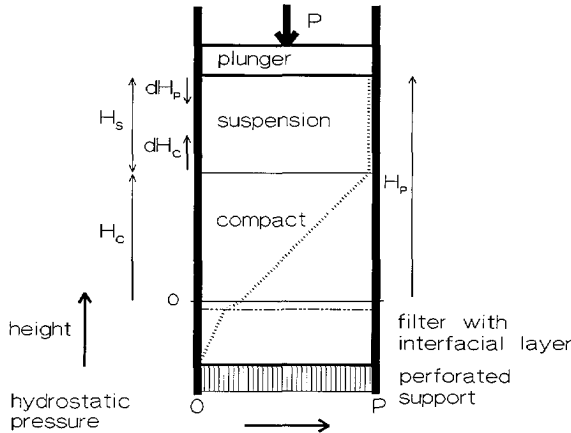


Figure 2.3 The coordinate system used in deriving the filtration equation

A descent of the plunger results in the displacement of a corresponding amount of the suspension. As a consequence of fluid incompressibility the same amount of filtrate has to pass through the filter plate. A particle volume balance results (after integration, assuming constant compact porosity) in a relation between the height of the particle compact H_c [m] and the plunger descent ΔH_p [m] :

$$H_c = \frac{\Delta H_p(t)}{C} = \frac{\Delta(H_s + H_c)}{C} = \frac{H_{p(t=0)} - H_p(t)}{C} \quad [m] \quad (2.2)$$

The constant of consolidation C [-] depends on the volume concentration ϕ_v [-] of particles in the suspension and the porosity ϵ_c [-] of the formed particle compact :

$$C = \frac{1 - \epsilon_c - \phi_v}{\phi_v} \quad [-] \quad (2.3)$$

Darcy's law relates the pressure drop ΔP_x [Pa] over a porous structure X with height H_x [m], permeability K_x [m²] and unit area to the superficial velocity v_f [m/s] through X of a Newtonian fluid with viscosity η_0 [Pa s] :

$$\frac{\Delta P_x}{H_x} = \frac{\eta_0 v_f}{K_x} \quad [Pa/m] \quad (2.4)$$

The superficial velocity is defined as

$$v_f = \frac{1}{A} \frac{dV_f}{dt} = \frac{\dot{V}_f}{A} \quad [m/s] \quad (2.5)$$

with filtrate volume V_f [m^3] and filtration area A [m^2].

The pressure ΔP [Pa], exerted by the plunger, follows after addition of the pressure drop over the filter plate and the pressure drop over the particle compact :

$$\Delta P = \Delta P_f + \Delta P_c \quad [Pa] \quad (2.6)$$

Treating the compact as a continuum, a network stress τ_{network} [Pa] is found with its normal in the direction of densification [5]. This network stress equals the pressure drop ΔP_c [Pa] (eq. 2.4) over the compact.

Combining eqs. 2.2 and 2.4-6 results in the general classical filtration equation :

$$\frac{1}{\dot{V}_f} = \frac{\eta_0}{A^2 K_c C \Delta P} V_f + \frac{\eta_0 R_f}{A \Delta P} \quad [s/m^3] \quad (2.7)$$

with the filter plate resistance R_f [m^{-1}] defined as

$$R_f = \frac{H_f}{K_f} \quad [m^{-1}] \quad (2.8)$$

It can be used to describe both filtration with constant pressure or filtration with constant rate.

Deviations from classical behaviour, e.g. from the linear relation between reciprocal filtration rate and the filtration volume in eq. 2.7, are found when the growing particle compact is compressible or because of clogging in the filter plate top layer [3,13]. The mismatch of pores at the interface between the filter plate and particle compact may cause an extra interfacial resistance $R_i(t)$ [m^{-1}]. Clogging will then increase the resistance of this interfacial layer. Adding the pressure drop over the filter plate/compact interface to eq. 2.6, gives a modified general filtration equation :

$$\frac{1}{\dot{V}_f} = \frac{\eta_0}{A^2 K_c C \Delta P} V_f + \frac{\eta_0 R_f}{A \Delta P} + \frac{\eta_0 R_i(t)}{A \Delta P} \quad [s/m^3] \quad (2.9)$$

Filtration with a constant rate

In case of an imposed constant filtration rate v_p [m/s] the relation between plunger velocity, filtration rate and filtrate volume is :

$$v_p = \frac{\dot{V}_f t}{A} = \frac{V_f}{A} \quad [m/s] \quad (2.10)$$

Substitution in eq. 2.9 gives the time dependent pressure drop over the filter cake for constant rate filtration :

$$\Delta P(t) = \frac{\eta_0 v_p^2}{K_c C} t + \eta_0 (R_f + R_i) v_p \quad [Pa] \quad (2.11)$$

This shows a linear relation between filtration time and pressure, because of the linear thickness growth of the compact. During filtration the total pressure drop increases. The pressure drop over the filter remains constant. The partial and also the absolute pressure drop over the particle compact increases during filtration.

Filtration with a constant pressure; Slip casting

With a constant pressure imposed on the filtration system the integration of relation 2.9 with respect to plunger displacement and time yields

$$\Delta H_p = K_c C \left\{ -(R_f + R_i) + \sqrt{(R_f + R_i)^2 + \frac{2 \Delta P}{\eta_0 K_c C} t} \right\} \quad [m] \quad (2.12)$$

showing a parabolic relation between compact thickness and time. The decrease in filtration rate causes a decreasing pressure drop over the filter, but, again the partial and the absolute pressure drop over the particle compact increase. With a small resistance in the filter and the interface, and a compact with a low permeability K_c , the partial pressure drop over the filter becomes negligible and a quadratic relation between compact thickness and time is obtained :

$$\Delta H_p = \sqrt{\frac{2 K_c C \Delta P}{\eta_0} t} \quad [m] \quad (2.13)$$

Slip casting is a special case of filtration with constant pressure. The pressure drop is then not the result of plunger movement but caused by the capillary suction of the pores in the mould. The flow resistance R_m [m^{-1}] of the mould is governed by the depth of penetration H_m [m] of the "filtrate" into the mould. This penetration depth is linearly

coupled to the compact height by the porosity of the mould and the consolidation constant C :

$$H_m = \frac{C}{\epsilon_m} H_c \quad [m] \quad (2.14)$$

In analogy to the derivation of eq. 2.12 we obtain a parabolic relation

$$\Delta(H_c + H_s) = K_c C \left\{ -R_i + \sqrt{R_i^2 + \frac{2 \Delta P}{\eta_0 K_c C \left(1 + \frac{K_c C}{K_m \epsilon_m}\right)} t} \right\} \quad [m] \quad (2.15)$$

with $H_c + H_s$ [m] the head of the suspension. In case of a negligible interface resistance there is again a quadratic relation between suspension head (compact thickness) and time, which now incorporates the mould permeability K_m [m²] and porosity ϵ_m [-] :

$$\Delta(H_c + H_s) = C H_c = \sqrt{\frac{2 K_c C \Delta P}{\eta_0 \left(1 + \frac{K_c C}{K_m \epsilon_m}\right)}} t \quad [m] \quad (2.16)$$

Because of the linear relation between penetration depth and compact height (eq. 2.14) the pressure drop over the compact and over the mould remains constant. Thus the total pressure drop over the compact layer will also be constant during slip casting.

In classical filtration theory, the characteristics for filtration with constant rate and for constant pressure (negligible filter resistance) or slip casting are, respectively,

Filtration at constant rate :

- The compact grows at a constant rate, i.e. conditions in the consolidated layer remain constant.
- Deviations from linearity in the filtration plot $\Delta P = f(t)$ relate to compact compressibility or to filter clogging.
- Using the relation of Carman-Kozeny (App. 1), it can be shown that compact compressibility causes an increase in the slope of the filtration plot.

Filtration at constant rate (negligible filter resistance); Slip casting :

- The compact is formed with a continually decreasing growth rate, causing continuous changes of the conditions in the consolidation layer.
- Deviations of quadratic behaviour may be caused by filter clogging or inadequate

determination of the start of the filtration process.

- The filtration plot $\Delta H_p(t)$ will not reveal any compact compressibility, for the volumetric mean porosity of the compact remains constant in the condition of a constant absolute pressure drop over the compact [34].

The consolidation zone during filtration

The local solids velocity $V_{s,l}$ [m/s] in the transition zone is small. The local fluid velocity $v_{f,l}$ [m/s] is related to the superficial velocity v_f and the porosity ϵ :

$$v_{f,l} = \frac{1}{(1-\epsilon)} v_f \quad [m/s] \quad (2.17)$$

To estimate the mean shear rate at the particle-fluid interface and the shear stress on the particles in the direction of consolidation, the Carman-Kozeny approach (see App. 1) can be used. The Hagen-Poiseuille relation [35] relates the laminar flow through (cylindrical) pores to the pressure drop (with x the direction of flow) :

$$\pi R^2 v_f = \frac{\pi R^4}{8 \eta_0} \left(-\frac{dP}{dx}\right) \quad [m^3/s] \quad (2.18)$$

The porosity of the transition layer in combination with the filtration rate and the particle diameter gives, through eq. 2.17-18, the pressure drop dP/dx [Pa/m] in the direction of consolidation.

For cylindrical pores the shear rate $\dot{\gamma}$ [s^{-1}] at the wall may be calculated as :

$$\dot{\gamma}_{wall} = -\frac{dv_x}{dr} \Big|_{r=R} = \frac{1}{2\eta_0} \left(-\frac{dP}{dx}\right) R \quad [s^{-1}] \quad (2.19)$$

The shear stress τ_{wall} [N/m^2], exerted by the fluid on the wall in the direction of consolidation, is then given by

$$\tau_{wall} = \tau_{rx} \Big|_{r=R} = \eta \dot{\gamma}_{wall} \quad [N/m^2] \quad (2.20)$$

with $\eta = \eta_0$.

These calculations of the approximate shear rate and the stress on a particle with radius R in the consolidation zone give the viscous drag force F_v [N] on the particles exerted by the fluid flow in the direction of consolidation :

$$F_v = \tau_{wall} \overline{\cos\phi} S = 4R^3 \frac{-dP}{dx} \quad [N] \quad (2.21)$$

with S [m^2] the surface of the spherical particles, and the surface averaged $\overline{\cos\phi} = \frac{2}{\pi}$.

References

- [1] M. Shirato , T. Aragaki , K. Ichimura , N. Ootsuji , J. Chem. Eng. Jpn. 4 [2] (1971) 172-177
- [2] T. Aragaki , S. Hiraoka , I. Yamada , T. Murase , E. Iritani , M. Shirato , J. Chem. Eng. Jpn. 22 [4] (1989) 358-363
- [3] M. Shirato , M. Sambuichi , H. Kato , T. Aragaki , Am. Inst. Chem. Eng. 15 [3] (1969) 405-409
- [4] T. Murase , E. Iritani , J.H. Cho , M. Shirato , J. Chem. Eng. Jpn. 22 [4] (1989) 373-378
- [5] F.M. Tiller , C-D. Tsai , J. Am. Ceram. Soc. 69 [12] (1986) 882-887
- [6] F.M. Tiller , J.R. Crump , F. Ville , in "Fine Part. Process. 2" , ed. P. Somasundran , Am. Inst. Min. Metall. Pet. Eng. Inc. , New York (1980) 1549-1582
- [7] F.M. Tiller , C.S. Yeh , D. Tsai , W. Chen , in "Proc. World 4th Filtr. Congress" , Uplands Press LTD , Croyden England (1986) 4.1-4.12
- [8] F.M. Tiller , H. Cooper , Am. Inst. Chem. Eng. 8 [4] (1962) 445-449
- [9] W.G. Gray , K. O'Neill , Water Resources Research 12 [2] (1976) 148-154
- [10] I. Tosun , M.S. Willis , Chem. Eng. Sci. 38 [3] (1983) 485-487
- [11] I. Tosun , M.S. Willis , Int. J. Multiphase Flow 9 [6] (1983) 763-766
- [12] M.S. Willis , I. Tosun , R.M. Collins , in "The 2nd World Filtr. Congress" , Uplands Press LTD , Croyden England (1979) 629-636
- [13] M.S. Willis , R.M. Collins , W.G. Bridges , Chem. Eng. Res. Des. 61 (1983) 96-109
- [14] M.S. Willis , R.M. Collins , S. Bybyk , in " Proc. World 4th Filtr. Congress" , Uplands press LTD , Croyden England (1986) 1.19-1.31
- [15] I.A. Aksay , C.H. Schilling , Adv. in Ceramics 9 (1984) 85-93
- [16] P.C. Carman , Trans. Inst. Chem. Eng. 16 (1938) 168-188
- [17] P.H. Hermans , H.L. Bredée , Recueil 54 (1935) 680-700
- [18] M.E. Tadros , I. Mayes , in "Fine Part. Process. 2" , ed. P. Somasundran , Am. Inst. Min. Metall. Pet. Eng. Inc. , New York (1980) 1583-1593
- [19] M.E. Tadros , I. Mayes , in " The 2nd World Filtr. Congress" , Uplands Press LTD, Croyden England (1979) 67-71
- [20] J.H.D. Hampton , S.B. Savage , R.A.L. Drew , J. Am. Ceram. Soc. 71 [12] (1988) 1040-1045
- [21] K. Stamatakis , C. Tien , Chem. Eng. Sci. 46 [8] (1991) 1917-1933
- [22] T.J. Fennelly , J.S. Reed , J. Am. Ceram Soc. 55 [5] (1972) 264-268
- [23] D.S. Adcock , I.C. McDowall , J. Am. Ceram. Soc. 40 [10] (1957) 355-362
- [24] F.F. Lange , K.T. Miller , Am. Ceram. Soc. Bull. 66 [10] (1987) 1498-1504
- [25] K. Rietema , Chem. Eng. Sci. 2 (1953) 88-94

- [26] J. Dodds , G. Baluais , D. Leclerc , in "Disorder and Mixing" , eds. E. Guyon et al. , Kluwer Acad. Publ. (1988) 163-183
- [27] R.L. Baird , M.G. Perry , *Filt. & Sep.* (1967) 471-474
- [28] C.R. Ethier , R.D. Kamm , *J. Membrane Sci.* 43 (1989) 19-30
- [29] I. Tosun , M.S. Willis , in "Proc. World 4th Filtr. Congress" , Uplands Press LTD, Croyden England (1986) 4.13-4.20
- [30] J.D. Sherwood , G.H. Meeten , C.A. Farrow , N.J. Alderman , *J. Chem. Soc. Faraday Trans.* 87 [4] (1991) 611-618
- [31] D.E. Smiles , *Chem. Eng. Sci.* 33 (1978) 1355-1361
- [32] D.E. Smiles , J.M. Kirby , *Sep. Sci. & Techn.* 22 [5] (1987) 1405-1423
- [33] D.R. Sperry , *Met. Chem. Eng.* 15 (1916) 198-203
- [34] B.F. Ruth , G.F.H. Montillon , R.E. Montonna , *Ind. Eng. Chem.* 25 (1933) 76-82 & 153-161
- [35] J. M. Smith , E. Stammers , L.P.B.M. Janssen , *Fysische Transportverschijnselen I*, DUM BV , Delft Holland (1981) page 15

2.3 Modelling centrifugal densification

To describe the sedimentation of a particle in a suspension, resulting in the rate of compact growth during centrifugation, we use the coordinate system of figure 2.4 .

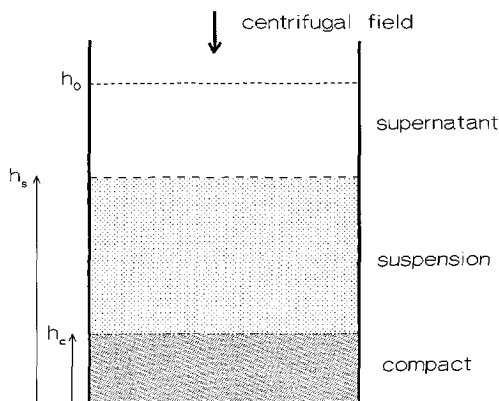


Figure 2.4 The coordinate system used to derive the equation of compact growth in case of centrifugal densification

During centrifugation a sedimenting particle experiences a friction force as a result of fluid displacement. The friction force F_v [N] on a spherical particle with radius R [m], while moving at a constant (sedimentation) velocity v_s [m/s] through a viscous medium with viscosity η_0 [Pa s], is given by Stokes law [1] :

$$F_v = 6 \pi \eta_0 R v_s = f_0 v_s \quad [N] \quad (2.22)$$

with friction factor f_0 [Ns/m]. Stokes law applies in case of the absence of hydrodynamic interactions between the moving spheres and in the absence of osmotic pressure influence, i.e. at infinitesimally small particle concentrations resp. a uniform particle distribution or a consolidation velocity resulting in $Pé > 1$ (eq. 2.1).

In a diluted system particle deviations from sphericity can be treated as an increase of the friction factor, thus formally increasing the hydrodynamic radius of a particle [2,3]. The effective friction factor f_{eff} [N s/m] deviates from f_0 [N s/m] by a factor f [-], the frictional ratio :

$$F_v = f_{eff} v_s = f f_0 v_s \quad [N] \quad (2.23)$$

In a concentrated suspension, the transport of particle volume must be compensated by an opposite flow of the medium. After correcting for the counterflow of fluid, the mean sedimentation velocity of particles may still be smaller than Stokes velocity [4]. This is due to hydrodynamic interactions and to deviations from sphericity, and can be accounted for as an increase of the effective medium viscosity :

$$f = \eta_r = \frac{\eta}{\eta_0} \quad [-] \quad (2.24)$$

Through this effect the frictional ratio f [-] or relative viscosity η_r [-] becomes dependent on the volume fraction of particles, the sphericity of the particles and the shear rate. The flow of the liquid and the hydrodynamic interaction between the moving particles affect the ordering in the consolidation zone.

The Krieger-Dougherty relation [5] relates the particle volume fraction of a suspension to the viscosity :

$$\eta_r = \left(1 - \frac{\phi_v}{\phi_{\max}}\right)^{-[\eta] \phi_{\max}} \quad [-] \quad (2.25)$$

with η_r the relative viscosity, ϕ_v [-] the particle volume fraction, $[\eta]$ [-] the intrinsic viscosity of the particles (in case of spherical particles $[\eta] = 2.5$), and ϕ_{\max} [-] the maximum volume fraction.

The centrifugal force F_g [N] on a spherical particle with radius R [m] suspended in a medium is given by :

$$F_g = \frac{4}{3} \pi R^3 \Delta \rho g \quad [N] \quad (2.26)$$

with $\Delta \rho$ [kg/m³] the difference between particle and medium density, and g [m/s²] the applied centrifugal field.

The force on the particle results in the sedimentation velocity v_s [m/s], relative to the surrounding medium :

$$\begin{aligned} v_s(t) &= \frac{2 R^2 \Delta \rho g}{9 \eta_0 \eta_r} \left[1 - \exp\left(-\frac{9 \eta_0 \eta_r}{2 R^2 \Delta \rho} t\right) \right] \\ &= v_{s,\infty} \left[1 - \exp\left(-\frac{g}{v_{s,\infty}} t\right) \right] \quad [m/s] \end{aligned} \quad (2.27)$$

In case of submicrometer α -alumina particles suspended in water 99 % of the stationary

velocity $v_{s,\infty}$ [m/s] is reached within $1 \mu\text{s}$, so that the non-stationary part of the sedimenting velocity may be neglected.

Compact growth rate

For a volume element at the boundary between the compact and the suspension, the flux balance of the solid and liquid volumes per unit area is [1,2] :

$$v_{s,c} \phi_v = -v_{l,c} (1 - \phi_v) \quad [m/s] \quad (2.28)$$

with $v_{s,c}$ [m/s] the local particle velocity, and $v_{l,c}$ [m/s] the local counter flow velocity of the displaced fluid (the centrifuge tube as coordinate system).

The particle velocity relative to the surrounding fluid is then

$$v_s = v_{s,c} - v_{l,c} = \left(1 + \frac{\phi_v}{1 - \phi_v}\right) v_{s,c} \quad [m/s] \quad (2.29)$$

Rewriting eq. 2.27 for the centrifuge tube as reference system for particle motion we obtain :

$$v_{s,c} = \frac{1}{\left(1 + \frac{\phi_v}{1 - \phi_v}\right)} \frac{2 R^2 \Delta \rho g}{9 \eta_0 \eta_r} \quad [m/s] \quad (2.30)$$

For an incompressible compact with a uniform porosity ϵ_c [-] a volume balance over compact and suspension layer gives

$$h_c \phi_v + (h_0 - h_s) \phi_v = h_c (1 - \epsilon_c) \quad [m] \quad (2.31)$$

and

$$v_{s,c} = \frac{h_0 - h_s(t)}{t} \quad [m/s] \quad (2.32)$$

The compact growth during centrifugation is then given by :

$$h_c(t) = \frac{1}{C} v_{s,c} t = \frac{1}{C} \frac{1}{\left(1 + \frac{\phi_v}{1 - \phi_v}\right)} \frac{2 R^2 \Delta \rho g}{9 \eta_0 \eta_r} t \quad [m] \quad (2.33)$$

The compact is capable of transmitting lateral stresses during centrifugation. The mean network stress (with the normal in the direction of densification) is :

$$\tau_{\text{network}}(t) = (1 - \varepsilon)(\rho_{\text{alumina}} - \rho_w) g h_c(t) \quad [\text{Pa}] \quad (2.34)$$

The consolidation zone during centrifugation

In centrifugation the motion of particles in the suspension is influenced by the displacement of the fluid. The viscous force F_v [N] on a particle can be seen as the product of the shear stress on the particle surface τ_{wall} [N/m²], averaged in the direction opposite to the particle translation, and the particle surface S [m²] :

$$F_v = \tau_{\text{wall}} \overline{\cos\phi} S \quad [\text{N}] \quad (2.35)$$

Combining eqs. 2.20, 2.23-24, 2.27 and 2.35, this results in

$$\dot{\gamma}_{\text{wall}} = \frac{\pi R \Delta\rho g}{6 \eta_0 \eta_r} \quad [1/\text{s}] \quad (2.36)$$

Under these conditions further densification of the consolidation zone caused by the centrifugal force on the particles (eq. 2.26) is opposed by fluid flow in the opposite direction.

The conditions in the consolidation zone depend on the compressibility of the compact. In case of a very compressible compact the counterflow of fluid exerts a viscous force opposing further densification while in case of an incompressible compact this force remains absent.

References

- [1] J.F. Richardson , W.N. Zaki , Trans. Inst. Chem. Eng. 32 (1954) 35-53
- [2] R. Buscall , L.R. White , J. Chem. Soc. , Faraday Trans. 1, 83 (1987) 873-891
- [3] A.A. Zick , G.M. Homsey , J. Fluid Mech. 115 (1982) 13-26
- [4] R. Buscall, I.J. MacGowan, Faraday Discuss. Chem. Soc. , 76 (1983) 277-290
- [5] I.M. Krieger , Adv. Colloid & Interface Sci. 3 (1972) 111-136

Chapter 3

Modelling the rheology of concentrated suspensions

3.1 Introduction to rheology

Rheology produces information about the properties of a suspension. The rheological behaviour of a colloidal suspension is influenced by [1-3] :

- the viscosity of the medium (depends on temperature)
- the concentration of particles
- the rigidity of the particles
- the particle shape and size distribution
- interactions between particles (interaction potentials depend on temperature ; the number of interactions per unit time depends on flow type and shear rate)
- spatial ordering of particles, which depends on shear rate and flow history; flow history should not be neglected when time dependent or irreversible ordering effects occur

The central problem in rheology is how a measured rheological response is related to microscopic suspension properties, and then to quantify found relations. This is especially difficult for concentrated suspensions, where interactions between more than two particles occur. And then there is always the difficulty of finding experimental procedures which result in correct and reproducible results. This problem is often underestimated.

For our investigations we need a rheological model for concentrated colloidal suspensions, in which it is possible to identify suspension properties which directly affect the densification of a particle bed. As discussed in Chapter 2, there will be a consolidation zone when a suspension is concentrated. In this zone densification is affected by the drag effect, depending on the parameters q (coordination number) and l^2 (interaction parameter). These parameters describe the mobility of particles relative to each other, because the drag on neighbouring particles opposes a particle's own motion.

References

- [1] I.M. Krieger , Adv. in Colloid & Interface Sci. **3** (1972) 111-136
- [2] J. Mewis , A.J.B. Spaul , Adv. Colloid & Interface Sci. **6** (1977) 173-200
- [3] J. Mellema , C. Blom , R.J.J. Jongschaap , "Inleiding in de reologie" , Kluwer technische boeken , 2nd edition (1986) 99-158

3.2 Modelling the rheology of concentrated suspensions

In case of a stable suspension with a particle volume fraction not exceeding 0.05, the relation between the relative viscosity η_r [-] and the particle volume fraction ϕ_v [-] is given by Einstein's law of viscosity for a suspension of uncharged hard spheres [1] :

$$\eta_r = 1 + [\eta] \cdot \phi \quad [-] \quad (3.1)$$

with intrinsic viscosity $[\eta]$ [-]. Such a suspension behaves as a Newtonian liquid. The intrinsic viscosity depends on the shape and size distribution of the suspended powder. In case of monodisperse spheres $[\eta] = 2.5$. When the particle shape deviates from sphericity, like with our α -alumina particles, the intrinsic viscosity exceeds 2.5.

The viscosity of more concentrated stable suspensions deviates from Einstein's law because of the (hydrodynamic) interaction between the particles. In general, concentrated colloidal suspensions show non-Newtonian behaviour. An example is the shear thinning behaviour of concentrated stable suspensions. Shear thinning is shown in figure 3.1.

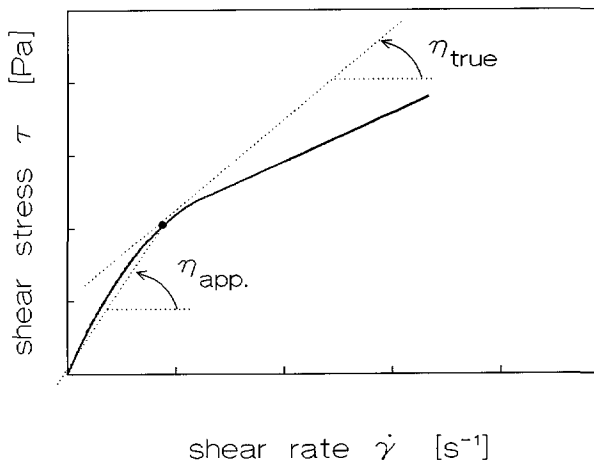


Figure 3.1 Flow curve of a shear thinning suspension

With flocculated suspensions shear thinning indicates the disruption of flocs by the shear forces in the flowing medium. The shear thinning depends on the strength of the inter-particle bonds and on the mean coordination number of particles. In case of stable suspensions shear thinning is caused by particle ordering when the shear rate increases. The transition between disordered and ordered systems will be around $Pé = 1$:

$$Pé = \frac{\dot{\gamma}}{kT/(6\pi\eta_0 R^3)} \quad [-] \quad (3.2)$$

In more concentrated suspensions the shear thinning transition shifts to lower Péclet numbers [2].

The relative viscosity, in the limits of infinitely low (maximum disordered structure) or infinitely high shear (maximum ordering of structure), is called the low shear limiting viscosity $\eta_{r,0}$ [-] and the high shear limiting viscosity $\eta_{r,\infty}$ [-] respectively.

Stable suspensions are Newtonian in both the low and high shear limit, while flocculated suspensions are only Newtonian at high shear. A double logarithmic plot of the flow diagram is used to obtain the relative viscosity (fig. 3.2) in the shear limits, $\eta_r = 1 + \Delta/\tau_N$

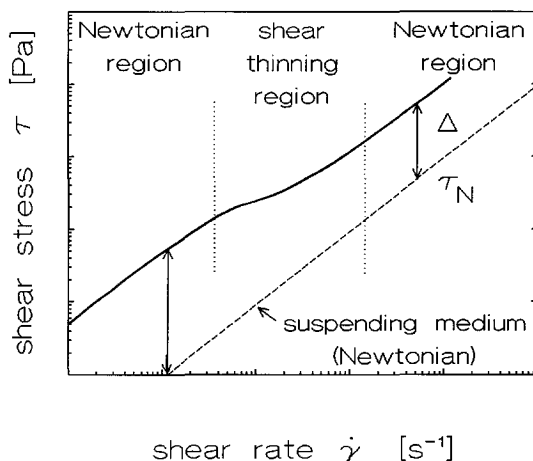


Figure 3.2 Typical shear thinning curve in log-log representation

The value of $\eta_{r,\infty}$ is found by extrapolation (to infinite shear) from measurements performed in the intermediate shear regime. The empirical Sisko relation is a most useful tool for such extrapolations :

$$\tau(\dot{\gamma}) = (\eta_{r,\infty} \eta_0) \dot{\gamma} + C \dot{\gamma}^n \quad [Pa] \quad (3.3)$$

The regime and magnitude of the shear thinning behaviour is determined by the constants C [Pa sⁿ] and n [-].

The Krieger-Dougherty relation

The hydrodynamic interaction between particles in a concentrated suspension can be described in three different models [3] :

- the mean field model
- the free surface model
- the lubrication model

Many (semi-)empirical relations for the effect of the particle volume fraction on the viscosity of a stable suspension [4-11], are based on these models.

In mean field theories, a particle added to a suspension will effectively experience this suspension as a continuum with a viscosity equal to the suspension viscosity. Brinkman [9] used mean field theory and obtained the expression

$$\eta_r = \frac{1}{1 - \frac{5}{2} \phi_v} \quad [-] \quad (3.4)$$

This equation is a special case of the (semi-empirical) relation by Krieger and Dougherty [4] :

$$\eta_r = \left(1 - \frac{\phi_v}{\phi_{\max}}\right)^{-\kappa} \quad [-] \quad (3.5)$$

with exponential factor κ [-] and maximum volume fraction ϕ_{\max} [-].

In contrast to other (semi-)empirical relations, an important quality of the Krieger-Dougherty relation is that it can be applied at low, intermediate and high particle concentrations without alteration of its empirical constants [3]. In a suspension of spheres, at low volume fractions, the Krieger-Dougherty relation yields Einstein's law of viscosity (eq. 3.1). The Krieger-Dougherty relation constitutes a most promising approach to describe the relative viscosity of suspensions of sphere-like particles with hard-sphere interaction over the whole range of solids contents.

A more detailed representation of the Krieger-Dougherty relation, in which it is attempted to account for differences in particle shape, ordering and electroviscous effects, is written [4] :

$$\eta_{r,\dot{\gamma} \rightarrow a} = f_{\dot{\gamma} \rightarrow a} = \left(1 - \frac{\phi_v}{\phi_{\max,\dot{\gamma} \rightarrow a}}\right)^{-|\eta| \phi_{\max,\dot{\gamma} \rightarrow a}} \quad [-] \quad (3.6)$$

with ϕ_v [-] the effective particle volume fraction, $|\eta|$ [-] the intrinsic viscosity of the particles (in case of spherical particles $|\eta| = 2.5$), and $\phi_{\max,\dot{\gamma} \rightarrow a}$ [-] the maximum volume

fraction. The value of ϕ_{\max} is empirically found by extrapolation to infinite relative viscosity, $\eta_r, \dot{\gamma} \rightarrow \infty$. It represents the idea of a volume fraction where the dispersed particles lock into a rigid structure, blocking shear.

ϕ_{\max} should depend on the degree of particle ordering in the suspension (determined by the imposed shear rate) as well as shape of the particles and the size distribution. At low shear rates (maximal disorder) ϕ_{\max} is believed to correspond with the density of a random loose packing (rlp), and in the high shear region (maximal ordering) with random dense packing (rdp) [12]. An increased width of the particle size distribution results in an increased ϕ_{\max} . Deviations from particle sphericity tend to decrease ϕ_{\max} [13,14].

For different powder characteristics, experimental operations and simulation procedures, a wide range of values for ϕ_{\max} has been reported in literature (experimental work [2,5,7,8,13,15-19], computer simulations [14,20,21]).

For irregular sand particles with a log-normal distribution of $\sigma = 0.46$, comparable with our A16SG-F powder, the experimental results were [18] :

$$\text{rlp} : \phi_{\max} = 0.57 \pm 0.03$$

$$\text{rdp} : \phi_{\max} = 0.63 \pm 0.01$$

The Giant-Floc model

In solid materials, deformation occurs when the yield stress is locally exceeded. When the microstructure of a material allows for mechanisms of atomic transport, plastic deformation may occur. Plastic deformation takes place in regions of stress concentration. For example, when deforming steel, the deformation will be concentrated in slip planes [22]. These slip planes emerge where certain crystal planes, in which minimal energy for material transport is needed, may slide in the direction of the highest shear stress. At increasing deformation, the number of slip planes increases. The structure between the slip planes remains undeformed.

Due to the fractal nature of discrete flocs [23], the percolation threshold in flocculated suspensions is considerably lower than the percolation threshold of $P_c = 0.25$ in simple cubic lattices [14]. In moderately and highly concentrated flocculated suspensions, such as used by us, the structure of the system is thus a network of particles, filled with water. For a powder, the particle coordination number and the strength of particle attraction are the characteristic parameters of the particle network.

On the analogy of solid materials, we expect the deformation of the particle network to be restricted to places where stress is concentrated. During shear, network destruction and ordering of particles at increasing shear rate will result in shear thinning behaviour.

This situation has been described in the Giant-Floc model of Stein, van Diemen and Schreuder [24,25]. The Giant-Floc model is based on a number of assumptions :

- In moderately and highly concentrated flocculated suspensions there are no discrete flocs. All particles belong to one single network, the "Giant-Floc".
- Shear will not be uniformly distributed over this network, but concentrates in preferential shear planes. These divide the floc into domains of average thickness A [m].
- Increasing the shear rate results in an increasing number of shear planes.
- The total energy dissipation in a sheared Giant-Floc is caused by individual particle motions in the viscous medium.

The dependence of the number of shear planes on shear rate is a cause of the system's striving for minimum dissipation. Minimum dissipation is achieved by sharing the shear over more shear planes. This implies a characteristic maximum shear rate per plane, related to the strength of the material.

A comprehensive derivation of the equation of the flow model is given by van Diemen en Stein [24]. A schematic representation of a sheared Giant-Floc is shown in figure 3.3 .

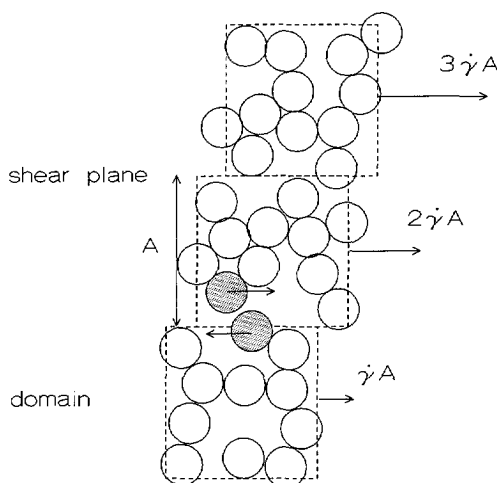


Figure 3.3 A sheared Giant-Floc [24]

Particle collisions in the shear planes will be the result of differences in the velocity of the adjacent domains. When particles from different domains collide (dotted particles in fig. 3.3) their trajectories will be deflected, resulting in two simultaneous particle displacements, each over an average distance δ_0 [m].

A displaced particle will entrain adjacent particles. The number of adjacent particles that will be entrained depends on the number of nearest neighbours, i.e. on the coordination number q [-]. The neighbouring particles are dragged over a fraction l [-] of δ_0 . The

fraction l depends on the interaction between the particles. Thus one encounter in a shear plane will result in a tree of coupled particle displacements in both domains.

The energy dissipation ϵ_i [J] caused by the displacement of the i^{th} particle through the viscous medium equals

$$\epsilon_i = 6\pi\eta_0 R f' \frac{\delta_i}{t_0} \delta_i \quad [J] \quad (3.7)$$

with δ_i [m] the displacement of particle i , and t_0 [s] the time of the encounter.

For this rheological model to describe the influence of l on energy dissipation, the frictional ratio f' [-] should be defined as an operator depending on particle volume fraction, powder properties and particle ordering, but not on the interaction parameter l itself. The importance of such a definition of f' will emerge later.

The total dissipation $\Sigma\epsilon$ [J], due to all combined particle displacements resulting from one encounter in a shear plane (two domains involved), then depends on the parameters q and l in the following way :

$$\begin{aligned} \Sigma\epsilon &= 2 \cdot 6\pi\eta_0 R f' \frac{\delta_0^2}{t_0} \sum_{i=1}^{\infty} \left(\frac{1}{2}ql^2\right)^{i-1} \\ &= 2 \cdot 6\pi\eta_0 R f' \frac{\delta_0^2}{t_0} \frac{1}{1 - \frac{1}{2}ql^2} \quad [J] \end{aligned} \quad (3.8)$$

Duisterwinkel [14] introduced the term $\frac{1}{2}ql^2$ in stead of $(q-1)l^2$ in the original model [24], in order to avoid double counting of particles.

Local values of q in the shear regions may strongly deviate from the mean coordination number. At increasing shear, stress concentration in regions with higher coordination numbers will level off the distribution of q .

On the average, particles in adjacent shear planes will collide after a particle displacement given by $\Delta \overline{\cos u}$ [m], with Δ^2 [m²] the mean available surface of a particle in a shear plane. The angle u [-] is given by the angle between the main direction of motion and the connecting line between the two particles to be collided, $\overline{\cos u} = \frac{2}{\pi}$. The time s [s] between two successive encounters in a shear plane is then given by

$$s = \frac{\Delta \overline{\cos u}}{\dot{\gamma} A} \quad [s] \quad (3.9)$$

with A [m] the distance between the shear planes ($1/A$ equals the total shear plane area per unit volume).

The duration of one encounter t_0 [s] is given by

$$t_0 = \frac{\delta_0}{\dot{\gamma} A \cos u} \quad [s] \quad (3.10)$$

The rate of energy dissipation per unit volume $\dot{\epsilon}$ [W/m³] equals the product of collision frequency (1/s), the energy dissipation involved with one encounter ($\Sigma\epsilon$) and the total number of the particles residing in the shear planes per unit volume :

$$\begin{aligned} \dot{\epsilon} &= \eta_{app.} \dot{\gamma}^2 = \frac{1}{s} \Sigma\epsilon \frac{1}{A\Delta^2} \\ &= 2.6\pi\eta_0 R f' \left(\frac{A\delta_0}{\Delta^3}\right) \dot{\gamma}^2 \frac{1}{1 - \frac{1}{2}ql^2} \quad [J/m^3s] \end{aligned} \quad (3.11)$$

The viscosity of a suspension is then

$$\eta_{app.} = 2.6\pi\eta_0 R f' \left(\frac{A\delta_0}{\Delta^3}\right) \frac{1}{1 - \frac{1}{2}ql^2} \quad [Pas] \quad (3.12)$$

Particle packing from suspensions involves high shear rates to reduce process time. To establish a link between rheology and consolidation we will be concerned with the relative viscosity of suspensions towards the limit of infinite shear, $\eta_{r,\infty}$. Here, our goal will be to relate rheology and compaction processes through the drag parameters l^2 and q . The latter is, as will be shown, proportional to ϕ_v .

Equation 3.12 describes the shear dependence of the apparent viscosity. After some rearranging, it can be seen that the shear dependence is determined by the dimensionless factors A/R , f' , δ_0/R , q and Δ/R .

The distance of the shear planes A [m] and the frictional ratio f' [-] which is influenced by ordering in the suspension, are strongly dependent on shear rate. In the limit of infinite shear, the situation of a totally destructed Giant-Floc, A equals about $2R$. At infinite shear maximum particle ordering exists, decreasing the frictional ratio to f'_∞ .

The deflection distance δ_0 [m] is believed to be weakly dependent on shear rate. At a high shear rate, based on Batchelor-Green trajectories, δ_0 [m] has been estimated [24] to be

$$\frac{\delta_0}{R} \approx 0.1 \quad [-] \quad (3.13)$$

In a highly ordered suspension of spheres the mean number of nearest neighbours q (at distance $2R$ of the centre of a chosen particle) can be estimated with

$$q = q_0 \frac{\phi_v}{\phi_{\max, \infty}} \quad [-] \quad (3.14)$$

where $q_0 = 6$, corresponding with the mean coordination number of a random close particle packing [20,26]. In case of random packings of log-normal distributed powders, the value of σ does not significantly influence q_0 [27].

In concentrated suspensions the mean available surface of a particle in a shear plane, Δ^2 [m^2], is only weakly dependent on ordering effects and particle volume fraction. Following Schreuder and Stein [25], we assume

$$\frac{R}{\Delta} \approx 0.5 \quad [-] \quad (3.15)$$

According to the above considerations, evaluation of the apparent viscosity (eq. 3.12) in the limit of infinite shear ($\eta_{app} \rightarrow \eta_{true}$) yields

$$\eta_{r,\infty} = f'_{\infty} \frac{1}{1 - 3 \frac{\phi_v}{\phi_{max,\infty}} l^2} \quad [-] \quad (3.16)$$

The frictional ratio f is an operator relating the total dissipation of a sheared system (due to individual translational and rotational particle movements, hydrodynamic interaction and particle drag) with the total dissipation of the medium at same shear rate (see eq. 2.24). In the high shear limit f is determined by the particle volume fraction, intrinsic powder properties and particle drag.

For a flocculated suspension, by combining eqs. 2.24 and 3.16, f can be expressed as

$$f = f'_{\infty} \frac{1}{1 - 3 \frac{\phi_v}{\phi_{max}} l^2} \quad [-] \quad (3.17)$$

Based on the Giant-Floc model, while operator f'_{∞} being independent on l , we now obtain a relation for f (in the limit of high shear) linear dependent on a term solely influenced by particle drag, determined by the product of ql^2 . In the limit of high shear, in both stable and flocculated suspensions, all particles are in relative motion. In this limit, although the drag effect will deviate, no significant difference will exist between the structure of operator f in flocculated or stable systems.

Thus eq. 3.17 should also apply for stable suspensions, now with $l^2 = l_s^2$ accounting for the influence of particle drag in a stable system.

According to the above considerations, using the Krieger-Dougherty relation (eq. 3.6) to describe the relative viscosity of stable suspensions, eq. 3.16 can be rewritten as

$$\eta_{r,\infty} = \left(1 - \frac{\phi_v}{\phi_{\max,\infty}}\right)^{-|\eta| \phi_{\max,\infty}} \cdot \frac{1 - 3 \frac{\phi_v}{\phi_{\max,\infty}} l_s^2}{1 - 3 \frac{\phi_v}{\phi_{\max,\infty}} l^2} \quad [-] \quad (3.18)$$

with $l_s \leq l \leq 1$. This rheological relation is valid for more or less concentrated stable as well as flocculated suspensions. It implies ordering of the particles at high shear. The parameters $|\eta|$ and $\phi_{\max,\infty}$ are intrinsic powder qualities, which do not depend on the colloidal stability of a suspension and/or the particle volume fraction.

In our strive to control the microstructure of a wet particle packing, because it's strong influence on the properties of the final ceramic product, we have obtained a rheological relation which depends on the mean coordination number q (q is related to ϕ_v through eq. 3.14) and the interaction parameter l^2 . In colloidal consolidation, these drag parameters influence the mobility of particles in the consolidation zone. Through the drag parameters q and l^2 now a relation between rheology and consolidation has been established.

At a given volume fraction the interaction parameter l^2 governs the drag effect (eq. 3.18). l^2 is determined by the strength of attraction between neighbouring particles. In case of stable suspensions ($l^2 = l_s^2$), eq. 3.18 reduces to the Krieger-Dougherty relation. When l^2 increases, this implies a correction factor due to increased particle drag, resulting in an increased viscosity. Our rheological model further implies (eq. 3.18) that the strength of the particle attraction (l^2) determines the particle volume fraction at which blocking of particles occurs. In case of limited particle drag, $l^2 < 1/3$, the divergence of $\eta_{r,\infty}$ to infinity (the blocking of particles) occurs at a volume fraction of $\phi_{\text{div.}} = \phi_{\max,\infty}$. However, when l^2 exceeds $1/3$, $\phi_{\text{div.}}$ shifts to lower values, given by $\phi_{\text{div.}} = \phi_{\max,\infty} / (3l^2)$. The influence of the strength of attraction between particles (in terms of l^2) on $\phi_{\text{div.}}$ is shown in fig. 3.4.

In case of ideal compaction the fluid flow exerts shear stresses on the particles, on the average in the direction of densification. This tends to densify the original random and open stacked consolidation zone. In practice, the shear rate during densification is extremely high. According to equation 2.19, during filtration or slip casting shear rates exceeding 10^4 s^{-1} are expected in the consolidation zone (filtration with 10^5 Pa/mm).

When particle motion in the consolidation zone is blocked because of strong particle drag ($\eta_{r,\infty} \rightarrow \infty$), densification of the consolidation zone is impossible. When compacting stable or weakly flocculated suspensions, i.e. $l^2 < 1/3$, blocking will occur at a particle volume fraction given by $\phi_{\max,\infty}$ (eq. 3.16). These suspensions can thus be densified to $\phi_{\max,\infty}$, the density of the random dense packed particle compact. With strongly flocculated suspensions, blocking will occur at a lower volume fraction, depending on the value of l^2 . These suspensions can be consolidated to $\phi_{\text{div.}} = \phi_{\max,\infty} / (3l^2)$.

Now rheological measurements can be done which indicate, through interpretation in terms of the drag parameters q and l^2 , if and to which extent the consolidation zone of a suspension can be densified.

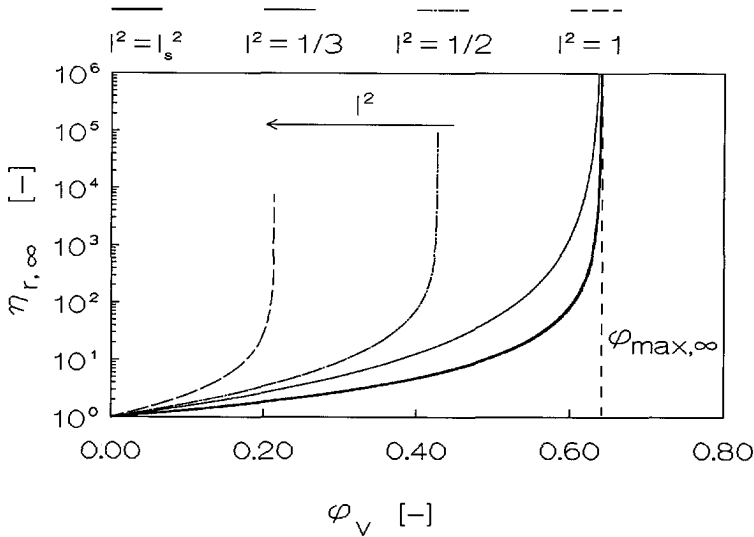


Figure 3.4 The high shear limiting viscosity as a function of particle volume fraction at different interaction parameters l^2 (eq. 3.18)

References

- [1] P.C. Hiemenz, "Principles of colloid and surface chemistry", Marcel Dekker Inc., N.Y. (1986) 187-193
- [2] J.C. van der Werff, C.G. de Kruif, J. Rheol. **33** [3] (1989) 421-451
- [3] A.A. Potanin, N. B. Uriev, J. Colloid & Interface Sci. **142** [2] (1991) 385-395
- [4] I.M. Krieger, Adv. Colloid & Interface Sci. **3** (1972) 111-135
- [5] A.A. Zick, G.M. Homsey, J. Fluid Mech. **115** (1982) 13-26
- [6] H. Eilers, Z. Schr. **97** [3] (1941) 313-321
- [7] D. Bedeaux, J. Colloid & Interface Sci. **118** [1] (1987) 80-86
- [8] P. Mills, P. Snabre, Progress & Trends in Rheol. **11** (1988) 105-108
- [9] H.C. Brinkman, Appl. Sci. Res. vol A1 (1947) 27-67

- [10] J. Happel , J. Appl. Phys. 88 (1957) 197
- [11] N.A. Frankel , A. Acrivos , Chem. Eng. Sci. 23 (1967) 847
- [12] A. Duisterwinkel , "Clean coal combustion with in situ impregnated sol-gel sorbent", thesis TU Delft (1991)
- [13] R.J. Wakeman , Powder Techn. 11 (1975) 297-299
- [14] W. Soppe , Powder Techn. 62 (1990) 189-196 , incl. personal comm.
- [15] G.Y. Onoda , E.G. Liniger , Phys. Rev. Lett. 64 (1990) 2727-2732
- [16] C.G. de Kruif et al. , J. Chem. Phys. 83 (1985) 4717-4722
- [17] R. Buscall , I.J. McGowan , Faraday Discuss. Chem. Soc. 76 (1983) 277-290
- [18] J.W. Goodwin , in " The Structure, Dynamics and Equilibrium properties of colloidal systems" , eds. D.M. Bloor , E. Wyn-Jones , Kluwer Acad. Publ. (1990) 659-679
- [19] H.Y. Sohn , C. Moreland , Can. J. Chem. Eng. 46 (1968) 162-165
- [20] G.T. Nolan , P.E. Kavanagh , Powder Techn. 72 (1992) 149-155
- [21] K.H. Schlüssler , L. Walter , Part. Charact. 3 (1986) 129-135
- [22] P. Jongenburger , "Kennis der metalen, deel 1" , 11th ed. DUM Delft (1976) 193-215
- [23] Y. Adachi , S. Ooi , J. Colloid & Interface Sci. 135 [2] (1990) 374-384
- [24] A.J.G. van Diemen , H.N. Stein , Rheol. Acta 22 (1983) 41-50
- [25] F.W.A.M. Schreuder , H.N. Stein , Rheol. Acta 26 (1987) 45-54
- [26] M.J. Powell , Powder Tech. 25 (1980) 45-52
- [27] J.Dodds , M. Leitzement , in "Proceedings in Physics 5 : Physics of finely divided matter" , Eds. N. Bocarra , M. Daoud , Springer-Verlag Berlin (1985) 56-75

Chapter 4

Rheological investigation of concentrated α -alumina suspensions

4.1 Suspension preparation and characterization

Suspension preparation is the beginning of the colloidal route to fine grained ceramics (figure 1.1). Optimization of the suspension preparation implies control of [1-4] :

- the particle size, and the particle size distribution
- powder impurities (including contamination by dust particles and micro-organisms)
- the colloid stability of the suspension
- aging effects

The powder

Suspensions were all prepared from one batch of Alcoa's A16SG α -alumina powder (4T67581). According to the manufacturer this powder contained the following impurities and dopants : SiO_2 0.025 m%, Fe_2O_3 0.01 m%, Na_2O 0.08 m%, MgO 0.05 m%, CaO 0.01 m% and B_2O_3 0.001 m% .

As received, the powder has a broad particle size distribution. The distribution was determined by static light scattering (Malvern Mastersizer, Malvern Instr.) in a transparent ($\phi_v \approx 10^{-4}$) suspension at pH = 3 (HNO_3), assuming equivalent spheres [5]. The histogram (figure 4.1), in terms of the partial particle volume in traject $\Delta(\ln D)$ around $\ln D$, resembled a log-normal distribution, i.e.

$$f_i [-] = \frac{1}{\sqrt{2\pi} \sigma} \exp\left[-\frac{1}{2}\left(\frac{\ln D - \ln D_g}{\sigma}\right)^2\right] d \ln D$$

It has a geometric mean particle diameter D_g^v of $0.56 \mu\text{m}$ and a standard deviation of $\sigma = 0.89$ ($\sigma = \ln \sigma_g$, with σ_g the geometric standard deviation). The diameters at which the volume of under-sized particles equals resp. 10, 50 and 90 % of the total particle volume, were $D_{v,10} = 0.23 \mu\text{m}$, $D_{v,50} = 0.61 \mu\text{m}$ and $D_{v,90} = 2.62 \mu\text{m}$. After a heat treatment of 10 hrs at 120°C , to ensure absence of condensed water, the BET surface of A16SG [6] was determined with a Sorpty 1750 (Carlo Erba Instr.), to be $11.6 \pm 0.3 \text{ m}^2/\text{g}$.

Fractionation

To remove hard agglomerates, oversized particles and dust, the powder was classified by sedimentation (eq. 2.30). In dilute suspensions ($\phi_v < 0.05$), alumina particles with a

diameter exceeding $0.86\ \mu\text{m}$ ($\text{Pé} > 1$, eq. 2.1) may be removed by sedimentation. These particles will settle at a rate over $0.42\ \text{cm/hr}$.

While slowly stirring, using a alumina blade stirrer, 10 kg of the as received A16SG was added to 170 l of demineralized water ($\sigma = 8.1 \pm 0.1\ \mu\text{S/cm}$ at $21\ ^\circ\text{C}$) in a 200 l PVC vessel with a diameter of about 60 cm. A coagulated suspension resulted, with a volume fraction of about 1.5 v%. The suspension was rezeptized by lowering the pH to 3 (adding HNO_3 , Baker p.a.) under rigorous stirring. After 48 hrs of settling the top layer of the suspension (8 cm, about 20 l), containing the smallest particles, was pumped off. This fraction was coagulated by increasing the pH to 9 (NH_4OH , Merck p.a.), and in 2 days a sediment formed ($\phi_v \approx 0.15$) and the supernatant was decanted. The settling procedure was repeated until about 7.2 kg of fractionated A16SG powder (A16SG-F) was obtained.

Figure 4.1 compares the particle size distributions of A16SG and A16SG-F.

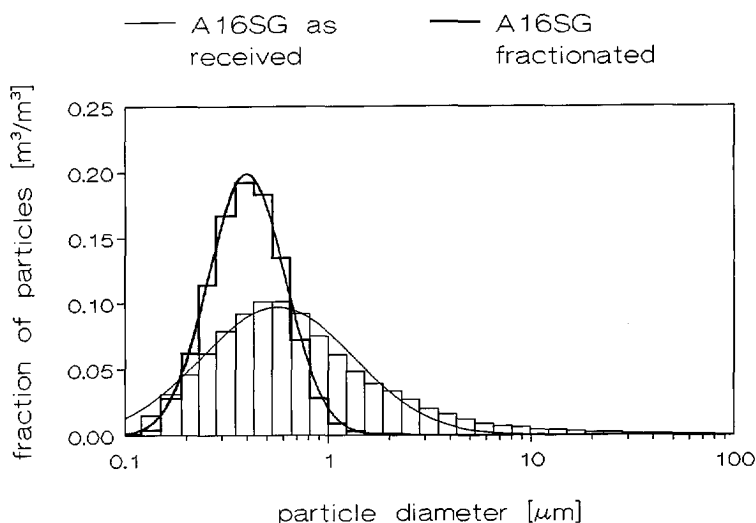


Figure 4.1 The particle size distributions of the A16SG as received and the A16SG-F powder

The fractionated powder has a log-normal distribution, with $D_g^v = 0.40\ \mu\text{m}$ and $\sigma = 0.433$, with $D_{v,10} = 0.23\ \mu\text{m}$, $D_{v,50} = 0.40\ \mu\text{m}$ and $D_{v,90} = 0.68\ \mu\text{m}$.

The BET surface of the powder increased from $11.6 \pm 0.3\ \text{m}^2/\text{g}$ (A16SG a.r.) to $13.4 \pm 0.3\ \text{m}^2/\text{g}$ (A16SG-F). The fractionation has clearly decreased the number of oversized particles,

resulting in a finer powder with a more narrow size distribution. Not all particles over $D = 0.86 \mu\text{m}$ could be removed. At $Pé > 1$ particle diffusion still reduces the sedimentation velocity, and some flow occurred during the removal of the top layers. After evaporating a drop of a peptized and strongly diluted A16SG-F suspension on a sample carrier, electron micrographs of the particles were obtained. Such a micrograph of the fractionated powder is shown in figure 4.2 .

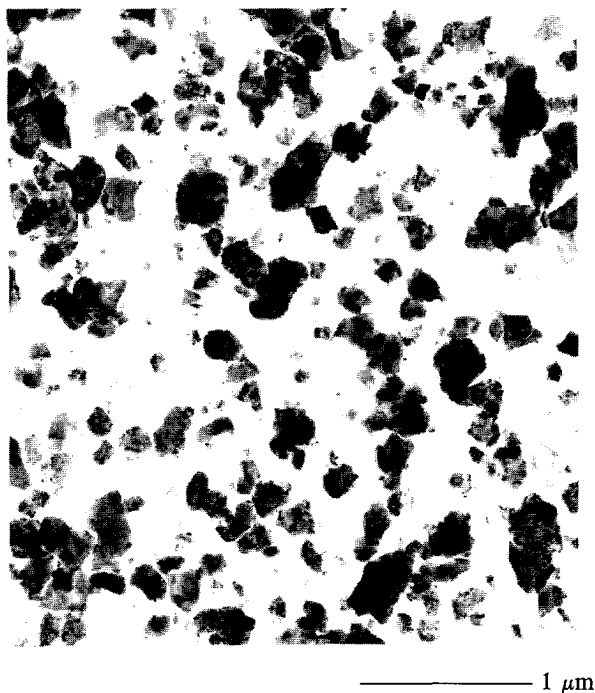


Figure 4.2 TEM micrograph of the A16SG-F powder

Washing the fractionated powder

The fraction A16SG-F was washed by adding (and rigorously shaking) 8 l de-mineralized water (Milli-Q water system, $\sigma = 0.42 \pm 0.03 \mu\text{S}/\text{cm}$ at 21°C) to remove salt and soluble impurities. The suspension remained flocculated ($\text{pH} \approx 9$). After two days of sedimentation the supernatant was decanted. Washing was repeated until the conductivity of the supernatant had decreased below $20 \mu\text{S}/\text{cm}$ (final $\text{pH} \approx 9.3$). This indicates a hydronium concentration of $5.7 \cdot 10^{-5} \text{ M}$ at 25°C [7]). The concentration of

ionic contaminants after washing is thus expected not to exceed $1 \cdot 10^{-4}$ M.

The α -alumina suspensions

A suspension of α -alumina is an electrocratic colloid. The colloid stability is determined by the relative strength of the van der Waals attraction and the electrostatic repulsion between particles. The repulsion is due to the positive surface charge of the particles. It is compensated by a diffuse space charge of opposite sign in the medium. When particles approach each other, overlap of these electrical "double layers" causes the repulsion [8-11]. Controlling the particle surface charge and the reach of the electrical repulsion can be used to influence the stability of the suspension. The thickness of the electrical double layer is of the order of the Debye length κ^{-1} [m]. The Debye length can be changed by altering the electrolyte concentration C [M].

With a 1:3 type electrolyte like $\text{Al}(\text{NO}_3)_3$, at 25 °C the Debye length is given by

$$\kappa^{-1} = (8.03 \cdot 10^9 \sqrt{C})^{-1} \quad [m] \quad (4.1)$$

Flocculation occurs when two particles collide and stick together. The collisions may be due to the thermal motion of the particles or to hydrodynamic forces on the particles in an imposed shear field. An excellent review of the stability criteria in case of fine particle dispersions is given by Chung et al [4].

The surface chemistry of α -alumina particles in water is very complicated [3]. One aspect in our experiments is the relation between the $\text{Al}(\text{NO}_3)_3$ concentration and the colloid stability, for both dilute and more concentrated fractionated A16SG suspensions.

In aqueous α -alumina suspensions, electrostatic stabilization is caused by selective adsorption of hydronium ions [12] and hydrolysed Al^{3+} species [13]. The colloidal stability is governed by the pH of the suspension [14]. Usually alumina suspensions are stabilized near $\text{pH} = 4$, where the particles are positively charged.

The dispersing medium was an aqueous solution of aluminumnitrate $\text{Al}(\text{NO}_3)_3$. In acid, aging of deflocculated α -alumina suspensions increases the pH [3]. Aluminumnitrate acts as a buffer around $\text{pH} = 4$ and keeps the dispersion stable [15].

Suspensions were prepared by adding the washed A16SG-F sediment to demineralized water (Milli-Q water system). As dispersing agent $\text{Al}(\text{NO}_3)_3 \cdot 9\text{H}_2\text{O}$ (Merck, extra pure) was added. All suspensions were prepared and stored in polyethylene (PE) vessels, and stored on a roller bench (bottles rotating at $\approx 1/2$ RPM) to prevent sedimentation.

The electrophoretic mobility (at 25 ± 1 °C) of the particles was measured using a Malvern Zeta-Sizer (Malvern Instr.). For these measurements transparent ($\phi_v < 10^{-4}$) suspensions were prepared by diluting a suspension in its own supernatant. Supernatant of the suspensions was obtained by centrifuging for 2 hrs at about 10.000 g. This gave a clear supernatant for all suspensions. The pH (± 0.05) and conductivity (± 0.02 mS/cm)

of the supernatants were measured at room temperature.

The electrode compartments of the Zeta-Sizer were filled with an $\text{Al}(\text{NO}_3)_3$ -KOH solution, matching the conductivity and pH of the supernatant. The temperature during the measurements was controlled within 0.1 °C. On each sample five measurements were performed. Corrections concerning the temperature dependence of the viscosity of water were applied. Equivalent zeta potentials were calculated assuming a relative small double layer, $\kappa R \gg 100$ (Helmholtz-Smoluchovski limit).

A16SG-F stock suspensions

Two stock suspensions have been used to avoid the influence of aging effects when relating the results from the rheological experiments (section 4.2) with the densification experiments (Chapter 5) to be performed. The two stocks were prepared, as much identical as possible, about 2 days before starting the respective group of experiments. In preparing a stock suspension the following steps have been followed :

- adjusting the particle volume fraction of the A16SG-F sediment
- adding the aluminum nitrate to obtain a stable suspension
- dispersing the suspension in a ball mill
- degassing the suspension

About 6 l of the A16SG-F sediment (containing about 3.6 kg powder) was poured in porcelain dishes and heated to a temperature of 95 °C in a drying oven. After about 4 hrs evaporation the sediment was concentrated to a volume fraction ϕ_v exceeding 0.2 . To determine ϕ_v about 20 ml of the concentrated sedimented was dried to constant weight (120 °C, 4 hrs). The mass fraction and related volume fraction were calculated by means of equations 4.2-3 , using the measured wet W_{wet} [g] and dry W_{dry} [g] weight of the sediment (Mettler AE100 balance, ± 0.05 mg).

$$\phi_m = \frac{W_{\text{dry}}}{W_{\text{wet}}} \quad [-] \quad (4.2)$$

$$\phi_v = \frac{1}{1 + \left(\frac{1}{\phi_m} - 1 \right) \rho_{\text{alumina}}} \quad [-] \quad (4.3)$$

By addition of millipore water the volume fraction was adjusted to a desired volume fraction of 0.20 . The amount of water to be added per gram of sediment, ΔF [-], follows from :

$$\Delta F = \frac{(\phi_{v,old} - \phi_{v,new}) \rho_{water}}{[\rho_{water} + (\rho_{alumina} - \rho_{water}) \phi_{v,old}] \phi_{v,new}} \quad [-] \quad (4.4)$$

The suspension was stabilized by addition of aluminum nitrate to the desired concentration of 0.020 M. To obtain this concentration, taking into account the adsorption of nitrate in the electrical double layer (eq. 4.5), 11.36 ± 0.01 mg $\text{Al}(\text{NO}_3)_3 \cdot \text{H}_2\text{O}$ per gram A16SG-F ($2.26 \mu\text{mol}/\text{m}^2_{\text{A16SG-F}}$) had to be added, which would, without adsorption, give an aluminum nitrate concentration of 0.030 M.

To obtain a completely deflocculated suspension, the suspension was milled for four hrs in an alumina ball mill, filled with alumina balls (diameter ranging from 5 to 20 mm) to just below the surface of the suspension. Due to this dispersing operation air bubbles in the suspension could be observed. Air bubbles were removed by degassing the suspension for 30 minutes at a pressure of about 0.05 bar (Gerhards vacuum system). After degassing, a dip test (see page 54) revealed no remaining aggregates.

A well dispersed suspension of about 4.5 l was thus obtained, with a volume fraction of 0.20 and an aluminum nitrate concentration of 0.020 M. The preparation of the stock suspension did not influence the particle size distribution and specific surface of the A16SG-F powder.

The steady state flow diagram showed the near Newtonian behaviour, which is characteristic for a well dispersed concentrated suspension. The properties of the stock suspension are shown in table 4.1.

Table 4.1 Properties of the A16SG-F stock suspension ($11.36 \text{ mg}_{\text{aluminum nitrate}}/\text{g}_{\text{A16SG-F}}$)

BET surface [m^2/g]	13.4	\pm	0.3
D_g^v [μm] (volume av.)	0.400	\pm	0.001
σ ($= \ln \sigma_g$) [-]	0.433	\pm	0.005
D_g^n [μm] (number av.)	0.238	\pm	0.004
ϕ_v [-]	0.199	\pm	0.001
$C_{\text{aluminum nitrate}}$ [M]			
in supernatant	0.0209	\pm	0.0004
pH	3.95	\pm	0.05
σ [mS/cm]	5.04	\pm	0.02
ζ_{pot} [mV]	53	\pm	2
$\eta_{r,\infty}$ (20 °C) [mPas]	3.0	\pm	0.3

Colloid stability of dilute A16SG-F/H₂O/Al(NO₃)₃ suspensions

The colloid stability of dilute suspensions was investigated by means of the dependence of sedimentation velocity on Al(NO₃)₃ concentration.

At a given horizontal level in a suspension, the particle concentration will decrease in time as a result of sedimentation. In diluted systems the effective light absorption, as a result of light scattering by the particles, is expected to be linear on particle concentration. Thus Beer's law applies [16,17]. Because flocs settle faster than the original particles, the decrease of absorbance in time can be used to discriminate between the various states of colloid stability.

Suspensions of A16SG-F were prepared by adding 0.05 ml of the stock suspension to 15 ml freshly prepared aluminum nitrate standard solutions ($\phi_v \approx 5 \cdot 10^{-4}$). The aluminum nitrate concentrations varied from 0.005 M to 0.05 M with intervals of 0.005 M. The suspensions were stored for two hrs on the roller bench.

In table 4.2 the measured conductivity and pH of the standard solutions, covering the range of 0.005 M to 0.05 M, and the measured zeta potentials of A16SG-F powder in these solutions are given. The measured zeta potentials follow the relationship between zeta potential and pH as reported by Schilling [14] (A16SG with HNO₃ as deflocculant).

Table 4.2 Properties of aluminum nitrate standard solutions

Concentration Al(NO ₃) ₃ [M]	σ [mS/cm]	pH	ζ -potential A16SG-F [mV]
0.0050	1.29	3.81	51.4 ± 2.2
0.0100	2.73	3.65	51.8 ± 0.8
0.0200	5.10	3.48	52.3 ± 1.1
0.0500	1.47	3.25	43.3 ± 3.2

In figure 4.3 the time dependent absorbance for various aluminum nitrate solutions is shown. It was investigated with a Beckman DU-40 spectrophotometer, at a frequency of 550 nm. The suspensions were contained in PMMA tubes of optical quality, with dimensions 1 x 1 x 5 cm³. The light beam traversed the tube at a height of 2.5 centimetres. Three types of time dependent absorbance behaviour can be distinguished. Up to 0.020 M Al(NO₃)₃, the rate at which the optical absorbance decreases is relatively small. In the initial (linear) part of curve A, the slope is $1.37 \cdot 10^{-5} \text{ s}^{-1}$. At 0.025 M (B) the slope had increased to $3.65 \cdot 10^{-5} \text{ s}^{-1}$, while suspensions in the range from 0.030 M up to 0.050 M (C) were characterized by a slope of $1.93 \cdot 10^{-4} \text{ s}^{-1}$.

This rate of absorbance drop is proportional to the sedimentation velocity of particles/aggregates (eq. 2.30). This gives a ratio between the radii of the kinetic units $R_A : R_B : R_C$ (neglecting corrections concerning the effective density of aggregates) of 1 : 1.6 : 3.8 .

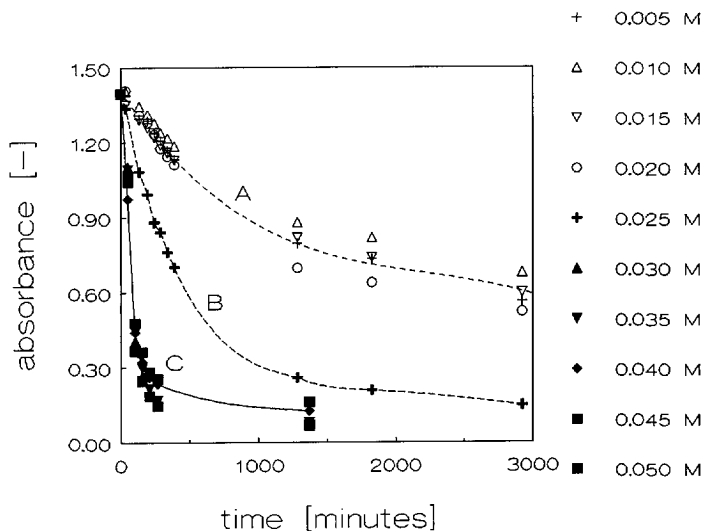


Figure 4.3 The time dependent absorbance of diluted suspensions of A16SG-F at various aluminum nitrate concentrations

Curve A represents the sedimentation of primary particles of the A16SG-F powder in a well deflocculated system. Curves B and C correspond to sedimentation of partly and completely unstable suspensions. The aluminum nitrate concentration at which slow coagulation becomes apparent (due to the thermal motion of the particles) is thus above 0.020 M.

The final absorbance of 0.70, 0.20 and 0.15, were reached in resp. about 2000, 1500 and 1000 minutes. In case of A, the particle diameter corresponding with a sedimenting distance of 2.5 cm in about 2000 minutes would be $2R = 0.31 \mu\text{m}$ (eq. 2.30).

Colloid stability of more concentrated A16SG-F suspensions

While preparing more concentrated A16SG-F suspensions care should be taken concerning the nitrate concentration. Because of the positive adsorption of nitrate ions on the particles, the actual nitrate concentration in the supernatant is lower than expected from

the total amount of water and added aluminum nitrate. Using the stock suspension, suspensions with volume fractions ranging from 0.20 - 0.57 v/v and aluminum nitrate concentrations ranging from 0.020 - 0.100 M have been prepared.

The increased solids content was obtained by centrifugal densification. A necessary amount of supernatant (eq. 4.4) was removed using a pipette to obtain the desired new volume fraction (accuracy ± 0.001 v/v). Suspensions with increased volume fractions were now obtained by redispersing the consolidated particle compact in the remaining supernatant on the roller bench for 24 hrs. For this concentration procedure might result in irreversible aggregation of particles, a particle size distribution (psd) of a redispersed suspension was measured.

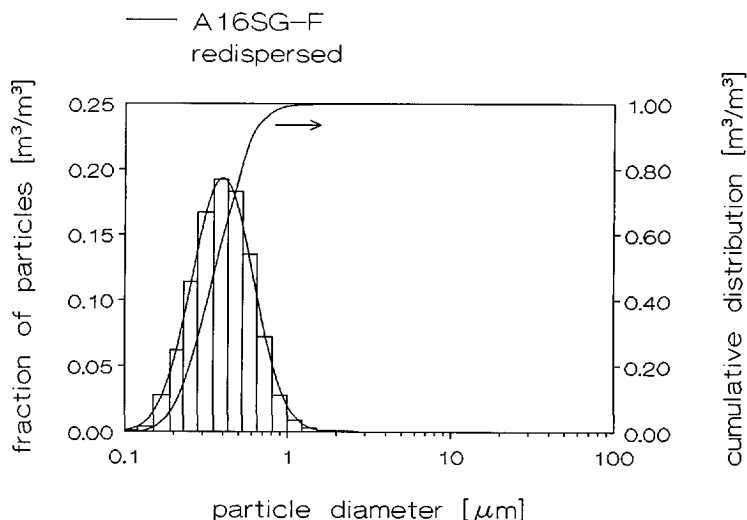


Figure 4.4 The particle size distribution of the A16SG-F powder after the concentration procedure

In figure 4.4 the psd of the redispersed suspension with a volume fraction of 0.278 v/v is shown. Comparing figure 4.4 with figure 4.1, the psd of the stock suspension, shows that the psd is not influenced by the concentration procedure. The calculated characteristic values of the log-normal distribution of the A16SG-F powder in the stock suspension and the redispersed suspension were identical. Irreversible aggregation due to the concentration procedure thus remained absent.

A desired amount of aluminum nitrate was then added under slow stirring. The nitrate concentration of the suspensions has been measured, after an ageing period of two days on the roller bench, in their supernatant, by means of ion chromatography.

The adsorption E [$\text{mol}/\text{m}^2_{\text{A16SG-F}}$] of nitrate (in terms of an equivalent amount of $\text{Al}(\text{NO}_3)_3$) depends on the particle volume fraction (proportional with the total particle surface present in the suspension) and with the actual aluminium nitrate concentration C_{actual} . The empirical adsorption isotherm was

$$E = (6.3 \pm 0.7) \cdot 10^{-7} + (2.3 \pm 1.4) \cdot 10^{-6} \cdot C_{\text{actual}} \quad [\text{mol}/\text{m}^2] \quad (4.5)$$

The conductance of the suspensions with a volume fraction of 0.2 varied between 5.1 mS/cm (0.02 M) and 23.9 mS/cm (0.1 M), and the pH varied between 3.95 (0.02 M) and 3.55 (0.1 M). The measured conductivity agreed with the value expected from the actual aluminum nitrate concentration (table 4.2), but the pH has shifted about 0.4 upwards. Increasing the ageing to a period of two weeks neither influenced the conductivity nor the pH of the suspensions.

The colloid stability of concentrated suspensions may be observed visually by dipping a quartz plate in a suspension. After removing the quartz plate, on drying, stable suspensions will result in a thin transparent smooth layer on the quartz plate. Flocculated suspensions show a thicker and less transparent layer of irregular thickness, comparable to the structure of a dried buttermilk layer on glass.

The results of the dip tests indicated that all suspensions with an actual aluminum nitrate concentration exceeding 0.022 M, independent of volume fraction, appeared to be flocculated. This result is consistent with the adsorbance data obtained on dilute A16SG-F suspensions.

References

- [1] F.F. Lange, J. Am. Ceram. Soc. 72 [1] (1989) 3-15
- [2] A. Roosen, H. K. Bowen, J. Am. Ceram. Soc. 71 [11] (1988) 970-977
- [3] W.H. Gitzen, "Alumina as a ceramic material", The Am. Ceram. Soc. Inc., Columbus Ohio US (1970) 111-115
- [4] H.S. Chung, R. Hogg, Colloids and Surfaces 15 (1985) 119-135
- [5] P.A. Nammensma, W. Seinen, "Diameter bepaling van bolletjes met statische lichtverstrooiing. Experimenten met de Malvern Mastersizer", ECN Memo N° 88-190 (1988)
- [6] J.J.F. Scholten, "Katalyse en Katalysatoren", Dep. of Chem. Techn. TH Delft (1985) 80-120

- [7] R.C. Weast , M. J. Astle (eds) , "Handbook of chemistry and physics, 60th ed." , CRC Press Inc. , Baco Raton Florida US (1980) page d169
- [8] E.J.W. Verwey , J. Th. G. Overbeek , "Theory of the stability of lyophobic colloids", Elseviers Publ. Comp. Inc. (1948)
- [9] B.V. Derjaguin , L.D. Landau , "Theory of the stability of strongly charged lyophobic sols and of adhesion of strongly charged particles in solution of electrolytes" , Acta Physiochim. USSR 14 (1941) 633
- [10] S.B. Hall , J.R. Duffield , D.R. Williams , J. Colloid & Interface Sci. 143 [2] (1991) 411-415
- [11] P.C. Hiemenz , "Principles of Colloid and Surface Chemistry , 2nd ed." , Marcel Dekker Inc. NY (1986)
- [12] J.A. Yopps , D. W. Fürstenau , J. Colloid Sci. 19 (1964) 61-71
- [13] E. Matijević , Ann. Rev. Mater. Sci. 15 (1985) 483-516
- [14] C.H. Schilling , "Microstructure Development by Colloidal Filtration" , thesis Univ. of California Los Angeles (1983)
- [15] B.C. Lippens , Chemisch Weekblad 62 (1966) 336-339
- [16] M.A. Hassen , R.H. Davis , Powder Techn. 58 (1989) 285-289
- [17] D.G. Peters , J.M. Hayes , G.M. Hieftje , "Chemical separations and measurements" , W.B. Saunders Comp. Philadelphia (1974)

4.2 Rheology of concentrated α -alumina suspensions

By analyzing the rheology of our A16SG-F suspensions in terms of the Giant-Floc model (eq. 3.18), the drag parameters q and l^2 will be revealed. For our suspension system we related the colloid stability (in terms of aluminum nitrate concentration) to the interaction parameter l^2 .

Extrapolation of the viscosity of suspensions with identical l^2 to infinite viscosity yields ϕ_{div} , the volume fraction where the particles lock into a rigid random packed structure prohibiting shear. As shown the density of this structure, ϕ_{div} , depends on the interaction parameter l^2 .

Measurement procedures

Rheological measurements were done using a Carri-Med CSL 100 rheometer. This rheo-meter measures the response of shear caused by an imposed stress. The imposed torque T [Nm] could be varied between $1 \mu\text{Nm}$ and $10^4 \mu\text{Nm}$ with a resolution of $0.1 \mu\text{Nm}$. The resulting angular velocity Ω [rad/s], in a range of 0 to 50 rad/s, was measured with an accuracy of 10^{-4} rad/s. The temperature of the rotor-stator system could be varied between 0 and 100°C with a resolution of 0.1°C . The actual temperature, with an

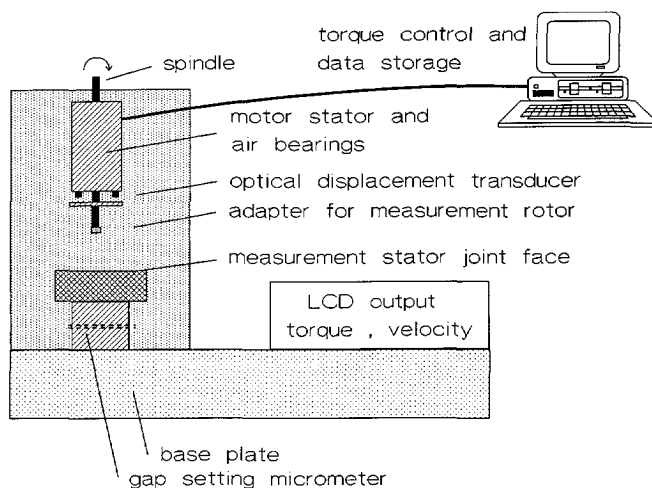


Figure 4.5 A schematic reproduction of the Carri-Med CSL 100 measurement system

accuracy of 0.1 °C , was measured using a Pt100 thermocouple. A schematic reproduction of the measurement system is shown in figure 4.5.

The mean shear stress and shear rate experienced by a fluid for a given rotor-stator system are related to resp. the imposed torque T [Nm] and measured angular velocity Ω [rad/s] by the geometrical constants (App. 2,3) of the measurement system, resp. G_r [m⁻³] and $G_{\dot{\gamma}}$ [-] :

$$\bar{\tau} = G_r \cdot T \quad [Pa] \quad (4.6)$$

$$\bar{\dot{\gamma}} = G_{\dot{\gamma}} \cdot \Omega \quad [s^{-1}] \quad (4.7)$$

Due to the wide range of viscosity of the suspensions, and our intention to measure viscosities in the high shear rate region, two cylindrical rotor-stator combinations have been used. Well chosen geometries have the advantage that shear stress and shear rate are (almost) uniformly distributed over the fluid.

Less viscous suspensions were measured using a double concentric cylinder (DCC), with $G_r = 8.637 \cdot 10^3$ [m⁻³] and $G_{\dot{\gamma}} = 53.14$ [-] (fig. 4.6) .

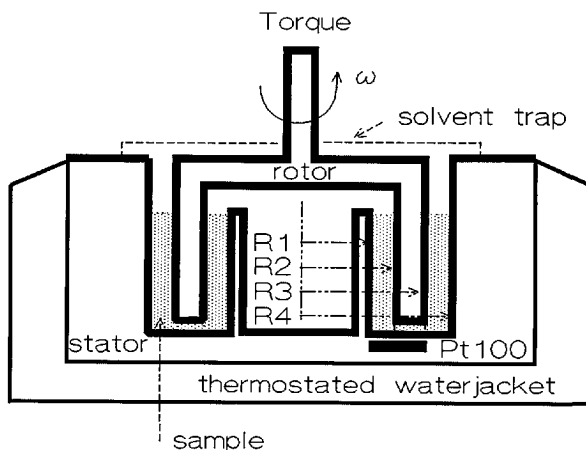


Figure 4.6 The double concentric cylinder

Highly viscous suspensions were measured using a medium concentric cylinder (CC), with $G_r = 24.05 \cdot 10^3$ [m⁻³] and $G_{\dot{\gamma}} = 12.34$ [-] (fig. 4.7).

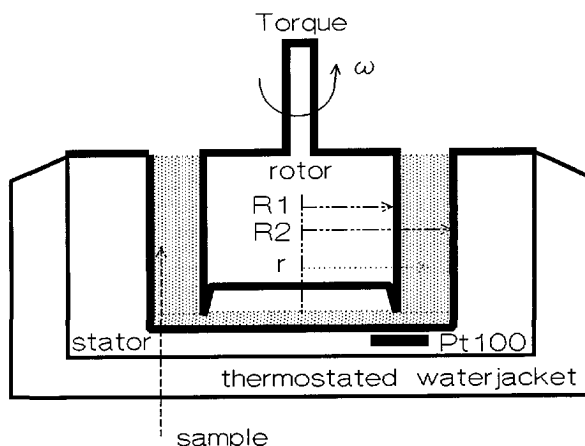


Figure 4.7 The medium concentric cylinder

The suspensions were characterized by measuring steady state flow curves, at 20.0 °C, from zero shear rate to the highest possible shear rate (for a given rotor-stator combination). Before adding a sample of the suspension (using a pipette) the "cup" was thoroughly cleaned, rinsed with demineralized water and dried.

To avoid possible influence of sample injection on shear behaviour, all suspensions were presheared during a time t_{preshear} . The preshear stress τ_{preshear} was chosen such to obtain a shear rate approaching the maximum shear rate permitted by the used rotor-stator combination. During this preshear period the samples obtained the required measurement temperature of 20.0 °C. The preshear procedure is followed by a rest period t_{rest} . Well within the preshear and rest period the temperature of the samples had equilibrated to the desired temperature of 20.0 °C.

A shear stress sweep was then measured. During the rising branch a linear increase of the shear stress in time was imposed, from 0 Pa to a maximum shear stress τ_{max} in a time $t_{1/2\text{sweep}}$. The increasing branch was directly followed by a descending branch in which the shear stress linearly decreased from τ_{max} to 0 Pa, again in time $t_{1/2\text{sweep}}$. During each half sweep 200 T, Ω data points were measured, taken with linear intervals of shear stress. The maximum shear stress τ_{max} was chosen such that the maximum shear rate permitted by the used rotor-stator combination was approached.

The measured flow curves were assumed to be steady state flow curves when visual no

distinction between rising and descending branch of the flow curve could be made. Preliminary experiments showed the occurrence of hysteresis and instabilities in the flow curves, especially in case of suspensions with a high solids volume fraction and a high aluminum nitrate concentration.

For all suspensions the parameters of the flow program were optimized to satisfy, or, when not possible, to approach the above steady state flow curve criterion.

All experiments were at least duplicated. Details of the flow program, optimized for each suspension, are shown in table 4.3.

Table 4.3 Parameters of the flow program for the various suspensions

susp. code	meas. system	τ_{preshear} [Pa]	t_{preshear} [min]	t_{rest} [min]	τ_{max} [Pa]	$t_{1/2\text{sweep}}$ [min]
0.20-A	DCC	6	1	2	6	15
0.20-B	DCC	8	1	2	8	15
0.20-C	DCC	10	1	2	10	15
0.20-D	DCC	19	1	2	19	15 *
0.28-A	DCC	10	1	2	10	20
0.28-B	DCC	12	1	2	12	20
0.28-C	DCC	18	1	2	18	30
0.28-D	DCC	36	1	2	36	20 *
0.40-A	DCC	25	1	2	25	20
0.40-B	DCC	35	1	2	35	20
0.40-C	DCC	53	1	2	53	30
0.40-D	CC	80	1	2	80	20 *
0.50-A	DCC	86	1	2	86	20
0.50-B	CC	50	5	2	50	20
0.50-C	CC	85	5	1	85	15
0.50-D	CC	240	5	1	240	15 *
0.57-A	CC	240	4	1	240	20
0.57-B	CC	180	1	1	160 +	15 *
0.57-C	CC	240	1	1	160 +	15 *

* hysteresis

+ to avoid instability at high shear rates $\tau_{\text{max}} < \tau_{\text{preshear}}$

Preparation of suspensions

Using the stable A16SG-F stock suspension (4.5 l, 0.199 v/v), two days after the stock preparation a matrix of suspensions was prepared with five different volume fractions, ranging from 0.2 v/v to 0.57 v/v, and four different salt concentrations, ranging from 0.2 to 0.1 M.

Of each suspension about 100 ml was obtained. After a period of two days on the roller bench all suspensions were characterized (table 4.4).

Table 4.4 Prepared suspensions and measured properties

code	ϕ_v (± 0.001) [-]	total added salt (± 0.02) [mg/g]	C_{aluminum} nitrate (± 0.0004) [M]	pH (± 0.05)	σ (± 0.02) [mS/cm]
0.20-A	0.199	11.36	0.0209	3.95	5.04
0.20-B	0.199	17.05	0.0359	3.74	9.05
0.20-C	0.199	24.82	0.0548	3.64	13.50
0.20-D	0.199	44.32	0.1034	3.46	23.90
0.28-A	0.278	11.36	0.0209	3.84	5.28
0.28-B	0.278	15.73	0.0350	3.77	8.56
0.28-C	0.278	20.22	0.0550	3.69	12.92
0.28-D	0.278	32.86	0.1041	3.55	22.50
0.40-A	0.403	11.36	0.0209	3.95	5.16
0.40-B	0.403	13.80	0.0373	3.82	8.81
0.40-C	0.403	16.46	0.0555	3.72	12.68
0.40-D	0.403	23.97	0.1041	3.60	22.60
0.50-A	0.501	11.36	0.0209	3.94	5.12
0.50-B	0.501	12.86	0.0350	3.83	8.35
0.50-C	0.501	14.93	0.0557	3.73	12.76
0.50-D	0.501	20.08	0.1070	3.55	23.20
0.57-A	0.570	11.36	0.0209	---	5.05
0.57-B	0.570	12.52	0.0343	---	---
0.57-C	0.570	14.11	0.0557	---	---

* insufficient amount of supernatant

The average aluminum nitrate concentrations of suspensions in the four groups A to D are :

A :	0.0209 ± 0.0004	M
B :	0.036 ± 0.002	M
C :	0.055 ± 0.001	M
D :	0.105 ± 0.002	M

As had been expected from the investigation of the stability of this suspension system (section 4.1) , all suspensions of group A were well deflocculated (dip test). Suspensions in group B to D were more or less flocculated, increasingly at higher salt concentrations and/or higher volume fractions. The most strongly flocculated suspension, 0.57-D , could not be poured out of the PE bottle. This suspension has not been used for the rheological investigation.

To minimize aging effects, all rheological experiments were done within 1 week after the characterization of the suspensions.

Determination of $\eta_{r,\infty}$

A double logarithmic representation of the flow curves has been used to investigate the shear thinning of the suspensions and to determine the relative viscosity in the high shear limit (figures 4.8-12). Without loss of essential information the number of data points per flow curve has been reduced with a factor 4 to 100 equidistant points.

Increasing aluminumnitrate concentrations and/or increasing the volume fraction of solids, gives higher apparent viscosities and increased shear thinning behaviour. As discussed in section 3.2 the increase in apparent viscosity can be explained in terms of increasing drag parameters. l^2 increases from A \rightarrow D, and q increases from $\phi_v = 0.20$ to 0.57 .

In stable suspensions (A) shear thinning is due to particle ordering at increased shear rate (eq. 3.6). The shear thinning is centred around a shear rate of 27 s^{-1} , where the transition between order and disorder is expected (eq. 3.2).

In case of the flocculated suspensions (B-D), shear thinning extends to higher shear rates. Here shear thinning results from particle ordering caused by network break-up at increased shear rates (eq. 3.12).

The suspensions series D, as well as 0.57-B and C, showed some hysteresis (this effect is more clearly expressed in the linear presentation of the flow curves, appendix 4). In all cases the descending branch of the flow curve was lower than the rising branch. Our intention was not to investigate, but rather to reduce the hysteresis. It troubled the extrapolation of the viscosity to infinite shear.

Hysteresis may origin from sedimentation, reversible and irreversible alignment of the shear planes (ordering) at high shear rates, and/or centrifugal effects. Centrifugal effects and sedimentation have not complicated the flow measurements on series A-C of less

concentrated suspensions. Because the more concentrated suspensions have a higher viscosity, sedimentation and centrifugal effects are negligible. Irreversible alignment of shear planes should already occur during the preshear of the samples, and is thus not expected to affect the flow curves. Changes in preshear time t_{preshear} and sweep time $t_{1/2\text{sweep}}$ did not influence the hysteresis effect. The nature of the observed hysteresis is still unknown. Hysteresis thus could not be avoided. As can be seen in figure 4.12, in case of suspensions 0.57-B and 0.57-C, hysteresis strongly troubled the viscosity measurements. The intersecting flow curves indicate the occurrence of apparent wall slip (appendix 3) [1-3].

In figures 4.8-12 the measured flow curves are shown. The results of fitting the Sisko relation (eq. 3.3) to the measured flow curves are represented by the solid lines. The Sisko relation describes the shear thinning of stable and flocculated concentrated A16SG-F suspensions from $\dot{\gamma} = 0.01$ up to $\dot{\gamma} = 2000$. This justifies the extrapolation to infinite shear, which is implied in the definition of $\eta_{r,\infty}$. For each flow curve, the fitted parameters are listed in table 4.5, as well as the estimated total error in $\eta_{r,\infty}$ (from calibration, occurrence of hysteresis and apparent wall slip).

Increasing C implies more shear thinning at a given shear rate. A decrease in n implies that shear thinning is seen over a wider range of shear rates.

In a floc, particle motion is hindered by the dragging of neighbouring particles. Particle drag is determined by the drag parameters q and l^2 .

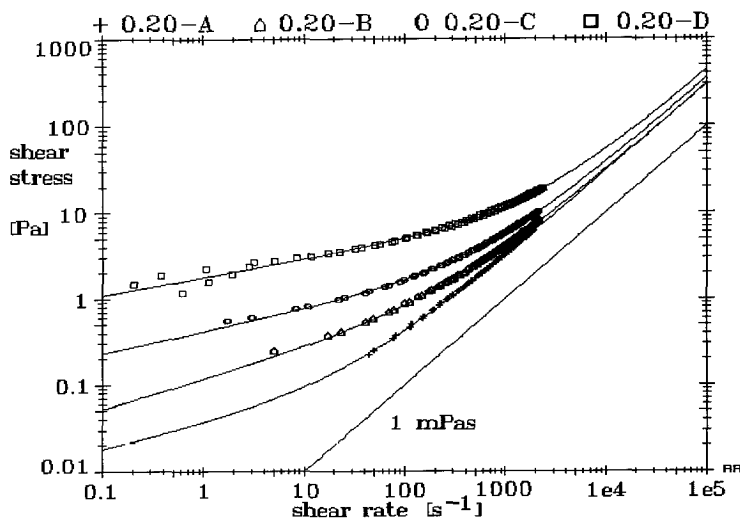


Figure 4.8 Flow curves of the suspensions with solids volume fraction $\phi_v = 0.20$

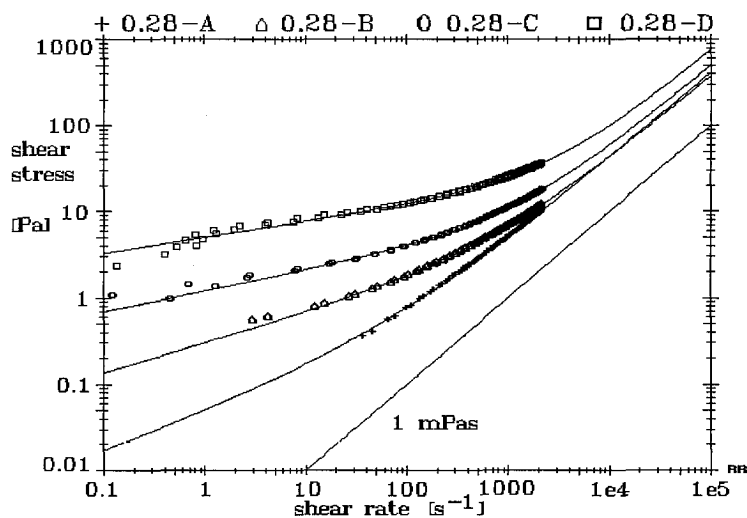


Figure 4.9 Flow curves of the suspensions with solids volume fraction $\phi_v = 0.28$

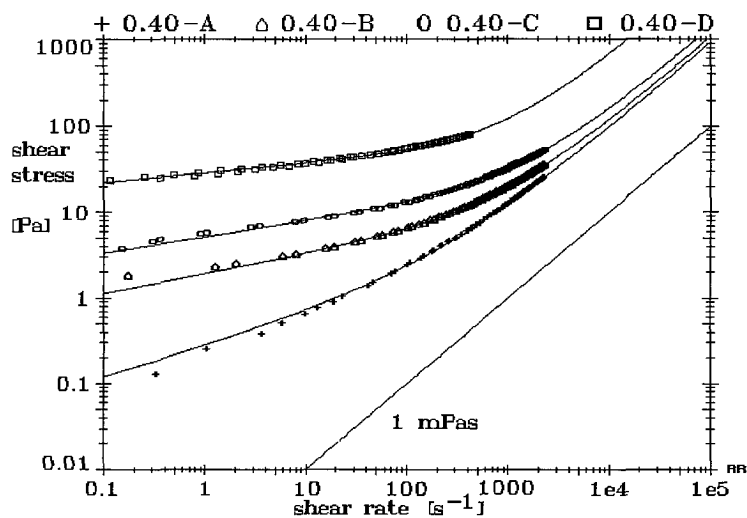


Figure 4.10 Flow curves of the suspensions with solids volume fraction $\phi_v = 0.40$

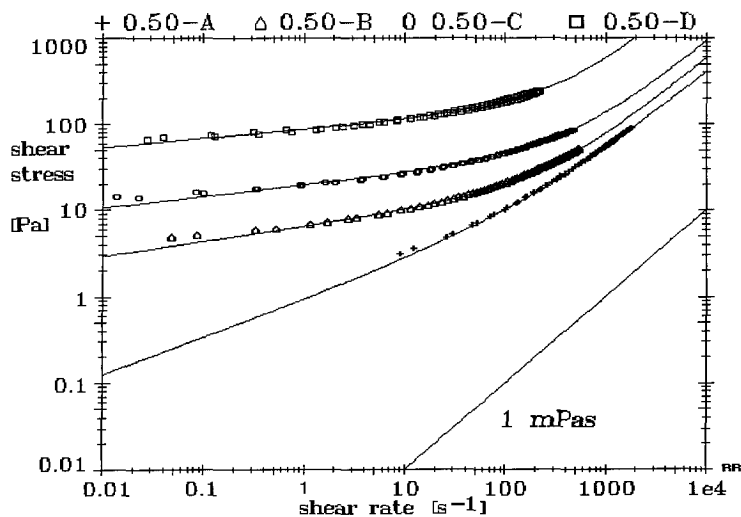


Figure 4.11 Flow curves of the suspensions with solids volume fraction $\phi_v = 0.50$

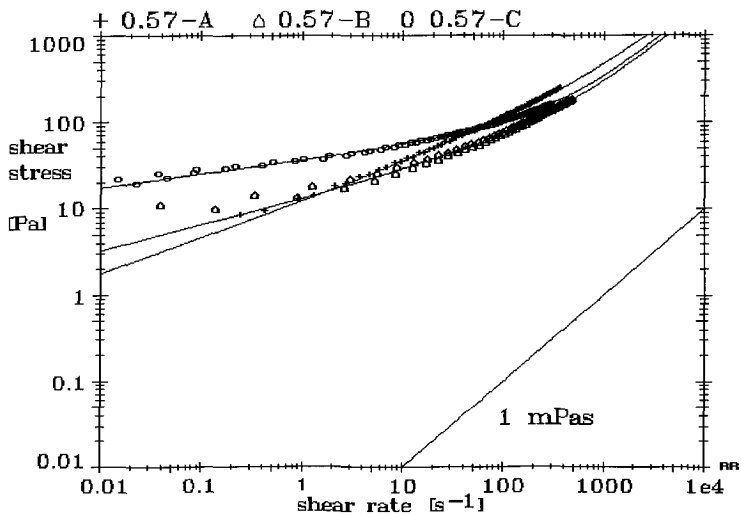


Figure 4.12 Flow curves of the suspensions with solids volume fraction $\phi_v = 0.57$

When the strength of the particle attraction increases, due to increased aluminum nitrate concentrations, this results in higher values of the interaction parameter l^2 . A higher particle volume fraction increases the number of nearby particles, i.e. the mean coordination number q of the particles in the floc.

Thus increases in the aluminum nitrate concentration or particle volume fraction increase the drag effect, resulting in higher values of $\eta_{r,\infty}$ (eq. 3.18). These are accompanied by the expected increases in C and decreases in n .

Table 4.5 Fitting the Sisko relation (eq. 3.3) to the measured flow curves

susp. code	$\eta_{r,\infty}$ [-]	C [Pa s ⁿ]	n [-]	estimated total error in $\eta_{r,\infty}$ [%]
0.20-A	3.00 ± 0.05	0.034 ± 0.005	0.28 ± 0.03	4
0.20-B	2.92 ± 0.05	0.114 ± 0.003	0.340 ± 0.006	4
0.20-C	3.45 ± 0.04	0.41 ± 0.01	0.252 ± 0.006	4
0.20-D ⁺	4.2 ± 0.1	1.76 ± 0.08	0.210 ± 0.009	4
0.28-A	4.06 ± 0.07	0.047 ± 0.003	0.45 ± 0.01	3.7
0.28-B	3.64 ± 0.09	0.300 ± 0.009	0.343 ± 0.006	3
0.28-C	4.85 ± 0.07	1.2 ± 0.3	0.238 ± 0.005	3
0.28-D ⁺	7.2 ± 0.2	5.0 ± 0.1	0.185 ± 0.005	3
0.40-A	9.05 ± 0.08	0.276 ± 0.001	0.367 ± 0.008	3.5
0.40-B	10.4 ± 0.1	1.91 ± 0.08	0.229 ± 0.008	3
0.40-C	13.3 ± 0.3	5.12 ± 0.17	0.188 ± 0.007	3
0.40-D ⁺	61 ± 3	28.5 ± 0.3	0.111 ± 0.004	3
0.50-A	36.3 ± 0.8	0.91 ± 0.09	0.43 ± 0.02	3.5
0.50-B	56.0 ± 0.7	6.5 ± 0.1	0.176 ± 0.005	2
0.50-C	86 ± 2	19.8 ± 0.3	0.135 ± 0.005	2
0.50-D ⁺	412 ± 30	87 ± 2	0.106 ± 0.008	10
0.57-A*	243 ± 7	12.4 ± 0.2	0.424 ± 0.005	15
0.57-B [□]	194 ± 10	13.3 ± 0.7	0.31 ± 0.02	~200
0.57-C [□]	232 ± 5	36.8 ± 0.4	0.164 ± 0.003	~500

⁺ hysteresis

* apparent wall slip (appendix 3)

[□] hysteresis and apparent wall slip

Interpretation of the viscosity data according to the Giant-Floc model

Particles in stable suspensions, series A, interact as hard spheres. In this case the interaction parameter $l^2 = l_s^2$, and $\eta_{r,\infty}$ becomes determined in full by the "Krieger-Dougherty part" of the adapted Giant-Floc model (eq. 3.18). Assuming that the effect of the electrical double layer thickness (eq. 4.1) on the effective volume fraction ϕ_v is negligible, the $\eta_{r,\infty}$ of series A can be fitted to eq. 3.18. This gives values for the intrinsic powder qualities $\phi_{\max,\infty}$ and $|\eta|$.

In more or less flocculated suspensions, series B-D, $\eta_{r,\infty}$ is influenced by the value of the interaction parameter l^2 . Since the intrinsic powder qualities are already known from series A, for series B to D the value of l_s^2 and the interaction parameter l^2 can be obtained by curve fitting.

The logarithmic form of eq. 3.18 has been used to fit the data. The total estimated error in $\eta_{r,\infty}$, due to factors like measuring near the limits of the measurement range, hysteresis and/or apparent wall slip etc., has been introduced to obtain the appropriate weight factors for the data pairs. The results of this procedures are shown in table 4.6.

Table 4.6 Fitting eq. 3.18 to the $\eta_{r,\infty}$ values (Table 4.5) of suspension series A to D

susp. series	$ \eta $ [-]	$\phi_{\max,\infty}$ [-]	l_s^2 [-]	l^2 [-]
A (0.0209 M)	3.62 ± 0.25	0.63 ± 0.01		
B (0.036 M)	3.62	0.63	0.32 ± 0.04	0.35 ± 0.02 $0.33 \pm 0.02^*$
C (0.055 M)	3.62	0.63	0.28 ± 0.07	0.36 ± 0.04
D (0.105 M)	3.62	0.63	0.15 ± 0.11	0.42 ± 0.02 $0.45 \pm 0.03^*$

* assuming $l_s^2 = 0.28$

Because the alumina particles are not spherical, the intrinsic viscosity $|\eta|$ exceeds the theoretical value of 2.5. The value $|\eta| = 3.62$ is consistent with prolate particles with an axial ratio of about 2.6 [4].

The calculated value of $\phi_{\max,\infty}$, 0.63 ± 0.01 , agrees with the value of 0.63 ± 0.01 found by Sohn and Moreland in case of a random dense packing of sand particles with $\sigma=0.46$ and an axial ratio of 1.2 [5].

Some spread was found in the experimental values of l_s^2 . However, even the assumption

of a constant value, $l_s^2 = 0.28$, did not strongly affect the values for l^2 . As discussed in section 3.2, $\phi_{div.}$, the particle volume fraction at which particle drag results in the blocking of particles, depends on the strength of the particle interactions (l^2). In case of weak particle attraction, when $l^2 < 1/3$, $\phi_{div.}$ equals ϕ_{max} (eq. 3.18). ϕ_{max} is the density of the random dense packing of powder particles, an intrinsic powder quality. In case of strong particle attraction, when l^2 exceeds $1/3$, blocking of the particles occurs at a lower particle volume fraction, $\phi_{max}/(3l^2)$. For our suspensions the interaction parameter l^2 reaches the critical value of $1/3$ at an aluminum nitrate concentration close to 0.036 M. In figure 4.13 the fitted curves (table 4.6), according to the adapted Giant-Floc model (eq. 3.18), are shown. It clearly shows the influence of l^2 on $\phi_{div.}$.

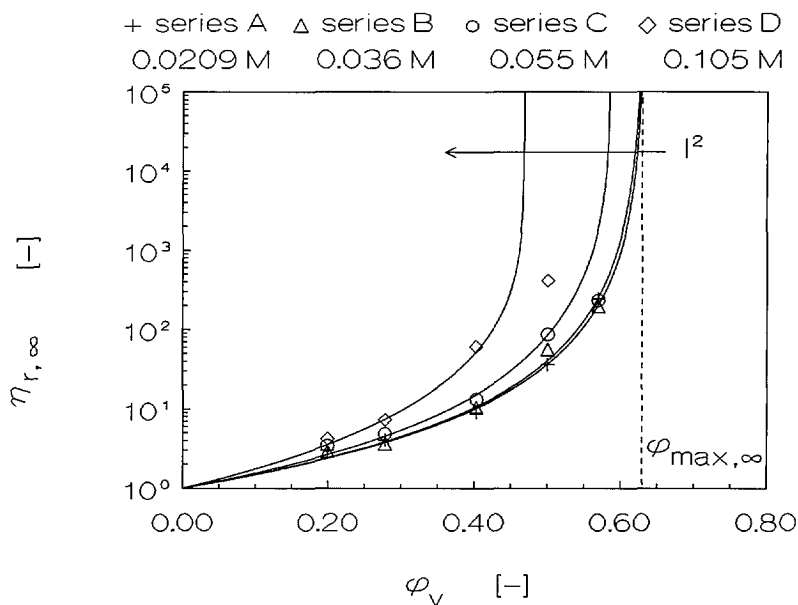


Figure 4.13 Fitted curves according to the Giant-Floc model (eq. 3.18),
 $l_s^2 = 0.28$

We analyzed the viscosity of our A16SG-F suspensions in terms of the adapted Giant-Floc model. This model relates particle drag, determined by the mean coordination number q and the interaction parameter l^2 , to the shear thinning of concentrated more or less flocculated suspensions (sect. 3.2). As shown, variations in the drag parameters q (ϕ_v) and l^2 indeed account for the experimentally observed differences in shear thinning of our

A16SG-F suspensions. The interaction parameter I^2 , as a measure of the net strength of attraction between particles in the floc, has been related to the aluminum nitrate concentration in our suspensions.

In ideal compaction, e.g. pressure filtration or slip casting, the velocity of particles in the suspension equals the velocity of the surrounding fluid (sect. 2.1). In the absence of relative fluid flow, a random and open stacked consolidation zone is formed. In the consolidation zone, fluid flows around the particles. High shear rates are involved. The resulting shear stresses on the particles are on average directed towards the filter. The shear stress tends to force the particles into a more dense packing.

Particle drag, however, reduces the mobility of particles in the consolidation zone. This opposes further densification. From analyzing the rheology of our suspensions we found that in case of a weak net particle attraction ($I^2 < 1/3$), related to aluminum nitrate concentrations below 0.036 M, blocking of particles in a shear field occurs at

$\phi_{\max, \infty} = 0.63 \pm 0.01$. $\phi_{\max, \infty}$ is the density of the random dense packed powder. It is an intrinsic powder quality. In case of strong net particle attraction ($I^2 > 1/3$), which relates to aluminum nitrate concentrations above 0.036 M, particles are blocked at a lower volume fraction. Blocking then occurs at $\phi_{\text{div.}} = \phi_{\max, \infty} / (3I^2)$. When particles are blocked, shear cannot further densify a particle packing.

In case of non-ideal compaction (centrifugation) the sedimenting particles experience a counter flow of fluid. This results in the formation of an ordered but open stacked consolidation zone. During further densification, due to the centrifugal force, fluid has to leave the particle packing. Fluid flow thus tends to preserve the initial ordered structure and opposes further densification of the consolidation zone. Compared with ideal compaction, in case of centrifugation less dense particle packings are expected.

Based on the results of the rheological investigation, for compacted A16SG-F suspensions we thus predict the following wet densities :

ideal compaction (slip casting, pressure filtration) :

$$\begin{aligned} I^2 < 1/3 \quad (C < 0.036 \text{ M}) & : \quad \phi_{v, \text{wet}} = \phi_{\max, \infty} = 0.63 \pm 0.01 \\ I^2 > 1/3 \quad (C > 0.036 \text{ M}) & : \quad \phi_{v, \text{wet}} = \phi_{\text{div.}} < \phi_{\max, \infty} \end{aligned}$$

non ideal compaction (centrifugation) :

$$\text{for all } I^2 : \quad \phi_{v, \text{wet}} < \phi_{\max, \infty}$$

with $\phi_{\max, \infty}$ the density of the random dense packed A16SG-F powder.

By means of densification experiments with our A16SG-F suspensions we will test some of the above predictions.

References

- [1] R. Rautenbach , D. Schegel , *Chemie-Ing.-Techn.* 41 (1969) 369-374
- [2] A.P. Shapiro , R.F. Propstein , *Phys. Rev. Letters* 68 [9] (1992) 1422-1425
- [3] F.W.A.M. Schreuder , H.N. Stein , *Rheol. Acta* 26 (1987) 45-54
- [4] P.C. Hiemenz , "Principles of colloid and surface chemistry" , Marcel Dekker Inc., N.Y. (1986) 198-204
- [5] H.Y. Sohn , C. Moreland , *Can. J. Chem. Eng.* 46 (1968) 162-165

Chapter 5

Compaction of concentrated α -alumina suspensions, drying and sintering

5.1 Introduction

Rheological investigation of our A16SG-F suspensions indicated a strong influence of the colloid stability on the shear thinning behaviour. By means of the Giant-Floc model (sect. 3.2) the shear thinning of our suspensions has been analyzed. It has been shown that the shear thinning depends on particle drag. Particle drag is determined by the mean coordination number q (ϕ_v) of the particles, and the interaction parameter l^2 , as a measure of the net attraction between the particles in a floc. Because these parameters determine the mobility of the particles, they influence wet compact formation (sects. 2.1, 4.2).

In case of ideal compaction, because the values of the drag parameters in our suspensions are known from the rheological investigation, we are able to predict the density of resulting wet compacts. Weakly flocculated A16SG-F suspensions ($l^2 < 1/3$), i.e. suspensions with an aluminum nitrate concentration below 0.035 M, are expected to densify to $\phi_{\max, \infty} = 0.63 \pm 0.01$. Strongly flocculated suspensions, with aluminum nitrate concentrations exceeding 0.035 M, should densify to $\phi_{\text{div.}} = \phi_{\max, \infty} / (3l^2)$. To verify this predictions, a stable and a strong flocculated suspension were pressure filtrated. Slip casting and pressure filtration are expected to result in identical wet compacts. Slip casting of stable suspensions then serves as a control experiment.

In case of counterflow less dense particle packings should result. Stable suspensions have been centrifugated at various Pé numbers. Through comparing parameters of the wet compacts formed by centrifugation and pressure filtration (slip casting), the effect of fluid flow has been examined.

5.2 Experimental

For our experiments we have chosen a stable suspension, 0.20-A with $I^2 = I_s^2 = 0.28$, and a strongly flocculated suspension, 0.20-C with $I^2 = 0.36$ (Table 4.6). The details of preparation and suspension properties are listed in Chapter 4. To minimize aging effects, all densification experiments were done within one week after characterization of the suspensions. For sake of reproducibility, each compaction experiment was replicated at least four times.

By analyzing the compact formation, properties of the wet compact, like porosity and permeability, can be found. Wet compacts have a limited strength. Sample taking might influence the wet compact structure, this restricts further characterization of the wet compacts.

A ceramic body is obtained after drying a wet compact and sintering of the dried green product. Drying and sintering procedures transform the initial wet microstructure into resp. the green and the ceramic microstructure. The drying and sintering procedures influence the quality of the ceramic microstructure. However, the optimum quality of a ceramic product is bounded by the properties of the original wet compact [1-3].

To investigate how properties of the wet compacts relate to the properties of the dried and resp. sintered structures, we "developed" the wet microstructures using standard drying and sintering conditions. After a light pre-sintering of the dried compacts to make them more rigid (in such a way that measurable shrinkage is avoided) porosity could be measured with mercury intrusion. Variations in the shrinkage behaviour during sintering, due to microstructural differences, were investigated with dilatometry. The sintering has been related to the development of ceramic microstructure by investigating the microstructure of compacts with scanning electron microscopy (SEM).

Wet compaction

Filtration at a constant rate

Filtration experiments were done with a stable and a flocculated suspension, resp. 0.20-A ($I^2 = 0.28$) and 0.20-C ($I^2 = 0.36$). In fig. 5.1 a schematic reproduction of the filtration equipment is shown.

The filtration cylinder had a diameter of 50.0 mm. A porous alumina disc (from cold isostatic pressed and then sintered CS400 MSI), with a thickness of 8.50 mm, has been used as filter. It had a porosity of 0.371 ± 0.003 (through the weight increase due to water saturation), an average pore diameter of $0.113 \pm 0.005 \mu\text{m}$ (Hg intrusion) and a permeability of $K_f = (8.3 \pm 0.3) 10^{-17} \text{ m}^2$.

Filtration was done at room temperature, with a filtration rate of 0.25 mm/min ($\pm 0.1\%$). Compacts were thus formed at a Pé number of about 0.8 (eq. 2.1). The filtration

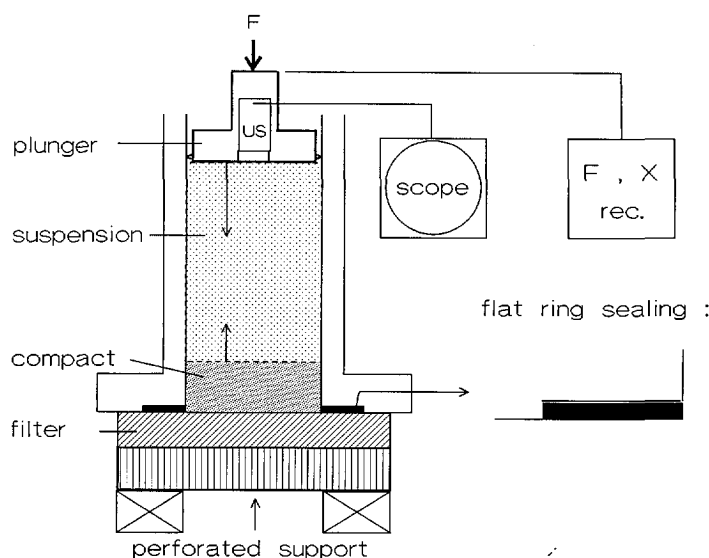


Figure 5.1 The filtration equipment

chamber was filled with a suspension layer of about 20 mm (H_0). The temperature of the suspensions was measured to correct for the influence of temperature on water viscosity. Then the filtration system was closed by placing the filter. Prior to mounting, to prevent filter suction, the filter had been saturated with water. Using an Instron 4502 pressing-bench, the filtration system could exert a maximum pressure of 50 bar. Filtration proceeded until all suspension was converted to compact. The wet compacts, with an approximate height of 6 mm, were then removed to dry.

During filtration, the pressure build up (accuracy 0.02 %) was measured. Compliance of the filtration system strongly influenced the pressure build-up (fig. 5.2). Up to a pressure of 10 bar, the compliance was mainly caused by the setting of the neoprene plunger sealing. Through the compliance at direct contact, the influence of filtration pressure on the actual plunger position is known (distance calibration). The compliance of the filled system relates the plunger position to the filtration chamber volume (volumetric calibration). The distance calibration is used to determine the compact height, while the volumetric calibration is necessary to determine the compact porosity.

Through the pressure build up (above 10 bar), the product of the permeability K_c and the constant of consolidation C has been determined (eq. 2.11). The value of C depends on the compact porosity (eq. 2.3). When the compact porosity is known, C can be determined, and thus the permeability K_c .

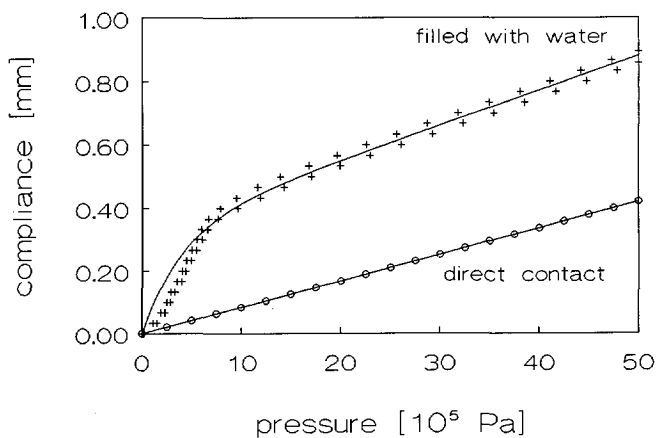


Figure 5.2 The compliance of the filtration system

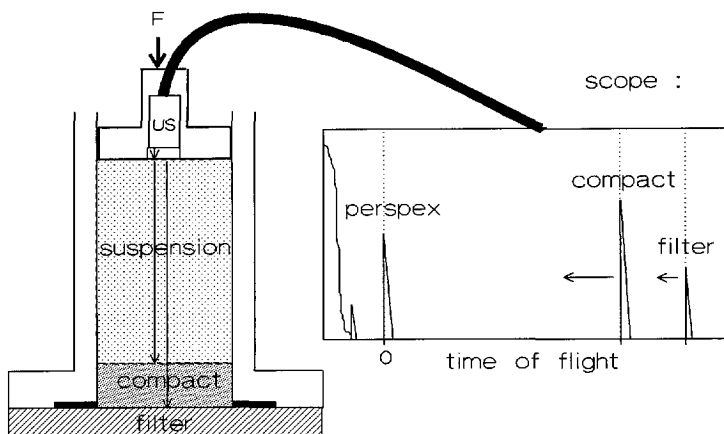


Figure 5.3 Ultrasonic measurement of the compact thickness

The compact thickness $H_c(t)$ was determined through ultrasonic measurement of the height $H_s(t)$ of the suspension layer (fig. 5.3). At the interface of layers with a different density ultrasonic waves reflect. Through calibration, the velocity of the wave propagation through the suspensions is known. Time of flight measurements then indicate the thickness of the suspension layer [4,5]. An Epoch 2001 oscilloscope, in combination with a transmitter/receiver crystal (10 MHz, H2K Krautkrämer), has been used. The suspension layer thickness could be measured with an accuracy of 0.02 mm. The thickness of the compact layer then follows from :

$$H_c(t) = H_0 - v_p t - H_s(t) \quad [m] \quad (5.1)$$

Through eqs. 2.2 and 2.3 , the compact thickness is related to the compact porosity. Thus the porosity and permeability of the compacts were known.

Slip casting

The stable suspension, 0.20-A, was slip cast. The used slip casting equipment is shown in figure 5.4 . The filtration cylinder had a diameter of 35.0 mm. The moulds of

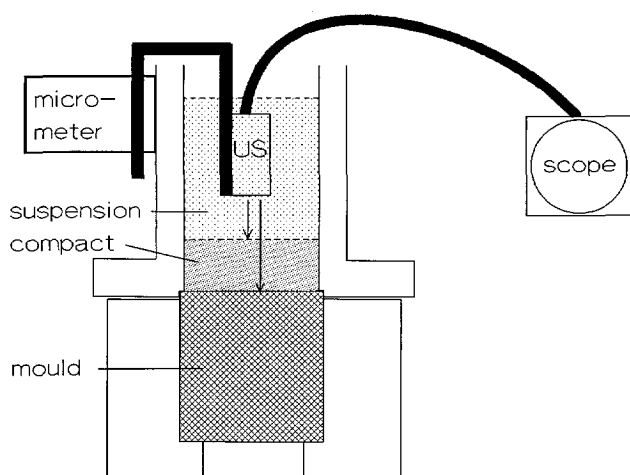


Figure 5.4 The slip casting equipment

porous alumina, made from the same material as the filters which have been used for pressure filtration, had a height of 40.0 mm and a diameter of 40.0 mm. The suction

pressure of the moulds relates to the rate of water suction :

$$\Delta H_{\text{water}} = \sqrt{\frac{K_m \epsilon_m}{\eta_0} 2 \Delta P t} \quad [m] \quad (5.2)$$

with H_{water} the height of the water head, and K_m [m^2] and ϵ_m [-] the permeability and porosity of the mould. The rate of water suction has been determined at the end of absorbing a 10 mm high water column. The moulds exerted a suction pressure of 16.2 ± 0.5 bar.

Slip casting was done at room temperature. The temperature of the suspensions were measured. The system was filled with a suspension column of about 26 mm. During slip casting, the compact growth has been measured by time of flight measurements of the ultrasound waves. The transmitter/receiver crystal was placed at a height of 10.0 mm above the mould. At a compact height of about 5 mm, long before the mould became saturated, the remaining suspension above the compact was removed. The mould and compact then were removed to dry.

The dry mould has been weighed before slip casting. Immediately after removing the redundant suspension, the wet compact with the wetted mould was weighed. The weight of the compact and water sucked by the mould, ΔM [g], equals the weight of converted suspension. The porosity of the compact thus relates to the thickness of the compact through :

$$\epsilon_c = 1 - \frac{\Delta M}{\pi R^2 H_c} \frac{1}{\rho_{\text{susp}}} \phi_v \quad [-] \quad (5.3)$$

$$\wedge \quad \rho_{\text{susp}} = \phi_v \rho_{\text{alumina}} + (1 - \phi_v) \rho_{\text{water}} \quad [g/cm^3]$$

with R [m] the radius of the filtration system.

With a known compact porosity, the permeability K_c could be determined from the measured rate of compact growth (eqs. 2.3 and 2.16).

Centrifugation

Centrifugation of the stable suspension, 0.20-A, has been done at four Pé numbers. The suspensions were contained by closed polycarbonate tubes with a flat bottom, fig. 5.5. These tubes had an inner diameter of 25.7 mm.

Centrifugation was done at a temperature of 20.0 °C. The tubes were filled with a suspension layer of about 70 mm. The conditions of centrifugation are shown in table 5.1. In a centrifuge, acceleration is not uniform but depends on location. The resulting slight variations in consolidation conditions, from bottom to the top of the compact, are shown between parenthesis.

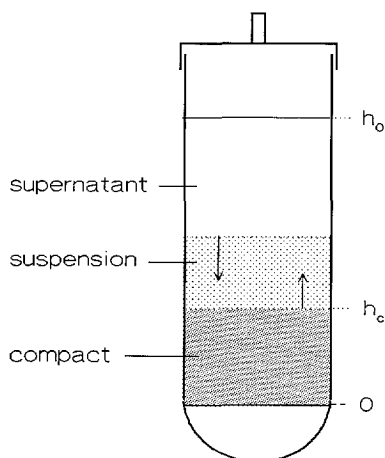


Figure 5.5 The centrifuge tubes

Table 5.1 Conditions of centrifugation at different Pé numbers

acceleration g [9.81 m/s ²]		v_s [mm/min] (eq. 2.27)		Pé [-] (eq. 2.1)		centrifugation time [Hr]
10327	(11339-9315)	53.7	(58.7-48.3)	164	(180-148)	1
1030	(1133-926)	5.3	(5.9-4.8)	16.4	(18.0-14.7)	3
103	(113-93)	0.5	(0.6-0.5)	1.6	(1.8-1.5)	26
20.9	(23.0-18.9)	0.11	(0.12-0.10)	0.3	(0.4-0.2)	54

After centrifuging the clear supernatant was removed. The wet compacts had a thickness of approximately 22 mm. The compacts remained in the tubes and were stored to dry.

Before centrifuging the filled suspension was weighed M_0 [g]. After removing the supernatant the weight of the wet compact was determined. Thus the weight of removed supernatant ΔM [g] was known. The porosity of the compacts could then be determined :

$$\varepsilon_c = 1 - \phi_v \frac{\frac{M_0}{\rho_{susp.}}}{\frac{M_0}{\rho_{susp.}} - \Delta M} \quad [-] \quad (5.4)$$

Drying of the wet particle compacts

The loss of liquid during the drying of a particle compact induces capillary forces, causing the compact to shrink. This finally results in a more densely packed structure. Shrinkage, however, is frequently inhomogeneous as a result of a non uniform pore size distribution. This causes differential stresses (eq. 5.5) in the compact which result in cracking of the compact on drying. To prevent cracking, the drying procedure should be optimized, resulting in industrial drying procedures for various kinds of porous compacts. An introduction of the drying process in porous materials is given by Shaw [6].

In our investigation we focused at the influence of compaction parameters on the wet compact structure. We thus have not optimized the drying and sintering conditions, but rather chose standard conditions. This enables us to examine how variations in wet compact structure affect the development of ceramic microstructure.

Our compacts were dried for 72 hrs under atmospheric pressure, at a temperature of 21 °C and a relative humidity (RH) of 40% . A typical drying curve of a porous compact under these conditions is shown in figure 5.6.

The drying curve may be divided into three stages. In the first stage fast drying proceeds at a constant rate, in the second stage the drying rate slows down. This results in a concave bending of the drying curve. In the last stage the drying rate is extremely slow. Although the second and third drying stages are caused by separate drying mechanisms, the transition is difficult to observe in the drying curve. With our compacts this transition took place somewhere between 32 and 48 hours.

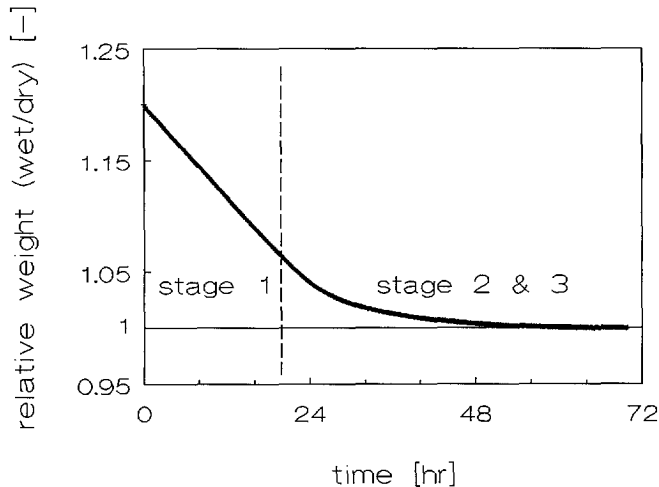


Figure 5.6 Drying curve of a wet A16SG-F compact at 1 Bar, 21 °C, RH = 40 %

The mechanisms which govern the three stages are as follows :

During the first stage, the drying rate is determined by the rate of evaporation of free water on the surface of the compact. The evaporation rate is governed by the mass transfer of water from the surface pores to the surrounding air. In the surface pores, due to loss of water, concave menisci are formed. This results in capillary suction, which causes water transport from the inside of the particle compact to the surface. Assuming cylindrical surface pores, the capillary suction ΔP [Pa] is given by

$$\Delta P = \frac{2 \gamma_w}{r} = - \frac{2 \gamma_w \cos \phi}{R} \quad [Pa] \quad (5.5)$$

with γ_w [N/m] the surface tension of water, r [m] the radius of curvature of the water meniscus, ϕ the contact angle and R [m] the radius of the surface pores. Due to the loss of water, the average interparticle distances inside the compact diminish and the coordination number of the particles increases. During the first drying stage the particle compact strongly shrinks.

The second drying stage starts when particle movement is hindered by an increasing mean coordination number. Shrinkage thus is suppressed, and the rate of water transport from the inner part of the compact to the surface will strongly decrease. The increasing capillary suction in the fraction of small surface pores drains the water from the coarse fraction of

surface pores. Eventually all pores will be filled with air, starting from coarse to fine and from the surface to the centre of the compact. The decreasing number of filled surface pores and the decreasing equilibrium vapour pressure (eq. 5.6) reduce the mass transfer. The drying rate thus slows down. During this stage macroscopic cracking may occur due to the moving fronts of retreating menisci, causing large stress gradients in the compact. The third stage starts when all the water in the surface pores has vanished. A fraction of small voids inside the particle compact is still filled with water. The compact now has its greatest strength, because the particles are 'glued' together by the menisci at their contacts. Further drying is due to vapour transport through capillary evaporation and condensation processes. Again the drying rate slows down. In the third stage no macroscopic shrinkage occurs. Further drying causes a loss of strength of the compact and may result in microscopic cracking.

During drying under the imposed conditions, not all the water will be removed. Besides some chemically bound water at the particle surfaces, adsorbed water remains present due to the lowered vapour pressure of highly curved water surfaces [7] in small pores and pore necks. This lowered vapour pressure is given by Kelvin's equation. For tubular pores, Kelvin's equation is given by :

$$\frac{p}{p_0} = \exp\left(\frac{2\gamma_w V_l}{r} \cdot \frac{1}{RT}\right) \quad [-] \quad (5.6)$$

with p [Pa] the vapour pressure above the curved water surface, p_0 [Pa] the saturated vapour pressure of water at 21 °C and 1 bar, R [J/mol K] the gas constant, γ_w [N/m] the surface tension of water, V_l [m³/mol] the molar volume of water at 21 °C, T [K] the temperature and r [m] the radius of curvature (negative in case of concave surfaces).

When p/p_0 equals the relative humidity, water cannot be evaporated. According to eq. 5.6 (assuming total wetting of the alumina surface), at RH=40% all pores with radii smaller than 1.2 nm remain filled with water.

Especially during the first two drying stages shrinkage occurs. During shrinkage relative particle positions continuously change. This causes reorganization, i.e. a relative change of the position of a particle with respect to its neighbouring particles. The effect of reorganization is determined by the initial wet microstructure and the conditions during drying. In figure 5.7 two extreme cases of shrinkage are shown, shrinkage with minor reorganization and shrinkage with strong reorganization.

Due to reorganization the mean coordination number, and thus the number of pores, increases.

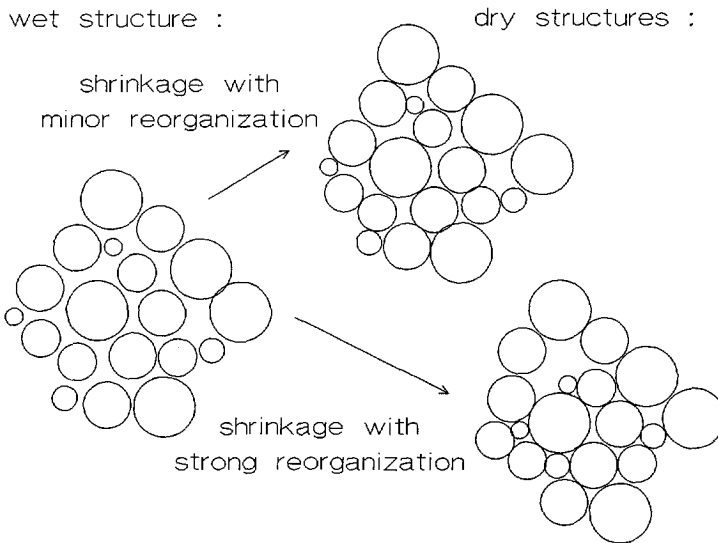


Figure 5.7 Shrinkage and reorganization

In general a dried compact has a clustered structure, consisting of dense regions which are slightly reorganized, separated by relatively open boundary zones where a strong reorganization has occurred. This precursors a grained structure. An example of such a structure is visualized by dried clay or dried mud soil.

During the third drying stage reorganization may occur due to vanishing water menisci at the interparticle contacts.

Particle compacts formed by pressure filtration and centrifugation will dry according to the above drying mechanisms. However, slip cast compacts cannot be removed due to the suction of the pores in the mould. The first and second drying stage are now influenced by the suction of the pores in the mould. This results in a (forced) increased drying rate. Because the structure of the wet compacts made by pressure filtration and slip casting are expected to be identical, we can observe how the increased drying rate due to mould suction affects the development of the ceramic microstructure.

Pre-sintering and porosity measurement

When the strength of dried compacts is increased by pre-sintering, samples can be taken without influencing the actual microstructure. The pre-sintering has to be done such that sintering restricts to neck growth between the smallest particles. This results in an increased strength of the compact, without major changes in porosity [8] and compact

structure. By examining the porosity of pre-sintered compacts, a good estimation of the porosity of dried compacts is obtained. Some reorganization of the compact structure will inevitably occur due to evaporation of water from the small pore fraction.

All compacts have been pre-sintered in air, using a temperature controlled Naber N20-74 oven. The compacts were heated at a rate of 100 °C/min to a temperature of 1050 °C. After 1 hr at 1050 °C, heating was stopped and the compacts in the oven cooled down to room temperature (± 30 °C/min).

Samples of about 1.5 g (near the compact centre) were taken using a diamond blade saw. The pore size distribution of such samples was investigated with a porometer (Carlo Erba Instr.), based on the incremental mercury intrusion at increasing pressure [8,9]. The neck size of the filled pores relates to the mercury pressure by equation 5.5, now with the surface tension of mercury γ_{Hg} . From the intrusion data an average hydraulic pore neck diameter can be calculated.

The dry relative density ϕ_{dry} [-] relates to the total intrusion volume of mercury per gram compact V_i [ml/g] through :

$$\phi_{dry} = 1 - \frac{V_i}{V_i + \frac{1}{\rho_{alumina}}} \quad [-] \quad [5.7]$$

With the known volume fractions of wet and dry (pre-sintered) structure, the amount of volumetric shrinkage can be determined (App. 5).

Sintering of particle compacts

Based on thermodynamics, a particle compact is unstable due to the high interfacial energy. Lowering of the interfacial energy by diminishing the interfacial area is a driving force for a particle compact to densify. Densification at an increased temperature enables mass transport. The following four processes may induce mass transport :

- evaporation-condensation
- surface diffusion
- bulk diffusion
- grain boundary diffusion

Theoretical considerations of these processes are given by Kingery et al. [10], Coble [11] and Johnson et al. [12].

The sintering of a particle compact may be divided in three stages [13] :

- the initial stage : The particle compact is characterized by the contacts between the particles. It constitutes an interconnected network, and a continuous pore system exists. The compact gains strength by neck-growth between the particles. The neck-growth is the result of evaporation-condensation, surface diffusion and bulk diffusion. During the initial stage material transport from less dense to dense regions (high coordination number) increases the initial local density variations. A clustered structure results, consisting of dense and less dense regions. During the initial stage, bulk diffusion is considered as the rate determining mechanism of shrinkage [11].
- the intermediate stage : The pore size diminishes until the continual pore system closes. This results in a discontinuous pore system, and grain boundaries are developed. The intermediate stage is characterized by a strong shrinkage, with material transport by means of bulk and grain boundary diffusion.
- the final stage : Some closed pores vanish, and grain growth or discontinuous grain growth may occur. This sinter stage will result in minor shrinkage, with material transport by means of bulk and/or grain boundary diffusion [14].

Under equal conditions, the shrinkage of the compacts was investigated by means of dilatometry. Dilatometry was performed in a gas tight alumina tube oven (fig. 5.8). The tube was flowed through with air.

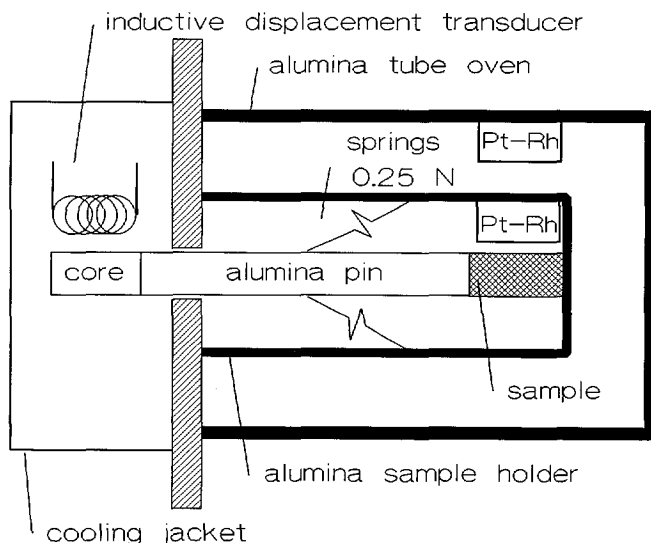


Figure 5.8 The Netsch Hochtemperatur Dilatometer 402 E

Of each group of densification experiments 3 samples (15*5*5 mm), sawn from the centre of the compacts, were investigated.

Of each sample the starting length L_0 was measured. The sample was heated at a rate of 5 K/min to 1500 °C in air. It remained for 1 hr at 1500 °C. Temperature was measured using Pt-Rh thermocouples. During heating, the sample temperature and length were recorded. After heating, the sample cooled down to room temperature at a rate of about 30 °C/min.

The densification rate followed from $d(\Delta L(t)/L_0)/dt$ [m/m s].

Assuming isotropic shrinkage, the linear shrinkage $\Delta L(T) = L_0 - L(T)$ relates to the relative density $D(T)$ [-] of the sample :

$$D(T) = D_{final} \cdot \left(\frac{L_{final}}{L_0 - \Delta L(T)} \right)^3 \quad [-] \quad (5.8)$$

with initial sample length L_0 [m] and the final sample length L_{final} [m].

The final relative density D_{final} [-] is found using Archimedes' method :

$$D_{final} = \frac{W_{dry}}{W_{dry} - W_{subm.}} \frac{\rho_{water}}{\rho_{alumina}} \quad [-] \quad (5.9)$$

with dry weight W_{dry} [g] and the in water submerged weight $W_{subm.}$ [g].

From equation 5.8 the initial relative density D_0 [-] may be evaluated using D_{final} , L_{final} , and L_0 . The results may be compared to the relative density of the pre-sintered compacts measured with mercury intrusion. When identical D_0 values are obtained, the transformation from linear shrinkage to relative density (eq. 5.8) is justified.

SEM investigation of microstructure development

To relate the shrinkage, as measured with dilatometry, to the development of the microstructure, samples of the pre-sintered compacts have been heat treated and examined with SEM. The heat treatments were chosen such that the structure development over a broad trajectory of compact density could be investigated. After the heat treatment the samples were ground and polished. To improve the visibility of particle contacts and grain boundaries in the sintered structures, the samples were thermally etched. Of each group of compacts, samples were exposed to the heat treatments shown in table 5.2 .

SEM micrographs have been taken at a magnification of 5000* .

Table 5.2 Heat treatments performed on the pre-sintered compacts

sintering at 5 K/min to :	thermal etching :
1100 °C, 5 hrs	1100 °C, 1 hr
1200 °C, 1 hr	1150 °C, 4 hrs
1300 °C, 1 hr	1250 °C, 1 hr
1400 °C, 1 hr	1350 °C, 0.5 hr
followed by natural cooling (± 30 °C/min)	

To investigate the grain size distribution, SEM micrographs of the structures sintered at 1400 °C were magnified 8 times (area) on paper. These enlargements were coated with a plastic layer to increase the weight. Through calibration, the weight of the grains has been related to the corresponding grain size area. A part of each structure, randomly chosen but large enough to eliminate influences of local microstructure variations, was cut into individual grains. Of each structure about 1000 grains were obtained. The grains were weighed and the corresponding grain size area was calculated. The grain size area was then converted to an equivalent diameter, assuming circular grains. The detection limit, determined by the possibility to accurately weigh the smallest cut grains, was 0.095 μm (equivalent grain diameter). For each structure, a number distribution of equivalent grain diameters could be obtained.

References

- [1] A. Roosen , H.K. Bowen , J. Am. Ceram. Soc. 71 [11] (1988) 970-977
- [2] B.C. Bonekamp , H.J. Veringa , Klei/Glas/Keramiek 8 (1986) 166-169
- [3] K.S. Venkataraman , R.A. Dimilia , J. Am. Ceram. Soc. 72 [1] (1989) 33-39
- [4] D.J. McClements , M.J.W. Povey , Adv. in Coll. Sci. 27 (1987) 285-316
- [5] A.H. Harker , J.A.G. Temple , J. Phys. D: Appl. Phys. 21 (1988) 1576-1588
- [6] T.M. Shaw , in "Better Ceramics Through Chemistry II , Vol. 73" , eds. C.J. Banker , D.E. Clark , D.R. Ulrich , MRS Pittsburg Penns. (1986) 215-223
- [7] J.F.F. Scholten , Katalyse and katalysatoren , Dep. of Chem. Techn. TH Delft (1985) 80-129

- [8] H.H.D. Lee , J. Am. Ceram. Soc. 73 [8] (1990) 2309-2315
- [9] R.G. Nyqvist , P.A. Nammensma , "Kwikporosimetrie, werking en mogelijkheden", ECN memo N° 86-155 (1986)
- [10] W.D. Kingery , M. Berg , J. Appl. Phys. 26 [10] (1958) 1205-1212
- [11] R.L. Coble , J. Am. Ceram. Soc. 41 [2] (1958) 55-62
- [12] D.L. Johnson , I.B. Cutler , J. Am. Ceram. Soc. 46 [11] (1963) 545-550
- [14] R.L. Coble , J. Appl. Phys. 32 [5] (1961) 787-792
- [15] T.-T. Fang , J. Mater. Sci. Lett. 7 (1988) 1068-1070

5.3 Results of compaction and characterization

Properties of the wet compacts

Pressure filtration

Filtration experiments were done with the stable (0.20-A) and the flocculated (0.20-C) suspension. A result of the measured pressure build-up and compact growth is shown in figure 5.9.

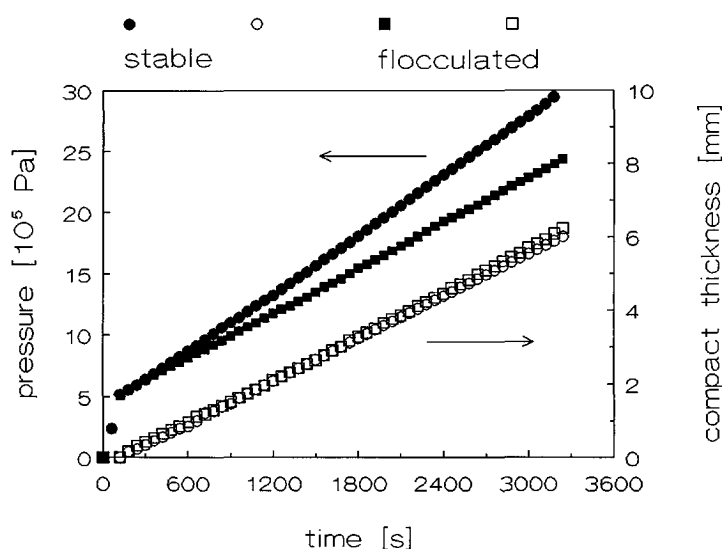


Figure 5.9 Pressure build-up and compact growth during filtration of the stable and the flocculated suspension

For both compacts, the compact thickness increases at a constant rate. This indicates the formation of incompressible compacts under these pressure conditions. When incompressible compacts are formed, the filtration pressure and the compact thickness should both increase linear with time. This has been found. From the pressure build-up, the compact porosity and permeability can then be calculated using classical filtration theory (section 2.2).

During filtration of the stable suspension (PF) the pressure increased more rapidly than with the flocculated suspension (PF-f). This indicates the formation of compacts with a

lower permeability. A lower compact porosity is thus expected, which is confirmed by the smaller growth rate from the stable suspension. However, a change in porosity has a stronger effect on the pressure build-up than on the compact thickness, because the permeability depends more strongly than linearly on the porosity (App. 1). The values for the pressure build-up and the rate of compact growth give for the two suspensions of different stability :

-PF (stable, 0.20-A)

$$K_c C = 2.14 \pm 0.08 \cdot 10^{-17} \text{ m}^2$$

$$\epsilon = 0.361 \pm 0.009 \text{ [-]}$$

indicating a compact permeability of $K_c = 0.97 \pm 0.06 \cdot 10^{-17} \text{ m}^2$

-PF-f (flocculated, 0.20-C)

$$K_c C = 2.77 \pm 0.19 \cdot 10^{-17} \text{ m}^2$$

$$\epsilon = 0.378 \pm 0.007 \text{ [-]}$$

indicating a compact permeability of $K_c = 1.31 \pm 0.11 \cdot 10^{-17} \text{ m}^2$

The compacts were formed at a constant Péclet number, $Pé = 0.76$. From eqs. 2.4 and 2.6, it follows that the pressure drop over the compact during filtration is $\Delta P_c = \Delta P / (1 + \Delta P_f / \Delta P_c)$. At the end of filtration, the maximum pressure drop was 25.7 bar for PF and 20.1 bar for PF-f. The shear rate in the consolidation zone remained constant at $\dot{\gamma} = 4.3 \cdot 10^4 \text{ s}^{-1}$ for PF and $3.2 \cdot 10^4 \text{ s}^{-1}$ for PF-f.

Slip casting

The slip casting experiment (SC) was done with the stable suspension (0.20-A). A result is shown in figure 5.10.

According to classical filtration theory (section 2.2), a linear increase in time of the squared compact thickness (H_c^2) is expected, independent of compact compressibility. In figure 5.10, H_c^2 curves slightly upwards and becomes linear after about 600 s. The initial curvature indicates a compact diameter which is smaller than the mould diameter. At the start, the water front progresses into the mould according to eq. 2.14. Because the water front spreads over the full surface of the mould, the average penetration depth of the waterfront in the mould is lower than according to eq. 2.14. After the water front has fully developed, the penetration velocity in the mould will be constant, but somewhat lower than according to eq. 2.14. Initially, the pressure drop over the mould thus decreases (eq. 2.4) to a finally constant but lower value. This results in a constant but higher than estimated pressure drop over the compact, and an increased rate of compact formation.

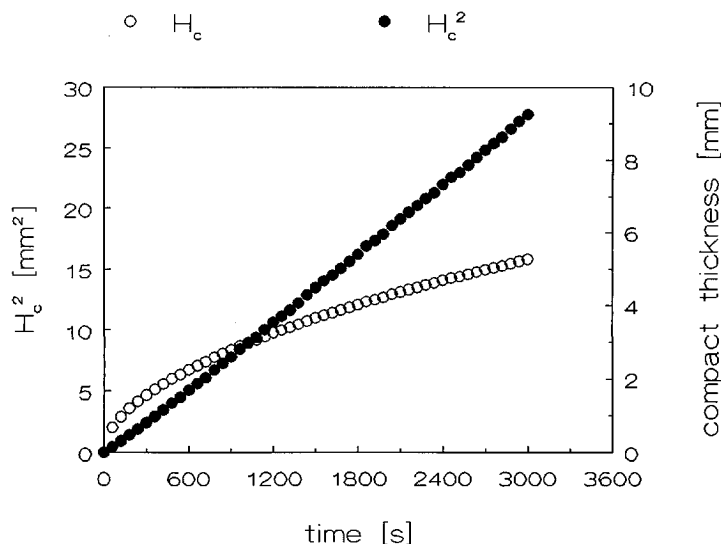


Figure 5.10 Compact growth during slipcasting of the stable suspension

After 600 s the total pressure drop is in accordance with the measured suction pressure of the mould (section 5.2).

For the stable suspension, the compact porosity and compact growth rate were measured independently as $\epsilon = 0.363 \pm 0.008$ and $H_c^2 = 9.34 \pm 0.21 \cdot 10^{-9} \text{ m}^2/\text{s}$. This indicates a compact permeability of $K_c = 1.14 \pm 0.27 \cdot 10^{-17} \text{ m}^2$. To find the value of K_c from the rate of compact formation with eq. 2.16, all measured mould characteristics are involved which, of course, leads to a relatively high uncertainty in K_c .

In slip casting the compacts initially form at an infinitely high Péclet number. Towards the end, the rate of compact growth has slowed down to about $1.1 \cdot 10^{-3} \text{ mm/s}$, corresponding with $Pé = 0.20$. In the linear part after 600 s, the constant pressure drop over the compact was about 9.0 bar (eqs. 2.4,6). The shear rate in the consolidation zone initially was infinitely high. At the end of filtration it had dropped to about $1.7 \cdot 10^4 \text{ s}^{-1}$ (eq. 2.19).

Centrifugation

In centrifugation of the stable suspension the Péclet numbers varied from 164 to 0.33. The measured porosity of the wet compacts (C) is shown in figure 5.11.

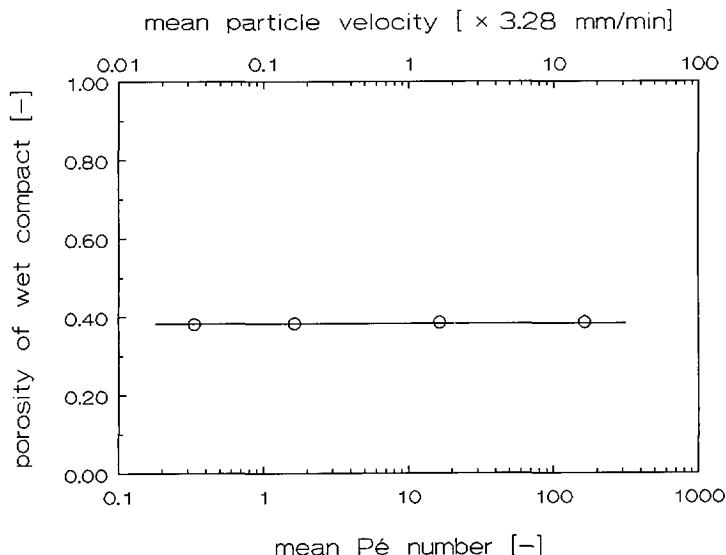


Figure 5.11 The porosity of wet compacts formed by centrifugation of the stable suspension

The pressure drop over the thickness of the centrifuged compacts varied from (eq. 2.34) 0.08 bar ($Pé = 0.33$) to 40.6 bar ($Pé = 164$). The porosity of the centrifuged compacts is not affected by these different combinations of pressure drop and $Pé$ number. For the stable suspension (0.20-A) the porosity remains constant at $\epsilon = 0.385 \pm 0.004$.

The effect of suspension and compaction parameters on the wet compact structure

In table 5.3 the measured properties of the wet compacts are summarized. The results show the expected strong influence of compaction conditions and variations in suspension stability on the porosity of the formed wet compacts.

In case of ideal compaction (pressure filtration, slip casting), fluid shear in the consolidation zone densifies the consolidation zone. The densification of the random and open stacked consolidation zone is opposed by particle drag, which is described by the parameters q and I^2 . Stable or slightly flocculated A16SG-F suspensions ($I^2 < 1/3$) should densify to $\phi_{\max, \infty} = 0.63 \pm 0.01$, the density of the random dense packed A16SG-F powder. In case of strongly flocculated suspensions a lower density of the wet compacts has been predicted, $\phi_{\max, \infty} / (3I^2)$.

Table 5.3 Properties of the wet compacts

	$K_c C$ [10^{-17} m^2]	$\phi_{\text{wet}} [-]$	K_c [10^{-17} m^2]
<u>Ideal consolidation</u>			
stable (PF)	2.14 ± 0.08	0.639 ± 0.009	0.97 ± 0.06
stable (SC)	---	0.637 ± 0.008	1.14 ± 0.27
flocculated (PF-f)	2.77 ± 0.19	0.622 ± 0.007	1.31 ± 0.11
<u>Counterflow</u>			
stable (C)	---	0.615 ± 0.004	---

As assumed in our rheological model, the wet compacts in pressure filtration and slip casting form under a very high shear rate. The densities of the wet compacts formed by the stable suspension 0.20-A ($I^2 \sim 0.28$) with these methods reach $\phi_{\text{max}, \infty}$, as expected. The relative density of the PF-f compacts (0.20-C, $I^2 = 0.36 \pm 0.04$) was lower than the density of the PF and SC compacts, which leads to an increased porosity and a higher permeability.

From the measured value of $\phi_{\text{wet}} = 0.622 \pm 0.007$ for the PF-f compacts follows an I^2 of 0.34, which is in good agreement with $I^2 = 0.36$ as determined from the rheology of that suspension.

Centrifugation is a "non ideal" compaction method, because the counter flow of fluid opposes the densification of the initially open and ordered consolidation zone. In centrifugation, less dense but ordered particle compacts are expected. This is confirmed by the experimental results. Compared with the ideal consolidation methods PF and SC, a lower relative density of the C compacts, $\phi_{\text{wet}} = 0.615 \pm 0.004$, is obtained.

- Therefore, at this stage we come to the conclusion that rheological measurements, interpreted in terms of the drag parameters q and I^2 , can predict the influence of the suspension stability on the density of wet compacts, which are produced with different consolidation methods.
- Our assumption about the strong influence of the relative direction of particle motion and fluid flow on compact formation is also confirmed. Counterflow of fluid during consolidation results in the formation of less dense wet compacts.

Properties of the dried and pre-sintered compacts

Drying shrinkage

In table 5.4 the wet and dry densities of the compacts are compared. The values of ϕ_{dry} have been measured with mercury intrusion porosimetry. The shrinkage has been calculated with eq. A5.3 .

Table 5.4 The porosity of the wet and dry compacts, and the amount of volumetric shrinkage

	ϕ_{wet} [-]	ϕ_{dry} [-] (eq. 5.7)	$\Delta V/V_{\text{wet}}$ [%]
<u>Ideal consolidation</u>			
stable (PF)	0.639 ± 0.009	0.704 ± 0.004	- 9.2 %
stable, forced drying (SC)	0.637 ± 0.008	0.673 ± 0.003	- 5.3 %
flocculated (PF-f)	0.622 ± 0.007	0.677 ± 0.003	- 8.1 %
<u>Counterflow</u>			
stable (C)	0.615 ± 0.004	0.655 ± 0.004	- 6.0 %

The pressure filtrated and centrifuged compacts were dried under equal conditions (section 5.2). The data show that the initial stacking of the particles, the strength of particle attraction (I^2), and the drying conditions, can considerably influence the shrinkage of a compact due to drying.

In pressure filtration, the wet compacts of a stable suspension were more densely packed than the PF-f compacts. Upon drying, the difference in density did increase even further. Under the given drying conditions, a random, dense packed compact, consisting of particles with a relatively weak net attraction (PF), allows for more shrinkage than a random open packed particle compact (PF-f) of particles with a strong net attraction.

As a result of the difference in fluid flow directions, the (stable) wet PF compacts were more densely packed than the C compacts. During drying both would shrink, and again the difference in density increased.

- Apparently, with equal interaction between the particles, a random dense stacked compact (PF) will shrink more than an open and ordered stacked compact (C).

Because the SC and PF compacts were formed under comparable consolidation conditions, the structures of these compacts were expected to be identical. This was borne

out by the equal densities of the wet SC and PF compacts. However, in an uninterrupted slip casting process, absorption of water from the compact by the mould causes forced drying at a high rate. This forced drying of the SC compacts resulted in a reduced drying shrinkage compared with the PF compacts.

- **Drying by suction, like in slip casting, strongly reduces the shrinkage of a random dense packed particle compact.**

As a result of drying, all our compacts showed cracks. Those formed from the stable suspension by slip casting (SC) had very few cracks. The compacts formed by pressure filtration of the stable (PF) and flocculated suspension (PF-f) showed some cracks. Centrifuged compacts of the stable suspension (C) were most strongly cracked. These differences in strength relate to the obtained differences in density ϕ_{dry} , table 5.4 .

Lightly sintered compacts

Lightly pre-sintered compacts are strong enough to allow the determination of pore (neck) size distributions in their porosity. Such distributions are shown in figure 5.12 .

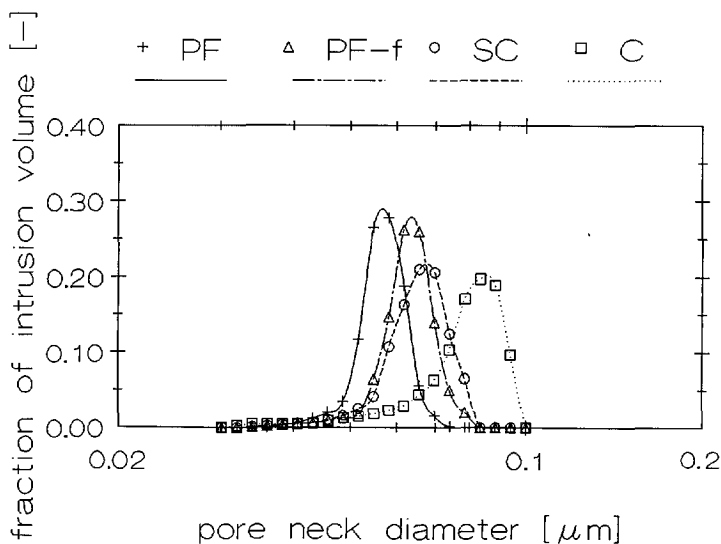


Figure 5.12 The pore neck size distributions of the pre-sintered compacts
Peak values [μm] : + 0.057 Δ 0.063 o 0.068 \square 0.08

Mercury intrusion cannot detect large internal voids [1]. Therefore the compact structures were also examined with SEM. Macroscopic defects inside the compacts were not found. Larger wet compact porosities, as obtained with the different preparation methods, shift the neck size distribution towards increased diameters. All compacts have a fraction of small pore necks, down to $0.03\ \mu\text{m}$. Due to this fraction of small pores, all histograms deviate from a log-normal distribution. The C and SC compacts have less sharp neck size distributions.

- **A random packed structure, formed by ideal consolidation, allows for small but randomly oriented particle displacements during drying. Such displacements result in reorganization, however, without much clustering within the original structure.** The randomly oriented particle displacements account for the strong shrinkage during drying, and result in a homogeneous dried structure with only small local variations in density. These dried compacts have a sharp pore neck size distribution, due to small local density variations.
- **A larger net particle attraction (PF-f), i.e. an increased I^2 , hinders the shrinkage of a random packed structure. Compared with PF, drying of the flocculated PF-f compacts involves less reorganization of the microstructure.** The PF-f compacts have a sharp pore distribution, but, compared with the PF compacts, a larger average interparticle distance.

Without strong clustering upon drying, cracking of the PF and PF-f compacts was not expected. The observed little cracking is believed to be related to the strong shrinkage in combination with the dimensions of the compacts.

- **The extra effect of a forced drying rate reduces the probability of random particle displacements. A suppressed reorganization is the result. This leads to a "frozen" wet structure.** The SC compacts show less shrinkage than the PF experiments. The suppressed reorganization appears to have given a slightly increased width of the pore distribution. Compared with PF and PF-f, the final dried SC compacts have a larger average interparticle distance.

Had there be clustering of particles in combination with the little shrinkage of the slip cast compacts, then this would have caused a wider pore size distribution. As can be seen in figure 5.12, however, the pore distribution was relatively sharp, which indicates the absence of clustering. Without the local pressure differences due to clustering, cracking during drying is not likely. The very few small cracks may have resulted from the mould/compact contact. This contact induces a reduced freedom of shrinkage for the adjacent layer of the compact.

- During drying, the open structure of the C compacts (counterflow) allows large particle displacements of individual particles. In an ordered structure these particle displacements will be non-randomly oriented and do not contribute much to shrinkage. The dried C compacts thus retain a low density.
- Reorganization of the ordered compact during drying causes a strongly clustered dry particle packing, with dense and less dense regions. Such a structure would tend towards a bimodal pore size distribution (fig. 5.12) .

During drying, the development of dense and less dense regions induces strong local pressure differences (eq. 5.5) . These account for the strong cracking of the centrifuged compacts.

Microstructure development during sintering

Dilatometry

The densification during sintering of the different compacts is shown in figure 5.13.

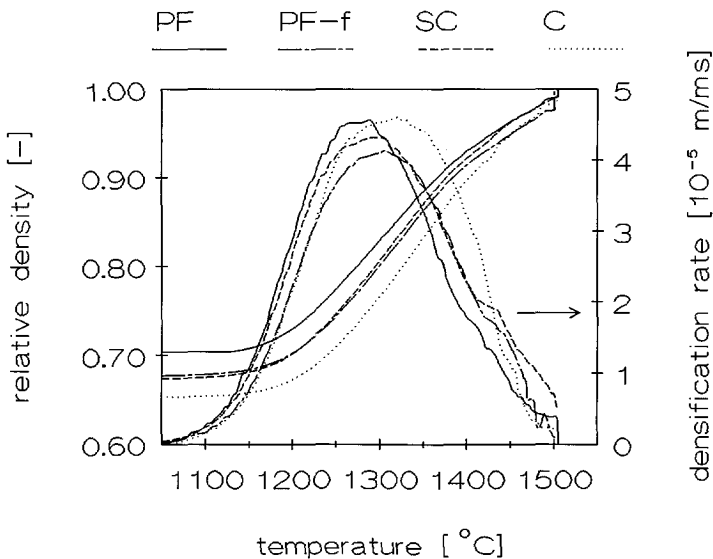


Figure 5.13 Density (eq. 5.8) and densification rate of the compacts (dilatometry)

Differences in the density of the dried compacts, strongly affect the shrinkage. For all compacts, densification starts well above the pre-sinter temperature of 1050 °C.

Close to the final density, obtained at the end of sintering, differences in density between the initially more dense compacts and the more open compacts are still visible. The initially more dense compacts reach the maximum rate of densification at a lower temperature.

- A higher porosity of the dried compacts relates to a decreased mean coordination number of the particles, which causes the initial slower rate of densification of the open compacts.

Through the measured relative final density D_{final} , the initial relative density D_0 of the pre-sintered compacts was estimated. These values are shown in table 5.5, with the porosity of the dried compacts as determined with mercury intrusion .

Table 5.5 The final relative density D_{final} [-] and the initial relative density D_0 [-] of the compacts as measured with dilatometry (eqs. 5.8-9)

	D_{final} [-]	D_0 [-]	ϕ_{dry} [-]
<u>Ideal compaction</u>			
stable (PF)	0.997 ± 0.002	0.690 ± 0.006	0.704 ± 0.004
stable, forced drying (SC)	0.996 ± 0.001	0.665 ± 0.008	0.673 ± 0.003
flocculated (PF-f)	0.996 ± 0.003	0.679 ± 0.003	0.677 ± 0.003
<u>Counterflow</u>			
stable (C)	0.995 ± 0.003	0.648 ± 0.005	0.655 ± 0.004

The calculated D_0 values agree with ϕ_{dry} , within a maximum deviation of 2.0 % . The applied transformation (eq. 5.8) to obtain the relative density from the measured shrinkage, is thus justified.

As shown, the pore size distribution of the pre-sintered compacts was influenced by compaction parameters, the strength of particle interaction and the rate of drying. However, the final density of the compacts was not influenced by the initial density differences of the dry compacts.

Microstructure development

The development of microstructure during sintering has been investigated by SEM. The micrographs of the structures are shown in appendix 6.

Properties of the dry structures have clearly influenced the development of microstructure during sintering.

As can be seen, at a temperature of 1300 °C the PF structure was already quite dense. The PF-f and SC structures were less dense, and the C structure still was quite open. This relates to the densification curves shown in figure 5.13. From the micrographs it can be seen that at 1200 °C the structures still consist of individual particles, while at 1300 °C a more or less grained structure is developing. The intermediate sintering stage thus starts between 1200 °C and 1300 °C.

During sintering, local density variations which are present initially do increase. The clustering in the microstructure becomes more pronounced. In the beginning of the sinter process, when the interparticle distances are still relatively large, the effect of clustering will be strong. Clustering thus precedes major densification. In figure 5.14, the development of the clustering of the microstructure of the different compacts is shown. It is based on a visual observation of the micrographs.

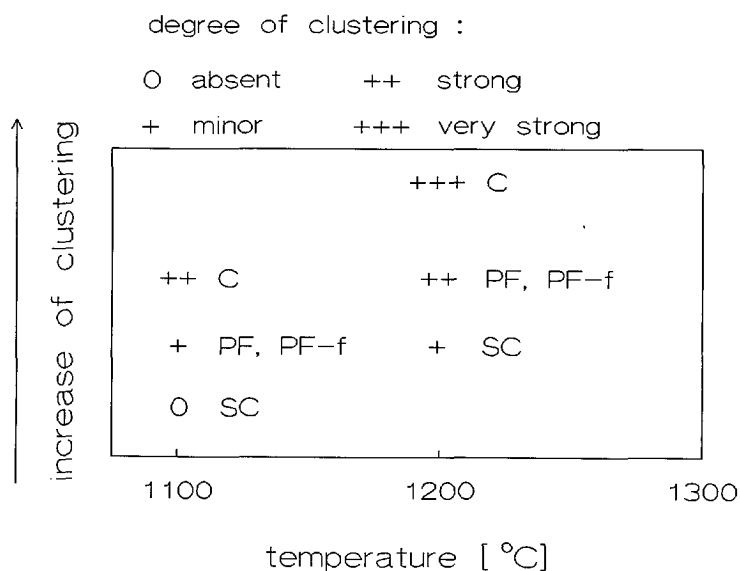


Figure 5.14 Clustering of the microstructures during sintering

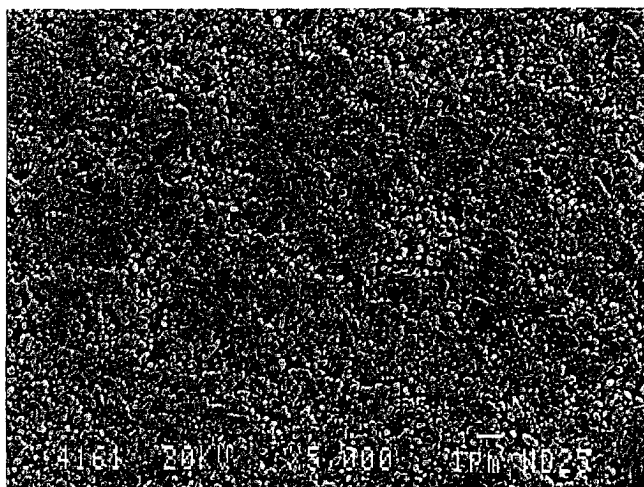


Figure 5.15 Microstructure of a slipcast compact,
SC at 1100 °C

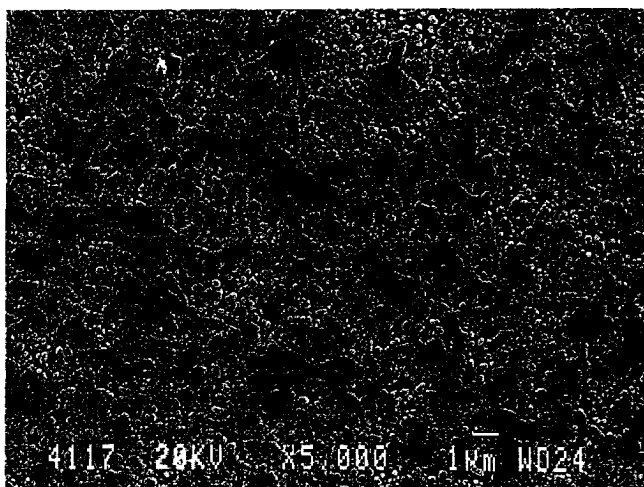


Figure 5.16 Microstructure of a centrifuged compact,
C at 1100 °C

- The results of the dried PF and PF-f compacts indicated minor clustering. Indeed little clustering is seen in the micrographs at 1100 °C. Due to the dense structure of PF the clustering did not develop as strongly as in the case of PF-f. This is confirmed by the micrographs at 1200 °C.
- The results of drying indicated that the dried slip cast compacts were not clustered at all. This is confirmed by the micrograph of the structure at 1100 °C (fig. 5.15). Due to the absence of strong local density differences, in combination with a relative high density, at an increasing temperature the micrographs show only a slightly increased clustering.
- The results of the dried centrifuged compacts indicated a strongly clustered structure. In the micrograph of the structure at 1100 °C (fig. 5.16) this is clearly visible. Due to the strong density variations and the relatively open structure, the clustering proceeded at increasing temperature.

Grain size distribution

The grain size distributions of the structures sintered at 1400 °C are shown in figure 5.17.

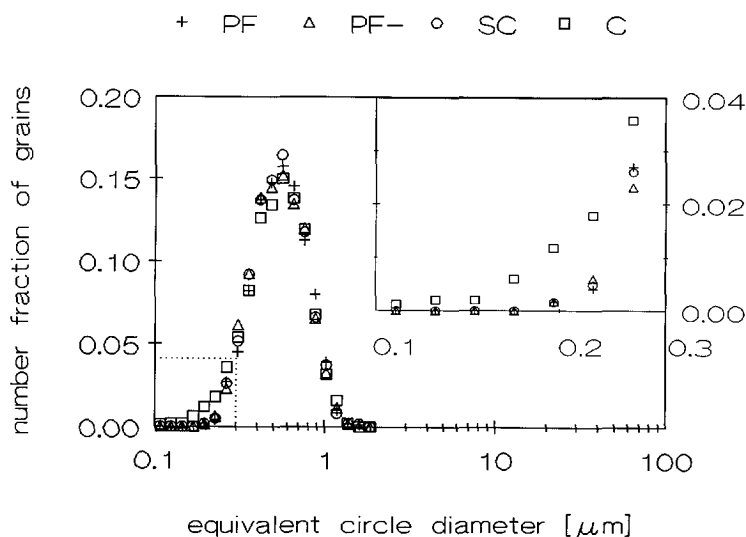


Figure 5.17 The grain size distribution of the structures sintered at 1400 °C

In obtaining the distribution, the number of counted grains was taken large enough to eliminate the influence of local microstructure variations on the grain size distribution. The smallest grains present in the distribution were well above the detection limit.

The grain histograms of the compacts formed by ideal compaction (PF, PF-f and SC) resembled log-normal distributions. The compacts formed by counterflow (C) have an increased fraction of small grains, resulting in a slight deviation from a log-normal distribution.

The increased fraction of small grains is supported by the results of image analysis [2], shown in figure 5.18.

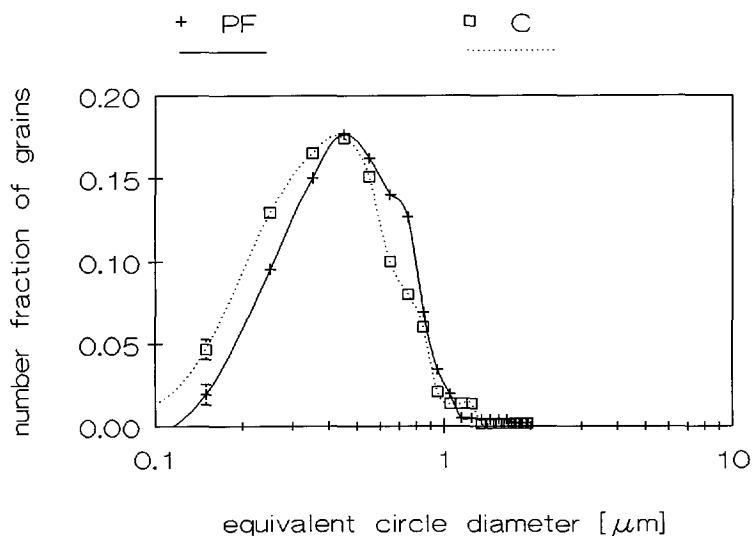


Figure 5.18 The grain size distribution of PF and C at 1400 °C, obtained with image analysis

The fitted parameters of the log-normal distributions are shown in table 5.6 .

Table 5.6 The parameters of the fitted grain size distribution (log-normal) of the sintered compacts (1400 °C)

	d_g^n [μm]	σ [-]
<u>Ideal compaction</u>		
stable (PF)	0.544 ± 0.005	0.371 ± 0.008
stable, forced drying (SC)	0.535 ± 0.004	0.367 ± 0.007
flocculated (PF-f)	0.536 ± 0.007	0.38 ± 0.01
<u>Counterflow</u>		
stable (C)	$0.539 \pm 0.006^*$	$0.392 \pm 0.009^*$

* slightly deviating from a log-normal distribution

The original A16SG-F powder had a log-normal size distribution, with a mean particle size of $D_g^n = 0.24 \mu\text{m}$. For all structures, D_g^n increased compared with the original powder. This indicates the occurrence of grain growth.

The larger fraction of small particles in the structure of C indicates that a substantial number of original powder particles was not eliminated by sintering. Clustering affects the local stress distribution during sintering [3]. Regions with high stress will shrink, while regions with low stress remain open. In the strongly clustered C structure, certain regions did not densify during the intermediate sintering stages. This finally resulted in the increased fraction of small grains.

- Compared with the random structures formed by ideal compaction, the sintering of a strongly clustered structure (counterflow) yields a grain size distribution with an increased fraction of small grains.

Physical properties like strength and hardness of well processed ceramics with a narrow grain size distribution are mainly affected by the mean and the standard deviation of the size distribution [4]. As can be seen in table 5.6, D_g^n and σ do not vary significantly for the different structures.

- Under the imposed sintering conditions, the strong differences in the ordering of the initial microstructures were levelled off considerably.

During sintering, densification results from particle rearrangement and particle deformation due to bulk and grain boundary diffusion. For a given powder, the actual densification mechanism depends on the sintering temperature and on the structure of the porous compact [3,5-6].

Variation of the time-temperature program of sintering offers a possibility to control the development of the ceramic microstructure. Differences in the ordering of the initial structures can be developed, through temperature control, into different sintered microstructures.

References

- [1] H.H.D. Lee , J. Am. Ceram. Soc. 73 [8] (1990) 2309-2315
- [2] J.G. Berryman , S.C. Blair , J. Appl. Phys. 60 [6] (1986) 1930-1938
- [3] T.M.G. Senden , A.H.M. Verhoeven (eds) , "The role of particle interactions in powder mechanics" , EFCE Publication, series 28, Eindhoven (1983)
- [4] pers. commun. with G. the With , Techn Univ. of Eindhoven (1994)
- [5] R.J. Brook , Sci. Ceram. 9 (1977) 57-67
- [6] T. Kimura , Y. Matsuda , M. Oda , T. Yamaguchi , Ceram. Int. 13 (1987)

Chapter 6

Thesis

The link between rheology and ideal consolidation, through the drag effect, enables the prediction of the wet compact density and the dependence of wet compact density on suspension stability through rheological investigation.

In ideal compaction of particles from a suspension, the densification of the consolidation zone (in which the wet compact is formed and structured) is promoted by the fluid flow past the consolidating particles.

These particles affect each other by the drag effect. The magnitude of the drag effect depends on the mean coordination number q of the particles, and on the strength of the interaction between the particles by surface forces.

These same factors determine the rheology of a concentrated suspension, which has been described in the Giant-Floc model.

Compaction of suspensions involves very high shear rates. The Giant-Floc model relates the high shear limiting viscosity of a concentrated suspension with the drag parameters q and l^2 and also with the volume fraction ϕ_v of the particles in the consolidation zone.

For a given suspension stability (l^2), when ϕ_v is increased, the high shear limiting viscosity finally diverges at a volume fraction ϕ_{div} . At this volume fraction the drag effect blocks particle motion. With ideal compaction, resulting in random packed compacts, a suspension thus can be densified to ϕ_{div} . The adapted Giant-Floc model relates ϕ_{div} with l^2 . When l^2 is smaller than $1/3$, ϕ_{div} is equal to $\phi_{max,\infty}$, the density of the random dense particle packing. $\phi_{max,\infty}$ is an intrinsic powder quality, and depends on the size and shape distribution of the particles. When l^2 exceeds $1/3$, ϕ_{div} decreases to $\phi_{max,\infty}/(3l^2)$.

The direction of the fluid flow, experienced by the consolidating particles, strongly influences wet compact structure.

When fluid flow promotes densification of the consolidation zone, the resulting particle compacts are randomly packed. The density of these compacts depends on the shape and size distribution of the powder, and on the interaction parameter l^2 .

When fluid flow opposes densification (counterflow), the resulting particle packing has an ordered structure. Such compacts have a lower density than the randomly packed compacts formed by ideal compaction.

The initial wet compact structure influences the development of the dried structure.

During drying, the particle displacements in a random structure (formed by ideal compaction) are randomly oriented. Reorganization during the drying of random packed compacts results in dry compacts with a random structure.

Particle displacements in ordered particle packings (counterflow) increase the initial local density variations. The dry compacts have a strongly clustered structure. Compared with the drying of random particle packings, the shrinkage is strongly reduced.

An increased particle attraction (I^2), but also a rapid drying process, like the one following slip casting, reduce the extent of the reorganization process, which results in a reduced drying shrinkage.

Cracking depends on the size and shape of the compact, on the extent of reorganization and on the percentage of shrinkage during drying. Oriented reorganization, as well as a strong shrinkage, promote cracking.

The sinter rates reflect the internal green structure of a particle compact and can therefore be affected by the method of wet consolidation.

Differences in the densification curves persist up to the theoretical density of a sintered product. In the initial stages of sintering, differences between ordered and randomly packed structures increase, due to a proceeding clustering of the ordered structures. Dry compacts with a higher porosity initially have a slower rate of densification.

The sintering of a randomly packed particle compact, formed from a log-normal distributed powder, gives a sintered product with a log-normal grain size distribution. Strong clustering affects the grain size distribution. It results in an increased fraction of small grains, which causes the distribution to deviate from log-normal.

From the above, we come to the conclusion that : **The way in which particles interact during wet consolidation is an essential factor in determining the quality of a ceramic product which results from the sintering of a particle compact.** Therefore, our thesis is that :

In wet compaction, the flow of the fluid surrounding the consolidating particles must be controlled, in order to master the quality of sintered ceramics.

Appendices

Appendix 1 The permeability of a particle compact

The permeability K [m^2] of particle packing is determined by the nature of the particle packing. On a semi-empirical basis Kozeny [1] proposed a relation between the permeability and the porosity of a particle compact. A porous material is considered as a dense material containing non interconnected tubular pores, in such a way that the pore diameter is related to the particle diameter, while the number of the tubular pores is determined by the porosity of the particle compact. Utilizing the Hagen-Poiseuille flow relation [2] the Carman-Kozeny relation can be deduced [3] :

$$K = \frac{\varepsilon^3}{k (1-\varepsilon)^2 S_v^2} \quad [m^2] \quad (A1.1)$$

with the particle specific surface area S_v [m^2/m^3]. The Kozeny constant k [-] is an empirical parameter introduced to account for the tortuosity (interconnectivity and meandering) of the porous system, values of k are usually found in the interval 2-10.

Ingmanson and Andrews [4] proposed a description of the Kozeny constant in terms of porosity :

$$k = 3.5 \frac{\varepsilon^3}{\sqrt{1-\varepsilon}} \{ 1 + 57(1-\varepsilon)^3 \} \quad [-] \quad (A1.2)$$

The specific surface area S_v of a powder follows from the surface area S_{BET} [m^2/g] as measured with nitrogen adsorption :

$$S_v = 10^6 \rho S_{BET} \quad [m^2/m^3] \quad (A1.3)$$

with ρ [g/cm^3] the density of the particles.

When the porosity of a particle compact is known, as well as the mean particle size, the BET-area and the density of the particles, a good estimation of the permeability of the particle compact may be obtained by means of eq. A1.1-3 .

References

- [1] J. Kozeny , *Wasserkraft & Wasserwirtschaft* 22 (1927) 67-86
- [2] J. M. Smith , E. Stammers , L.P.B.M. Janssen , *Fysische Transportverschijnselen I*, DUM BV , Delft Holland (1981) page 15
- [3] G.J. Kok , P.L. Zuiderveld , *Fysisch Technische Scheidingsmethoden* , DUM BV, Delft Holland (1973) 257-266
- [4] W.L. Ingmanson , B.D. Andrews , *Tappi* 46 (1963) page 150

Appendix 2 Derivation of the geometrical constants of a concentric cylinder system

Here we will be concerned with a general derivation of the geometrical constants G_r [m^3] and $G_{\dot{\gamma}}$ [-] (eqs. 4.6-7) appertaining to a concentric cylinder measurement systems as shown in figures 4.6. and 4.7. For sake of simplicity the geometric constants will be derived based on a CC geometry. The DCC geometry may be considered as two combined CC geometries, resulting in analogous derivations.

We consider the case of a cylinder with height H [m] and radius R_1 [m], submerged in a fluid contained by a symmetrically placed cylindrical container with radius R_2 [m], and rotating with a stationary angular velocity $\Omega = d\theta/dt$ [s^{-1}]. Top and bottom side of the cylinder will be neglected when considering force transfer from rotor (via fluid) to container (see figure 4.7).

At each position r [R_1, R_2] measured from the central axis of the rotor, we can establish a force balance matching the externally imposed torque T [Nm] on the rotor with the shear stress $\tau_{r,\theta}$ [Pa] experienced by the fluid [1] :

$$\tau_r = -\tau_{r\theta} = \frac{T}{2\pi Hr^2} \quad [N/m^2] \quad (A2-1)$$

Thus the spatial distribution of the shear stress is known.

The shear rate at position r in the fluid is given by :

$$\dot{\gamma}_r = -r \frac{d\omega_r}{dr} \quad [s^{-1}] \quad (A2-2)$$

with local angular fluid velocity ω_r [s^{-1}].

In rheology, it is convenient to define both shear stress τ_r (working on the fluid in direction θ on a plane with its normal in direction r) and shear rate $\dot{\gamma}_r$ as positive quantities [2].

At each radial position r , the local shear stress τ_r and shear rate $\dot{\gamma}_r$ are coupled through a constitutional equation describing the viscosity behaviour of the fluid, which generally depends on shear rate. For the derivation of the geometric constants we will consider a shear thinning fluid exhibiting power law type behaviour (both τ_r and $\dot{\gamma}$ positive) :

$$\tau_r = k \dot{\gamma}_r^n, \quad 0 < n \leq 1 \quad [N/m^2] \quad (A2-3)$$

with constant k [$Pa \cdot s^n$]. In the limit of $n=1$ we find Newtonian behaviour, $k = \eta_0$ [$Pa \cdot s$]. A relation between the rotor's angular velocity Ω and imposed torque T may be derived combining eqs. A2-1 to 3 and subsequent integration over r using the appropriate boundary conditions [2] :

$$\Omega = \frac{n}{2} (R_1^{-\frac{2}{n}} - R_2^{-\frac{2}{n}}) \left(\frac{1}{2\pi Hk} \right)^{\frac{1}{n}} T^{\frac{1}{n}} \quad [s^{-1}] \quad (A2-4)$$

The spatial distribution of shear rate may now be derived by combining equations A2-1,3 and 4 :

$$\dot{\gamma}_r = \frac{2}{n} \frac{1}{(R_1^{\frac{2}{n}} - R_2^{\frac{2}{n}})} r^{-\frac{2}{n}} \Omega \quad [s^{-1}] \quad (A2-5)$$

Through eqs. A2-1,5 the spatial distribution of both shear stress and shear rate is now known. In contrary to the spatial distribution of shear stress the distribution of shear rate depends on the viscous behaviour of the suspension, characterized by the value of the power law exponent n .

The spatial averages of shear stress and shear rate are obtained by resp.

$$\bar{\tau} = \frac{\int 2\pi r \tau_r dr}{\int 2\pi r dr} \quad [N/m^2] \quad (A2-6)$$

$$\bar{\dot{\gamma}} = \frac{\int 2\pi r \dot{\gamma}_r dr}{\int 2\pi r dr} \quad [s^{-1}] \quad (A2-7)$$

For well designed concentric systems the gap is chosen to be small compared to the radius, $R_2 - R_1 \ll R_1$, in order to obtain a linear shear stress profile, see figure A2-1.

Combining eqs. A2-1,6 and integrating over the appropriate boundary conditions, assuming $R_2 - R_1 \ll R_1$, the spatially averaged shear stress is given by

$$\bar{\tau} = G_\tau T = \frac{R_1^2 + R_2^2}{4\pi H R_1^2 R_2^2} T \quad [N/m^2] \quad (A2-8)$$

In case of a Newtonian fluid ($n=1$), assuming $R_2 - R_1 \ll R_1$, the spatially averaged shear rate may be derived by combining eqs. A2-5,7 :

$$\bar{\dot{\gamma}} = G_{\dot{\gamma}} \Omega = \frac{R_1^2 + R_2^2}{R_2^2 - R_1^2} \Omega \quad [s^{-1}] \quad (A2-9)$$

In case of a shear thinning fluid ($n < 1$), by combining eqs. A2-5,7, the spatially averaged shear rate results in [3] :

$$\bar{\dot{\gamma}} = G_{\dot{\gamma}} \Omega = \frac{2}{1-n} \frac{1}{R_2^2 - R_1^2} \frac{R_2^{2-\frac{2}{n}} - R_1^{2-\frac{2}{n}}}{R_1^{-\frac{2}{n}} - R_2^{-\frac{2}{n}}} \Omega \quad [\text{s}^{-1}] \quad (\text{A2-10})$$

The spatially averaged shear rate thus depends on the value of the power law's exponent n . Through eqs. A2-8 to 10 the geometrical constants G_r [m^{-3}] and $G_{\dot{\gamma}}$ [-] are known for Newtonian fluids and fluids with power law type behaviour.

Considering Newtonian fluids, using the geometrical constants given by eqs. A2-8,9, the spatially averaged shear stress and shear rate can be directly calculated through the known dimensions of the measurement system. Thus the true viscosity of a fluid may be determined from a set of measured T, Ω data.

In case of measuring viscosity data of a shear thinning fluid n is initially unknown. The spatially averaged shear rate therefore cannot be calculated using the measured Ω data before an estimation of n has been made. Thus the true viscosity cannot be determined from a set of T, Ω data. To get around this difficulty, in practice, the spatial mean shear rate is calculated assuming Newtonian behaviour, equation A2-9. We then obtain apparent values for the spatial mean shear rate and the resulting true viscosity. The value of n may then be estimated and the spatial mean shear rate data can be recalculated using equation A2-10. When necessary this iterative procedure can be repeated. However, using measurement geometries with a small gap ($R_2 - R_1$), and/or measuring a suspension with not to extreme shear thinning behaviour, usage of the apparent values of the spatial mean shear rate only introduces a minor error.

In figure A2-1 the characteristic shear profiles $\dot{\gamma}_r$ [-] for both a Newtonian and a shear thinning fluid are visualized assuming $R_2 - R_1 \ll R_1$. In case of a Newtonian fluid, both shear stress and shear rate may be considered linear dependent on radial position. In case of a small gap, local shear stresses and shear rates will only weakly deviate from the calculated spatial averages (eqs. A2-8,9). The accompanying shear profile will be parabolical.

In case of shear thinning behaviour, again the shear stress will be linear dependent on radial position. Thus the local shear stresses will only weakly deviate from the spatial average (eq. A2-8). The local shear rates, however, deviate strongly from the calculated spatial average (eq. A2-10). The accompanying shear profile will deviate from parabolic behaviour.

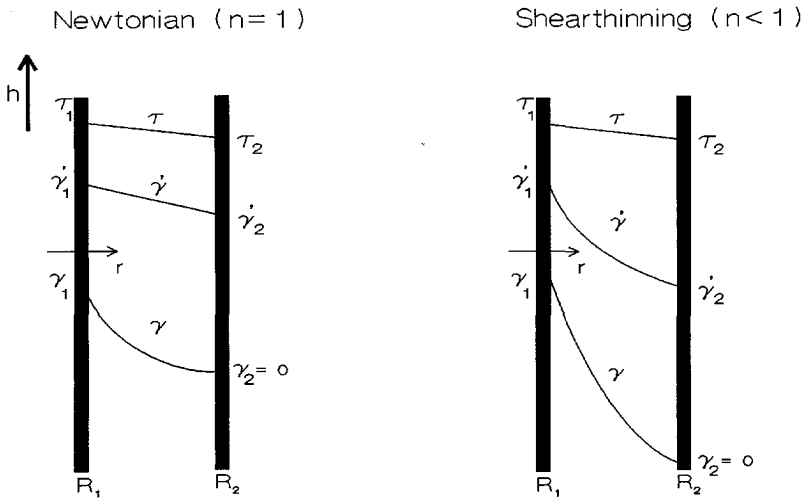


Figure A2-1 The flow profile of a Newtonian and a Power law fluid in a concentric cylinder measurement system in case of $(R_2 - R_1) < R_1$

The dimensions of the used stainless steel medium concentric cylinder CC (rotor N° 5275) are : $R_1 = 13.83$ mm, $R_2 = 15.00$ mm and $H = 32$ mm.

The gap between the bottom of the rotor and the stator was set at 4 mm. The necessary sample volume was 9 ml.

Using the above dimensions, the geometrical constants were calculated to be, according to eqs. A2-8 and A2-9, $G_r = 24.05 \cdot 10^3$ [m⁻³] and $G_\gamma = 12.34$ [-].

Even assuming extremely strong shear thinning behaviour, for example $n = 0.1$, only an error of -2.3 % is introduced when using eq. A2-9 in stead of eq. A2-10 to calculate G_γ . According to these geometrical constants the measuring range of the CC configuration is given by $0.024 \leq \tau \leq 240$ Pa and $1.2 \cdot 10^{-3} \leq \dot{\gamma} \leq 615$ s⁻¹.

This enables accurate measurement of (Newtonian) viscosities (between 10-90 % of full scales of τ and $\dot{\gamma}$) between 43 mPas $\leq \eta \leq 3.5$ Pa s.

The dimensions of the used stainless steel double concentric cylinder DCC measurement geometry (rotor N° 5271) are : $R_1 = 20.00$ mm, $R_2 = 20.38$ mm, $R_3 = 21.96$ mm, $R_4 = 22.38$ mm and $H = 20.5$ mm.

The gap between bottom of the rotor and the stator was set at 500 μm . The sample volume needed was 3.5 ml.

The DCC geometry is designed to obtain identical stress and shear rate profiles in both gaps, thus $(R_2 - R_1)/R_1 = (R_4 - R_3)/R_3$. The imposed torque is then divided equally over both gaps. Analogous to eq. A2-8, the following G_τ has been derived :

$$G_\tau = \frac{R_1^2 + R_2^2}{4 \pi H R_2^2 (R_1^2 + R_3^2)} \quad [m^{-3}] \quad (\text{A2-11})$$

From eq. A2-11, using the above dimensions G_τ was calculated to be $G_\tau = 8.637 \cdot 10^3 [m^{-3}]$. According to eq. A2-9, for $G_\dot{\gamma}$ we then find $G_\dot{\gamma} = 53.14 [-]$.

Even assuming a strong shear thinning, for example $n = 0.1$, only an error of -0.5 % is introduced in calculating $G_\dot{\gamma}$ when eq. A2-9 is used instead of eq. A2-10.

According to the above geometric factors the measurement range of the DCC configuration is given by $0.0086 \leq \tau \leq 86.37 \text{ Pa}$ and $5.3 \cdot 10^{-3} \leq \dot{\gamma} \leq 2667 \text{ s}^{-1}$.

This enables accurate measurement of (Newtonian) viscosities (between 10-90 % of full scales of τ and $\dot{\gamma}$) between $4 \leq \eta \leq 343 \text{ mPa s}$.

References

- [1] R.B. Bird , W.E. Steward , E.N. Lightfoot , "Transport Phenomena" , Wiley and sons , NY (1986)
- [2] C. Blom , R.J.J. Jongschaap , J. Mellema , "Inleiding in de reologie", Kluwer Technische boeken (1986) 62-73
- [3] F.W.A.M. Schreuder , H.N. Stein , Rheol. Acta 26 (1987)45-54

Appendix 3 Error sources with a concentric cylinder measurement geometry

Besides the problem of developing an adequate flow procedure to study a viscous phenomenon, the obtained viscosity data may be troubled by errors due to changes in the thermodynamic conditions of a fluid or due to changes in the flow pattern. These errors are influenced by the magnitude of the shear rate and the geometry of the measurement system.

The following causes can trouble the accuracy of the obtained viscous data on aqueous suspensions :

- turbulence, disturbing the laminar flow profile
- viscous heating
- cracks or discontinuities in the suspension

In the following we will concentrate on pointing out the circumstances under which the above error sources may trouble our measurements [1]. Finally we will discuss the viscosity measurements used to calibrate the rheometer.

Turbulence occurs when the inertial forces in a system exceed the viscous forces. The extra energy dissipation caused by turbulency generally results in an overestimation of the viscosity of the concerned suspension.

At increasing shear rate, a transition from laminar to turbulent flow will occur. At the onset of the transition Taylor vortices will be generated.

Using a concentric cylinder measurement geometry (CC or DCC) the Reynolds number at which the Taylor vortices appear (Searle type rheometer) is given by

$$Re > 41.3 \sqrt{\frac{R_u}{R_u - R_i}} \quad [-] \quad (A3-1)$$

For our CC measurement system (see appendix 2) Taylor vortices are thus expected to initiate above $Re = 148$, while for the DCC they will occur above $Re = 302$.

In case of $R_2 - R_1 \ll R_1$, the Reynolds number may be related to the mean shear rate in the fluid by :

$$Re = \frac{\rho \cdot v \cdot D}{\eta} = \frac{\rho \cdot (R_u - R_i)^2 \cdot \dot{\gamma}}{\eta} \quad [-] \quad (A3-2)$$

The CC geometry has only been used for measuring the most viscous suspensions. Of this group of suspensions, sample 0.40-D showed the lowest (high shear limiting) viscosity (about 60 mPa s). Combining eqs. A2-1,2, substituting suspension and CC

geometry data, Taylor vortices are expected to occur at shear rates exceeding 2900 s^{-1} . As shown in appendix 2 this shear rate is well above the measuring range of the CC system (615 s^{-1}). Thus, while using the CC geometry, turbulence will be absent.

The DCC geometry has been used for measuring suspensions with relative low viscosities. For suspension 0.20-A, the suspension with the lowest viscosity (about 3 mPa s), Taylor vortices are expected at shear rates exceeding 3900 s^{-1} , well above the experimental limit of 2657 s^{-1} . Thus using the DCC geometry viscosity measurements of the suspensions will not be troubled by turbulency. However, when measuring the viscosity of water, the onset of turbulence (according to eqs. A3-1,2) is expected at a shear rate of 2090 s^{-1} , well within the measurement range (see figure A3-1).

Viscous heating caused by the shearing of a suspension may result in a temperature gradient through the sample (cooled wall). An approximation of the expected temperature difference between the sample at the centre of the gap and sample near the wall is given by :

$$T_{\text{centre}} - T_{\text{wall}} = \frac{\eta \Omega^2 R^2}{8\lambda} \quad [K] \quad (\text{A3-3})$$

with R [m] the radius of the rotating cylinder and λ [W/mK] the heat conductivity coefficient of the sample. In case of water ($\lambda \approx 56 \text{ W/mK}$) at the maximum angular velocity (50 rad/s) the calculated temperature difference is negligible ($\approx 10^{-3} \text{ K}$). Viscous heating is not expected to trouble viscosity measurements.

Cracks or discontinuities in the sample can be the cause of major errors. Due to cracking the shear rate will show sudden fluctuations. These fluctuations are easily detectable in a flow curve. Cracking is to be expected while shearing suspensions with a high solids content ($\phi_v > \approx 0.5 \text{ v/v}$). Coarse particles and high shear rates promote the occurrence of cracking.

Discontinuities of the sample near the walls of a cylindrical measurement geometry (near R_1 and R_2) may effectively result in an apparent wall slip. Such discontinuities in a suspension can be the result of particle excluded volume layers. In the excluded volume layers, compared to the bulk volume, a lower particle concentration will exist resulting in a lower viscosity. Here we will investigate the magnitude of the resulting error in determining the viscosity of the suspension from the measured T, Ω data, due to excluded volume layers near R_1 and R_2 with extension Δ [m]. Δ [m] is expected to be of the order of half the mean particle diameter.

To simplify matters, we will assume a Newtonian viscosity behaviour of the suspension inside the excluded volume layers, resulting in a linear shear rate profile inside the excluded volume layers. The total shear rate profile over the measurement gap then will consist of three coupled linear regions. The viscosity of the excluded volume layers is assumed to be $c \eta_0$, with bulk viscosity η_0 and constant $c < 1$.

For a Newtonian suspension, in the absence of excluded volume layers, the relation between

the measured torque and angular velocity (eq. A2-4) results in :

$$\Omega = \frac{1}{4 \pi H \eta_0} \frac{R_2^2 - R_1^2}{R_1^2 R_2^2} T \quad [s^{-1}] \quad (A3-4)$$

Analogous to the derivation of A2-4, using the appropriate boundary conditions, the relation between torque and angular velocity in case of excluded volume layers is given by

$$\Omega_{ws} = \frac{1}{4 \pi H \eta_0} \left[\frac{1}{c R_1^2} - \frac{1}{c(R_1 + \Delta)^2} + \frac{1}{(R_1 + \Delta)^2} - \frac{1}{(R_2 - \Delta)^2} + \frac{1}{c(R_2 - \Delta)^2} - \frac{1}{c R_2^2} \right] T \quad [s^{-1}] \quad (A3-5)$$

As expected, in the limits of $c = 1$ or $\Delta = 0$, equation A3-5 reduces to equation A3-4. In case of a Newtonian viscosity, in the absence of excluded volume layers, from eqs. A2-4 and eqs A2-8,9 the viscosity may be calculated using the measured T, Ω data in the following way :

$$\eta_0 = \frac{G_\tau}{G_\dot{\gamma}} \frac{T}{\Omega} = \frac{R_2^2 - R_1^2}{4 \pi H R_1^2 R_2^2} \frac{T}{\Omega} \quad [Pas] \quad (A3-6)$$

Analogous, to obtain the bulk viscosity in case of excluded volume layers, using the troubled Ω data, the viscosity should be calculated using the following relation :

$$\eta_0 = \left(\frac{G_\tau}{G_\dot{\gamma}} \right)_{ws} \frac{T}{\Omega_{ws}} = \frac{1}{4 \pi H} \left[\frac{1}{c R_1^2} - \frac{1}{c(R_1 + \Delta)^2} + \frac{1}{(R_1 + \Delta)^2} - \frac{1}{(R_2 - \Delta)^2} + \frac{1}{c(R_2 - \Delta)^2} - \frac{1}{c R_2^2} \right] \frac{T}{\Omega_{ws}} \quad [Pas] \quad (A3-7)$$

However, initial Δ and c are unknown. Using the original geometrical factors in treating the T, Ω data in case of excluded volume layers, will result in an underestimation of the bulk viscosity. As can be seen from equations A3-6,7 the relation between the calculated apparent viscosity and the correct bulk viscosity η_0 is given by :

$$\eta_{app.} = \frac{\frac{G_\tau}{G_\dot{\gamma}}}{\left(\frac{G_\tau}{G_\dot{\gamma}} \right)_{ws}} \eta_0 = C \cdot \eta_0 \quad [Pas] \quad (A3-8)$$

with C [-] :

$$C = \left(\frac{1}{R_1^2} - \frac{1}{R_2^2} \right) / \left[\frac{1}{c R_1^2} - \frac{1}{c(R_1 + \Delta)^2} + \frac{1}{(R_1 + \Delta)^2} - \frac{1}{(R_2 - \Delta)^2} + \frac{1}{c(R_2 - \Delta)^2} - \frac{1}{c R_2^2} \right] \quad [-] \quad (\text{A3-9})$$

Compared to the CC geometry, the strongest effect of excluded volume layers is expected when using the DCC configuration (Δ relative large compared to gap) and measuring concentrated suspensions (viscosity of bulk and excluded volume layer will deviate strongly).

For both gaps of the DCC geometry are identical we will calculate the effect of excluded volume layers inside the inner gap with $R_1 = 20$ mm and $R_2 = 20.4$ mm. Assuming the extension of the excluded volume layers to be half the mean particle diameter, we will use $\Delta = 0.2$ μm .

Measuring the viscosity of a concentrated colloidal stable A16SG-F suspension, for instance suspension 0.50-A, will result in a high shear viscosity (Newtonian region) of about 36 mPas. Assuming the volume fraction of the excluded volume layers to be about 0.28 v/v, the accompanying high shear viscosity in the excluded volume layers will be about 4 mPa s (see suspension 0.28-A).

According to equation A3-9 the error (due to the excluded volume layers) in determining the bulk viscosity using the original geometrical constants is lower than 1 %. As shown in appendix 2 the influence of shear thinning on determining the geometrical constants of the DCC system is negligible when $n > 0.1$. The above result is thus also valid in case of more or less flocculated suspensions.

Concluding, in case of A16SG-F suspensions, not exceeding particle volume fractions over 0.5, corrections to account for excluded volume layers are negligible.

Calibration measurements of the rheometer are performed, using the DCC geometry. After filling the DCC geometry and obtaining the desired temperature of 20.0 °C, a shear stress sweep was performed. A total sweep was performed in 30 minutes ($t_{1/2\text{sweep}} = 15$ min.), choosing τ_{max} such to approach the maximum shear rate allowed by the DCC geometry.

In figure A3-1 measurements are shown using two calibration oils of resp. 5.2 and 118 mPa s (Haake) as well as millipore water (1.0 mPa s).

Determining the viscosity of water from the above curve (using data from the high shear regime), results in a relative error of about + 23 % at low shear rates. In case of the calibration oil of 5.2 mPa s a deviation of + 4 % results. These deviations are due to the low viscosities of the samples, resulting in a shear stress sweep outside the 10-90 % measurement range of the DCC geometry (see appendix 2). The viscosity of the 118 mPa s calibration oil (high shear region data well within the 10-90 % measurement range) is

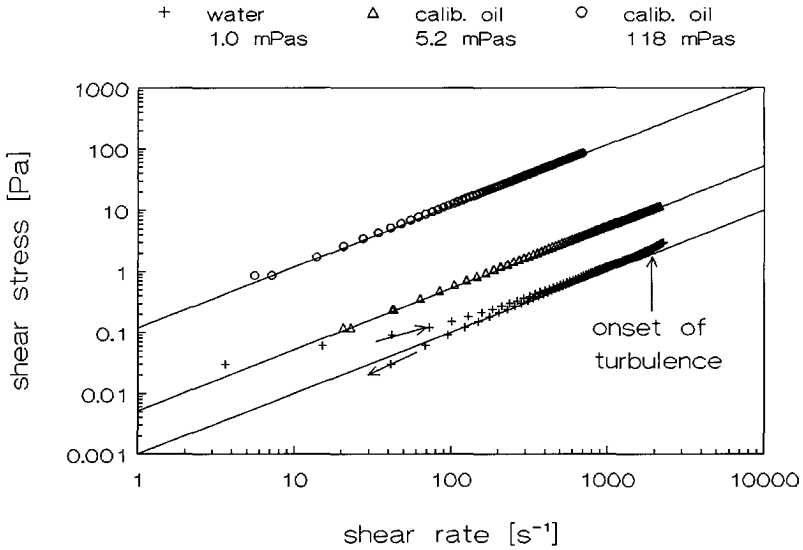


Figure A3-1 Flow curves of calibration fluids using the DCC geometry
(20.0 °C)

accurate within 1 %.

As predicted by equations A3-1,2, shearing water using the DCC geometry results in turbulent flow above about 2100 s^{-1} .

While shearing the calibration oils, turbulence remains absent, as expected from eqs. A3-1,2 .

References

- [1] C. Blom , R.J.J. Jongschaap , J. Mellema , "Inleiding in de reologie" , Kluwer Technische boeken (1986) 62-732

Appendix 4 Measured flow curves in linear-linear representation

In the following, representative measured flow curves are shown in linear-linear representation. The suspension data can be found in table 4.4, while the respective measurement procedures are dealt with in section 4.2. Details of the flow program are shown in table 4.3.

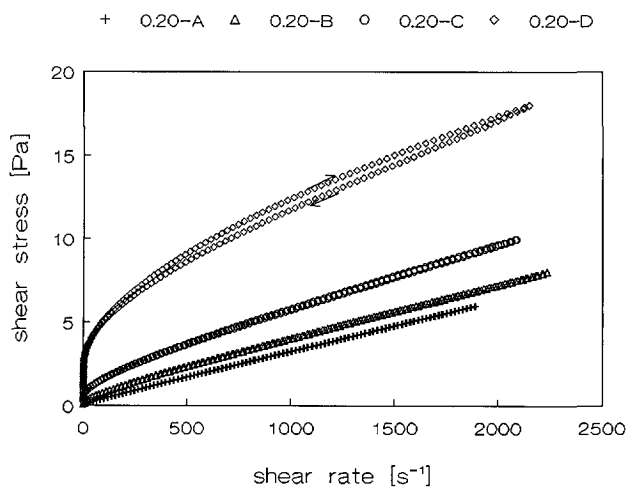


Figure A4-1 Flow curves of the suspensions with solids volume fraction $\phi_v = 0.20$

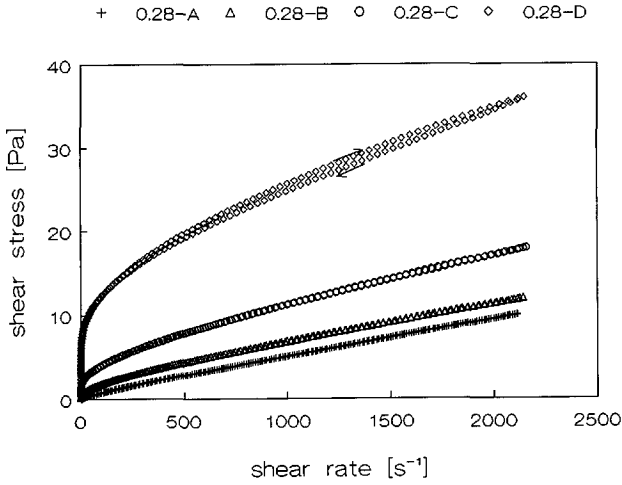


Figure A4-2 Flow curves of the suspensions with solids volume fraction $\phi_v = 0.28$

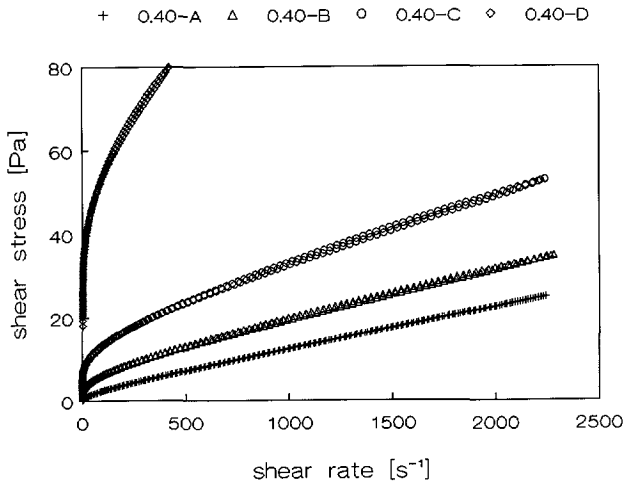


Figure A4-3 Flow curves of the suspensions with solids volume fraction $\phi_v = 0.40$

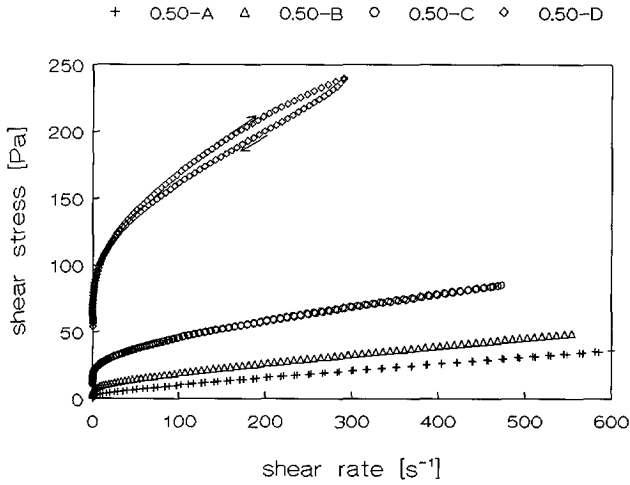


Figure A4-4 Flow curves of the suspensions with solids volume fraction $\phi_v = 0.50$

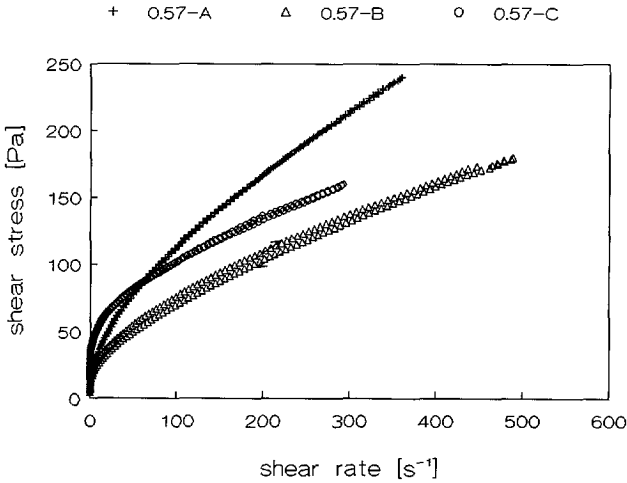


Figure A4-5 Flow curves of the suspensions with solids volume fraction $\phi_v = 0.57$

Appendix 5 Calculation of volumetric shrinkage

In a wet compact, the relation between the solids volume V_s [cm^3] and the liquids volume in the pores V_l [cm^3] is :

$$V_l = \frac{1 - \phi_{\text{wet}}}{\phi_{\text{wet}}} \cdot V_s \quad [\text{cm}^3] \quad (\text{A5.1})$$

with ϕ_{wet} [-] the volume fraction of solids in the wet compact.

In a totally dry compact, after pre-sintering, the relation is

$$V_p = \frac{1 - \phi_{\text{dry}}}{\phi_{\text{dry}}} \cdot V_s \quad [\text{cm}^3] \quad (\text{A5.2})$$

with V_p [cm^3] the dry pore volume and ϕ_{dry} [-] the volume fraction of solids in the pre-sintered compact.

Now the total volumetric shrinkage ΔV [cm^3] can be calculated relative to the original total wet volume $V_{\text{wet}} = V_l + V_s$ or relative to the original wet pore volume V_l . The following equations result :

$$\frac{-\Delta V}{V_{\text{wet}}} = (1 - \phi_{\text{wet}}) - \frac{(1 - \phi_{\text{dry}})}{\phi_{\text{dry}}} \cdot \phi_{\text{wet}} \quad [-] \quad (\text{A5.3})$$

and

$$\frac{-\Delta V}{V_l} = 1 - \frac{\phi_{\text{wet}}}{\phi_{\text{dry}}} \cdot \frac{(1 - \phi_{\text{dry}})}{(1 - \phi_{\text{wet}})} \quad [-] \quad (\text{A4.4})$$

Because the relation between the solids volume fraction of a compact ϕ_c [-] and the corresponding porosity ϵ_c [-] is given by

$$\phi_c + \epsilon_c = 1 \quad [-] \quad (\text{A5.5})$$

equations A5.3 and 4 offer a means to calculate volumetric shrinkage using porosity data.

Appendix 6 Microstructures of the sintered compacts

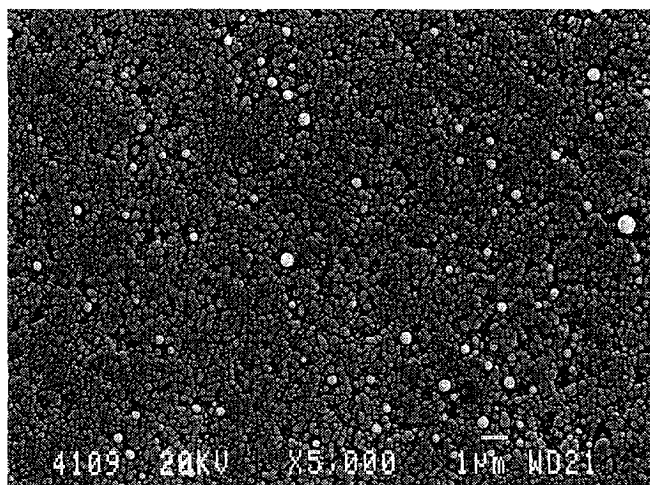


Figure A6-1 Microstructure of a pressure filtrated compact,
PF 1100 °C

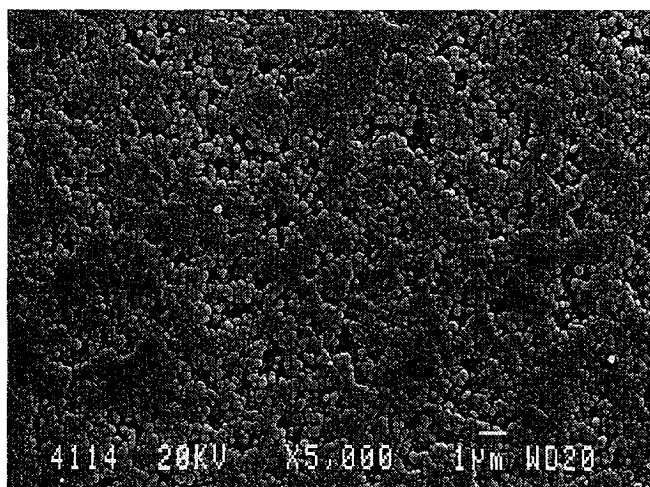


Figure A6-2 Microstructure of a pressure filtrated compact,
PF 1200 °C

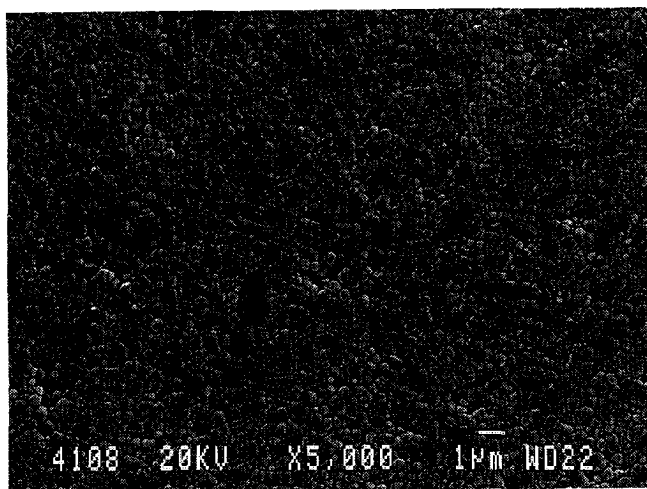


Figure A6-3 Microstructure of a pressure filtrated compact,
PF 1300 °C

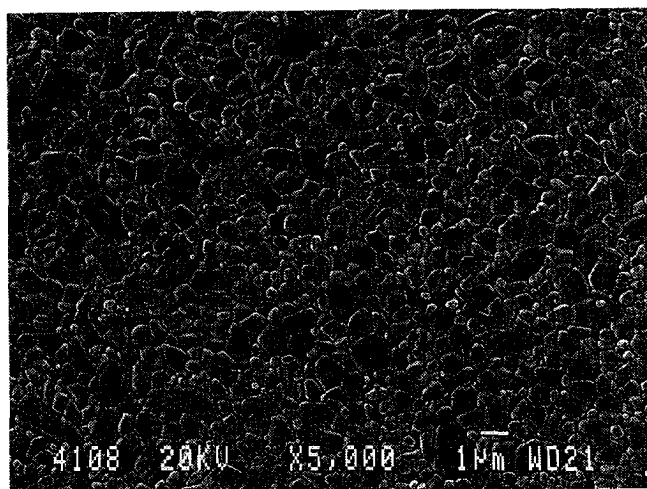


Figure A6-4 Microstructure of a pressure filtrated compact,
PF 1400 °C

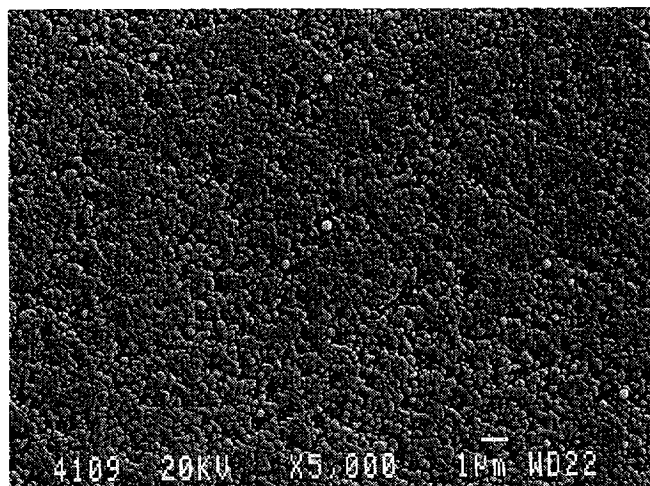


Figure A6-5 Microstructure of a pressure filtrated compact, PF-f 1100 °C

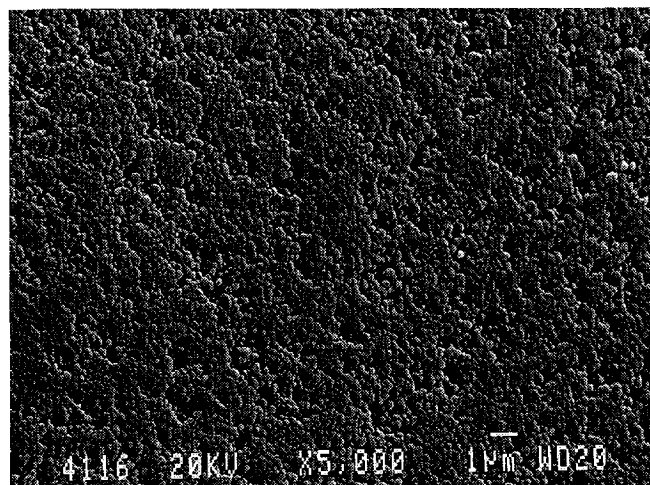


Figure A6-6 Microstructure of a pressure filtrated compact, PF-f 1200 °C

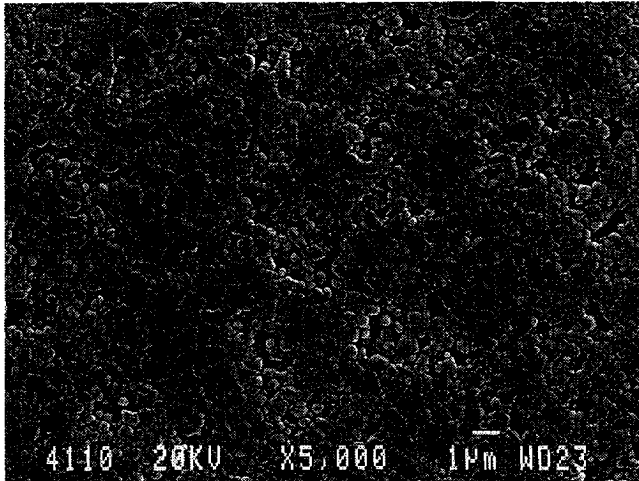


Figure A6-7 Microstructure of a pressure filtrated compact,
PF-f 1300 °C

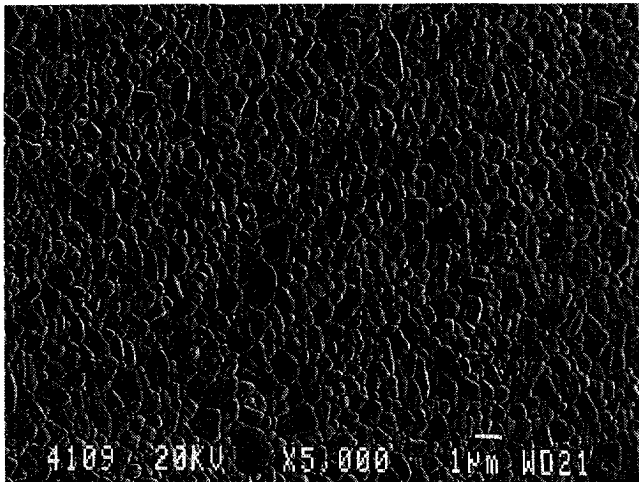


Figure A6-8 Microstructure of a pressure filtrated compact,
PF-f 1400 °C

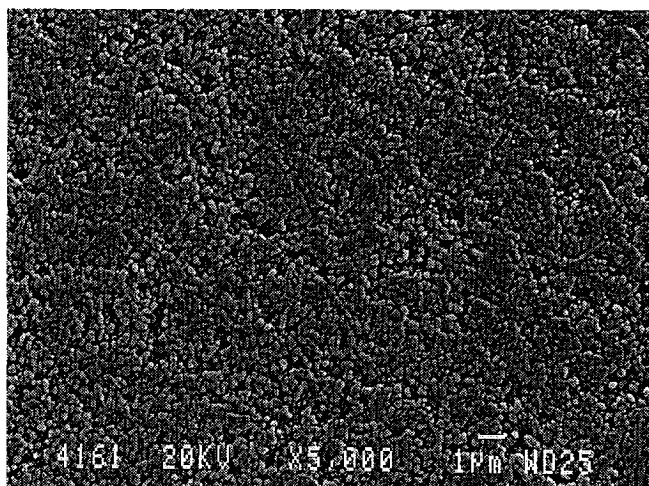


Figure A6-9 Microstructure of a slipcast compact,
SC 1100 °C

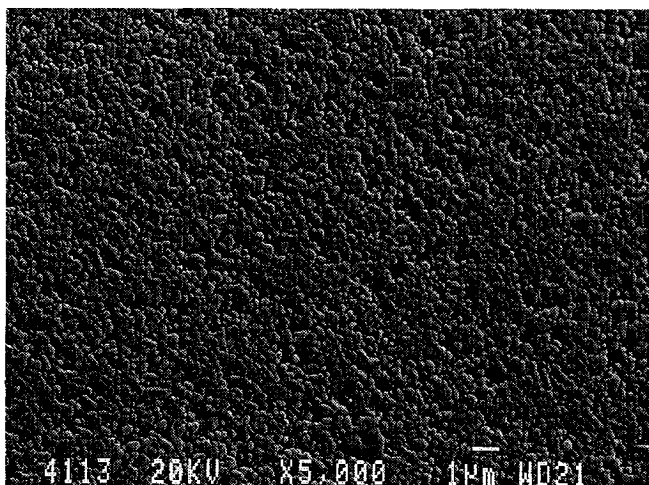


Figure A6-10 Microstructure of a slipcast compact,
SC 1200 °C

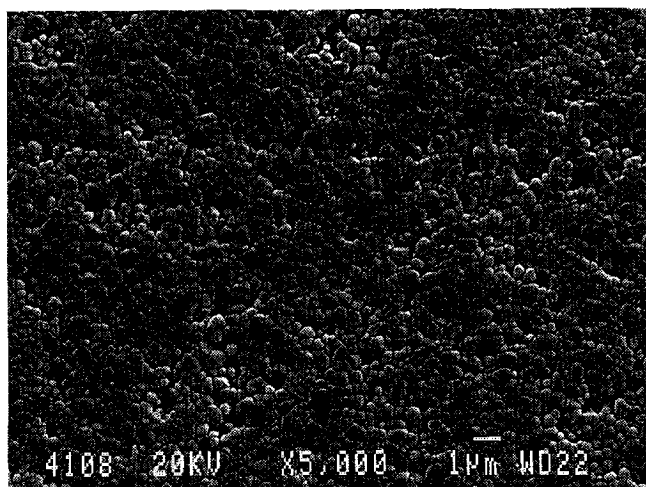


Figure A6-11 Microstructure of a slipcast compact,
SC 1300 °C

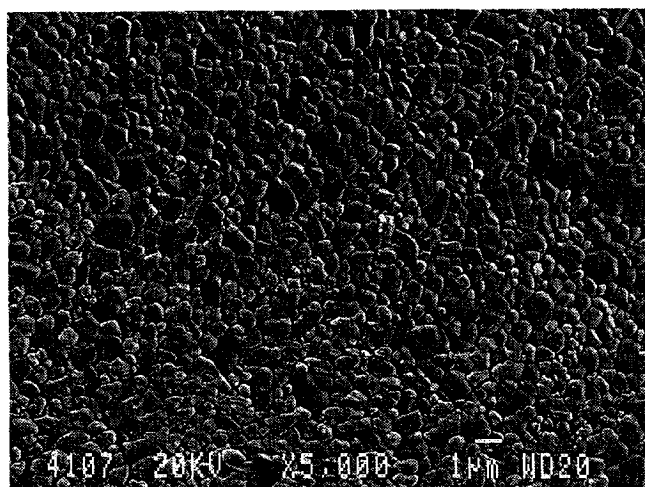


Figure A6-12 Microstructure of a slipcast compact,
SC 1400 °C

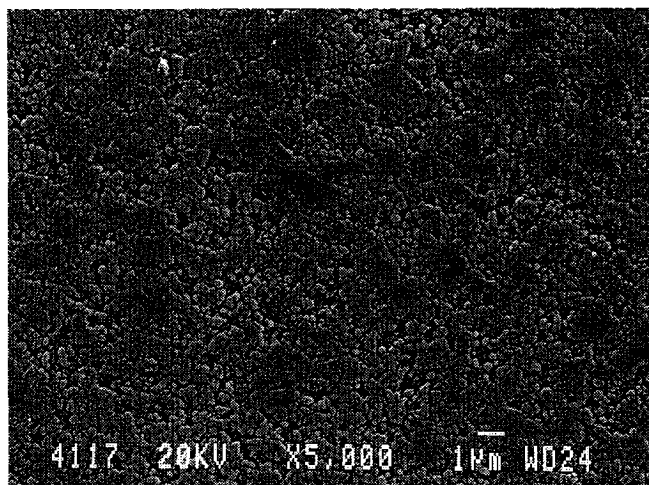


Figure A6-13 Microstructure of a centrifuged compact,
C 1100 °C

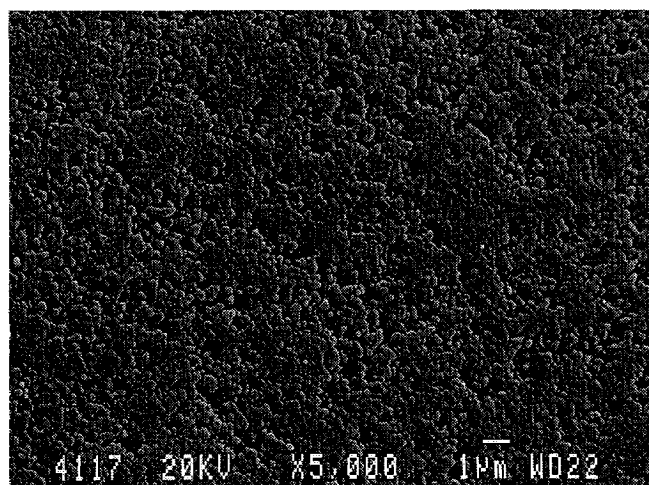


Figure A6-14 Microstructure of a centrifuged compact,
C 1200 °C

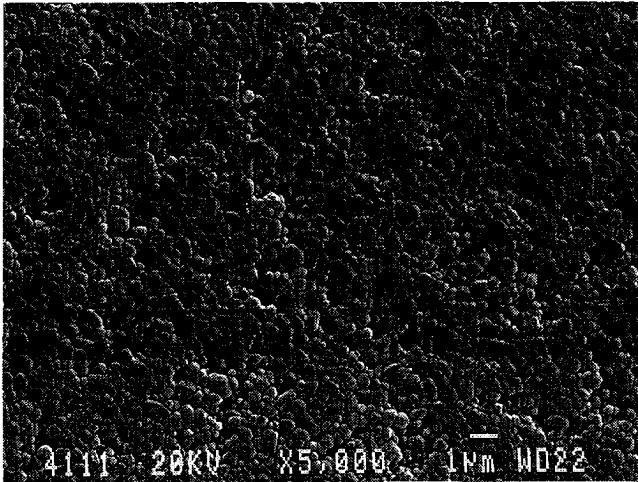


Figure A6-15 Microstructure of a centrifuged compact,
C 1300 °C

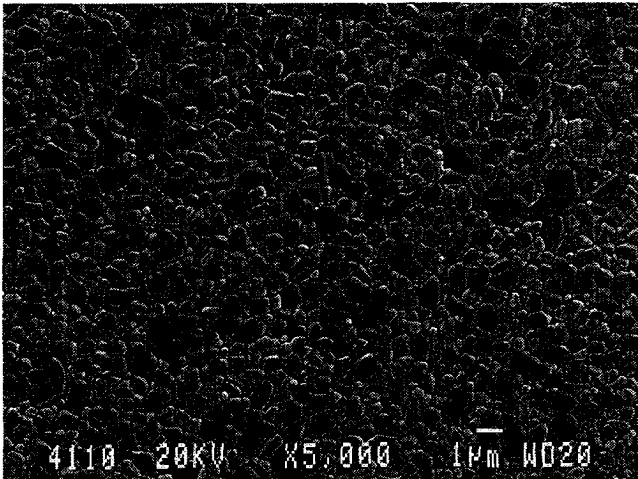


Figure A6-16 Microstructure of a centrifuged compact,
C 1400 °C

Summary

Compared with more conventional materials, the technical ceramic α -alumina exhibits special material properties as a high hardness and wear resistance, even at high temperatures. Extensive use of α -alumina in advanced heat engines and other industrial applications is thus expected. An important property restricting the use of α -alumina is the brittle behaviour of the material. Flaws (local density variations) in the microstructure of the sintered material, reduce the strength of a ceramic. Flaws may be initiated during all processing operations. To control the flaw size population in order to reduce the brittleness of the ceramic, the processing should be optimized.

Due to a high melting temperature, technical ceramics are generally obtained by sintering shaped particle compacts. The particle compacts are preferentially formed by consolidation of colloidal ceramic suspensions. Compared with dry powder consolidation, this wet route offers the best possibilities to control the microstructure development, because the strength of the particle interactions can be adjusted. For small series of parts with a complicated shape, techniques as pressure filtration, slip casting or centrifugal densification are appropriate. To reduce the process time, high shear rates of the fluid are necessary during wet consolidation.

For a given powder, the microstructure of the wet compact is determined by the combination of suspension properties and the parameters of the used consolidation process. The wet compact acts as a precursor in the formation of the structure of the dried (green) product, and finally affects the microstructure of the sintered product.

We studied the effect of the direction of fluid flow relative to the particle motion during consolidation and the influence of the particle interaction on the density and the particle ordering of the wet compact. A link between rheology and the consolidation of concentrated suspensions has been established, which enables us, through rheological measurements, to predict the influence of the strength of particle attraction on the density of a wet compact.

Compaction techniques as pressure filtration, slip casting and centrifugation have been used to densify aqueous suspensions of a fractionated submicrometer α -alumina powder. In these electrocratic colloids, the strength of the particle interaction has been varied through adjustment of the electrolyte concentration.

By developing the obtained wet compacts under equal drying and sintering conditions, the relations between the structure of the wet and the green compact, and the resulting microstructure development during sintering, have been investigated.

During consolidation a transition layer exists, the consolidation zone, in which suspension is continuously converted into particle compact. An important factor influencing further densification of this zone is the magnitude and the direction of the fluid flow relative to the particle motion.

In case of counterflow, when the shear forces on the particles oppose the densification of

the consolidation zone (centrifugation), ordered and relatively open particle compacts result. In ideal compaction, the shear in the consolidation zone promotes densification (pressure filtration, slip casting), resulting in dense and homogeneously stacked particle compacts. The density of these particle packings depends on intrinsic properties of the alumina powder and the strength of net particle attraction.

Compaction experiments with stable alumina suspensions confirmed the expected higher density of the compacts formed by ideal compaction, compared with the compacts formed by counterflow.

Both ideal consolidation and the shear thinning behaviour of concentrated suspensions are affected by particle interaction.

Shear induces particle displacements in a suspension. When a particle in a concentrated, more or less flocculated suspension is displaced, it will drag its neighbouring particles. Chains of combined particle displacements are thus involved on displacement of one particle. This drag effect opposes the displacement of the particles, and thus influences the viscosity and the consolidation of concentrated suspensions. The extent of the drag effect depends on the number of particle contacts (coordination number q) and the net strength of particle attraction (interaction parameter l^2).

When particle drag results in the blocking of particle motions, the viscosity of the suspension diverges. Further densification of the consolidation zone is then not possible.

An existing rheological model for flocculated suspensions, the Giant-Floc model, has been used to account for the influence of particle drag (q , l^2) on the shear thinning of flocculated concentrated suspensions. The model has been evaluated in limit of high shear, and adapted to describe the relation between the drag parameters and the high shear limiting viscosity of more or less flocculated suspensions. Interpretation of the shear thinning of our concentrated α -alumina suspensions with the rheological model in terms of q and l^2 , related the interaction parameter l^2 to the suspension stability. Based on the rheological model, with a known interaction parameter l^2 of a suspension, the densities of the consolidated wet particle compacts formed by ideal compaction could be predicted successfully.

The wet compact structure strongly influences the green structure. The dense homogeneous stacked compacts formed by ideal consolidation, result in green structures with small local density variations (little clustering) and with a high density due to a strong shrinkage. A larger net particle attraction, i.e. an increased interaction parameter l^2 , reduces the drying shrinkage. A forced drying rate, as in slip casting, leads to a "frozen" wet structure with a reduced drying shrinkage.

The more open and orderly stacked compacts, as formed by counterflow, show less shrinkage and yield a strongly clustered structure consisting of dense and less dense regions.

The sinter rate reflects the internal green structure of a particle compact, and is thus influenced by the method of wet consolidation.

In the early stages of sintering, a higher porosity of the dried compacts causes a slower rate

of densification. The clustering of all structures proceeds, however, the differences in clustering maintain.

With the used sintering program, all compacts were finally sintered to near theoretic density. Differences between the sintered microstructures remained visible. Compared with the random structures as formed by ideal compaction, the grain size distribution of the strongly clustered structures (counterflow) shows an increased fraction of small grains.

The way in which particles interact during wet consolidation is thus an essential factor in determining the quality of a ceramic product which results from the sintering of a particle compact. This leads to our thesis :

In wet compaction, the flow of the fluid surrounding the consolidating particles must be controlled, in order to master the quality of a sintered product.

Samenvatting

De beheersing van de microstructuur van deeltjespakkingen door middel van natte consolidatietechnieken

Het technische keramiek α -alumina heeft, vergeleken met conventionele materialen, speciale materiaaleigenschappen als een hoge hardheid en slijtvastheid, zelfs bij hogere temperaturen. Hierdoor is een breed scala van industriële toepassingen denkbaar, zoals b.v. in apparaten voor energie-omzetting bij hoge temperatuur. Het brosse karakter van het materiaal vormt echter een belemmering voor het gebruik van α -alumina. De sterkte van keramiek neemt af door de aanwezigheid van "flaws" (plaatselijke dichtheidsvariëaties) in de microstructuur. Tijdens het vervaardigen van keramiek kunnen alle processtappen aanleiding geven tot de vorming van flaws, zodat de gehele procesroute geoptimaliseerd dient te worden.

Door het hoge smeltpunt van α -alumina, wordt een dicht vormstuk in het algemeen verkregen door een vormgegeven deeltjesstapeling te sinteren. Bij voorkeur worden de deeltjespakkingen verkregen door consolidatie van colloïdale keramische suspensies. Deze natte productieroute geeft, vergeleken met het verdichten van droge poeders, de beste mogelijkheden om de vorming van de microstructuur te beheersen, omdat de deeltjesinteracties kunnen worden ingesteld. Voor de vervaardiging van kleine series van vormstukken met een gecompliceerde vorm, zijn technieken als drukfiltratie, slibgieten en centrifugale verdichting, bijzonder geschikt. Bij de gebruikte korte procestijden treden tijdens de consolidatie van suspensies zeer hoge afschuifsnelheden in de vloeistof op.

Uitgaande van een poeder, wordt de microstructuur van de natte deeltjespakking bepaald door de combinatie van suspensie-eigenschappen en de parameters van de gebruikte verdichtingstechniek. De natte deeltjespakking werkt als precursor in de vorming van de droge (groene) structuur, en beïnvloedt uiteindelijk de microstructuur van het gesinterde vormstuk.

Wij onderzochten het effect van de richting van de vloeistofstroming relatief ten opzichte van de deeltjes tijdens consolidatie en de invloed van de deeltjesinteractie, op de dichtheid en de deeltjesordening van de natte deeltjespakking. Daarbij is een relatie gelegd tussen de reologie en de consolidatie van geconcentreerde suspensies, waardoor, met behulp van reologische metingen, de invloed van de sterkte van de deeltjesinteractie op de dichtheid van een natte deeltjespakking voorspeld kan worden.

Suspensies van een gefractioneerd submicrometer α -alumina poeder (op waterbasis) zijn verdicht met behulp van technieken als drukfiltratie, slibgieten en centrifugatie. De sterkte van de deeltjesinteractie in deze electrocratische colloïden is gevarieerd door het instellen van de elektrolytconcentratie. Door de verkregen natte deeltjespakkingen onder vast gekozen condities te drogen en te sinteren, konden de relaties tussen de structuur van de natte en de droge deeltjespakking en de resulterende microstructuurontwikkeling tijdens het

sinteren worden onderzocht.

De continue verdichting van suspensie naar deeltjespakking vindt plaats in de consolidatiezone. De grootte en richting van de vloeistofstroming ten opzichte van de deeltjes, vormen een belangrijke factor in de mate van verdichting die optreedt in de consolidatiezone.

In het geval van tegenstroming, als de afschuifkrachten op de deeltjes verdere verdichting bemoeilijken, ontstaan open en geordende deeltjespakkingen. Bij ideale consolidatie echter, leidt de vloeistofstroming in de consolidatiezone tot afschuifkrachten die de verdichting bevorderen (drukfiltratie, slibgieten). Dit resulteert in het ontstaan van dichte en homogeen gestapelde deeltjespakkingen. De dichtheid van deze pakkingen wordt bepaald door intrinsieke eigenschappen van het te verdichten poeder en de sterkte van de deeltjesattractie. Verdichtingsexperimenten uitgaande van stabiele alumina suspensies hebben de verwachte hogere dichtheid van de deeltjespakkingen gevormd met ideale consolidatie bevestigd.

Zowel de ideale consolidatie als het shear thinning gedrag van geconcentreerde suspensies worden beïnvloed door deeltjesinteractie.

Afschuiving veroorzaakt deeltjesverplaatsingen in een suspensie. Als een deeltje in een geconcentreerde, meer of minder gevlokte suspensie verplaatst wordt, zal het aangrenzende deeltjes meeslepen. Hierdoor resulteert het verplaatsen van één deeltje in reeksen van gekoppelde deeltjesverplaatsingen, waardoor het meesleepeffect deeltjesverplaatsing hindert. De invloed van het meesleepeffect is afhankelijk van het aantal deeltjescontacten (coördinatie getal q) en de sterkte van de deeltjesattractie (interactie parameter l^2). Als het meesleepeffect leidt tot het blokkeren van deeltjesverplaatsingen, divergeert de viscositeit van de suspensie, waardoor verdere verdichting van de consolidatiezone niet meer mogelijk is.

Een bestaand reologisch model voor geflocculeerde suspensies, het Giant-Floc model, is gebruikt om de invloed van het meesleepeffect (q, l^2) op het shear thinning gedrag te beschrijven. Het model is uitgewerkt in de limiet van hoge afschuifsnelheden, en aangepast om de relatie tussen de meesleepparameter en de high shear limiting viscosity van meer of minder geconcentreerde suspensies te beschrijven. Het interpreteren van de shear thinning van onze geconcentreerde α -alumina suspensies met het reologisch model in termen van q en l^2 , maakt het mogelijk om de interactie parameter l^2 te relateren aan de suspensiestabiliteit. Wanneer de l^2 van suspensies bekend is, kunnen we, uitgaande van het reologisch model, de dichtheden van deeltjespakkingen gevormd met ideale verdichting voorspellen.

De groene structuur wordt sterk beïnvloed door de structuur van de natte deeltjespakking. Uit de dichte en homogeen gestapelde pakkingen, welke zijn gevormd m.b.v. ideale consolidatie, ontstaan groene structuren met kleine locale dichtheidsvariaties (lichte clustering) en met een hoge dichtheid t.g.v. een sterke krimp. Een verhoogde deeltjesattractie (hogere l^2) leidt tot een afname van de droogkrimp.

De meer open en geordende pakkingen, zoals gevormd onder tegenstroming, geven

aanleiding tot minder droogkrimp en leiden tot een sterk geclusterde groene structuur, bestaande uit open en dichtere gebieden.

De sintersnelheid is gerelateerd aan de interne structuur van de groene deeltjespakkingen en wordt dus beïnvloed door de omstandigheden tijdens natte consolidatie. In de beginstadia van het sinteren resulteert een hogere porositeit van de droge deeltjespakkingen in een lagere verdichtingssnelheid. In alle structuren treedt verdere clustering op, maar de verschillen in de mate van clustering blijven aanwezig.

Met het gebruikte sinterprogramma werden alle deeltjespakkingen tot vrijwel de theoretische dichtheid verdicht. Er bleven echter verschillen tussen de microstructuren van de gesinterde pakkingen zichtbaar. De korrelgrootteverdeling van de sterk geclusterde structuren (tegenstroming) toont een verhoogde fractie van kleine korrels vergeleken met de structuren voortkomend uit ideale consolidatie.

De wijze waarop de deeltjesinteractie plaats vindt tijdens de natte verdichting is dus een essentiële factor in het beïnvloeden van de kwaliteit van een keramisch product gevormd door het sinteren van een deeltjespakking. Dit leidt tot onze thesis :

Bij natte verdichting moet de stroming van de vloeistof waaraan de deeltjes tijdens consolidatie onderhevig zijn worden gestuurd, als uitgangspunt voor de beheersing van de kwaliteit van een gesinterd product.

Nawoord

Tijdens de uitvoering van dit onderzoek en het schrijven van het proefschrift heb ik van velen steun en medewerking gekregen, waarvoor ik zeer dankbaar ben. Een aantal personen en organisaties wil ik hier daarom graag met name noemen :

Ik ben allereerst veel verschuldigd aan mijn promotor Prof. Frens voor de degelijke wijze waarop hij mijn onderzoek begeleid heeft. Hij heeft in de loop van de tijd veel ideeën aangedragen, en de uiterst gevarieerde gedachtenwisselingen met hem waren zowel prettig als leerzaam.

Het ECN ben ik erkentelijk voor de mogelijkheid om het onderzoek uit te voeren en voor het drukken van het proefschrift.

Lucy Correia heeft een belangrijke bijdrage geleverd aan het verloop van het onderzoek, mede middels de vele discussies en tips op het gebied van het filtratie- en sinter-onderzoek. Ben Bonekamp, mijn begeleider bij het ECN, en Hubert Veringa, dank ik voor de vele discussies over de onderzoeksresultaten en over de fundamentele achtergronden van fysisch/-chemische processen.

Bij het ECN zijn verder Ruud Nyqvist en Cor van Egmond (karakteriseringswerkzaamheden), Gerrit Hamburg (SEM onderzoek), Loek Berkeveld (preparatie mallen en filters) en Trudy Zomerdijk (afdrukken manuscripten) belangrijk geweest.

Erik Kelder stond altijd klaar voor informatie over de gang van zaken aan de TU Delft en voor een goed gesprek bij een kop koffie.

Bert Groenestein heeft veel moeite gedaan om een druk-klare versie van het proefschrift te verzorgen.

Tenslotte dank ik al mijn vrienden, mijn ouders en familie, voor de morele steun die zij mij hebben gegeven en al het overige.

Curriculum Vitae

Peter van Houten werd geboren op 15 februari 1961 te 's-Gravenhage. Van 1974 tot 1980 doorliep hij het VWO (typisch β eindexamen pakket) aan de scholengemeenschap Hugo Grotius te Delft. Na twee jaar Chemische Technologie gestudeerd te hebben aan de Technische Hogeschool Delft, volgde hij aldaar de studie Materiaalkunde aan de inmiddels tot Technische Universiteit verworpen TH. In februari 1988 studeerde hij af bij prof.dr. J. Schoonman (sectie Toegepaste Anorganische Chemie) op een onderzoek naar de relatie tussen de processing en het ionengeleidend vermogen van dunne lagen lithiumnitride.

Van oktober 1988 tot maart 1993 was hij als promovendus in dienst van het Energieonderzoek Centrum Nederland ECN. Zijn promotor was prof. G. Frens van het Laboratorium voor Fysische Chemie, TU Delft. In deze periode heeft hij zich bezig gehouden met onderzoek naar de beheersing van de structuur van deeltjespakkingen gevormd met behulp van natte consolidatietechnieken. De behaalde onderzoeksresultaten zijn deels beschreven in dit proefschrift.

